CHAPTER IV
RESULTS AND DISCUSSION

4.1 Corrosion Test in the Ti-2 Autoclave with Heat Transfer

4.1.1 Run 1

During exposure, samples darkened; an example is shown in Figure 4.1. Exposed samples were weighed and their weight changes are reported in Table 4.1. It shows that some SG samples gained weight, some lost weight, and for some, their weights remained unchanged. Zircaloy-4 and SS304 samples gained weight fairly significantly, compared with weight changes of the SG samples. These should be caused by the balance of formation and dissolution of the oxide film during exposure.

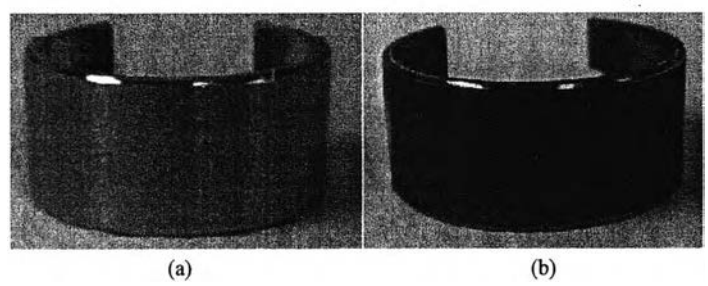

Figure 4.1 SG1 sample band in Run 1 (a) before exposure and (b) after exposure.

Table 4.2 presents the coolant chemistry in Run 1. The measurements show that boron concentration after exposure was lower than that before exposure. Boric acid precipitation from residual solution on the test section and the autoclave body may have contributed to the difference; however, the difference is less than 2% and within measurement error. The concentrations of Ni, Fe and Mn in the coolant increased during exposure, no doubt due to the dissolution of these metal ions (which have high diffusion rate) from the corrosion products and the base materials of SG and SS304 samples. The Zn concentration after exposure was higher than that before exposure, possibly due to the releasing steam from the autoclave at start of exposure (because the pressure was over the saturation pressure) and the residual Zn

contamination from the lubricant used in this work (ZnO is one of its constituents) and/or from the previous work (the autoclave was operated with water containing Zn).

Table 4.1 Weight of the sample bands before and after exposure in Run 1

Sample	Surface Area (cm^2)	Before (g)	After (g)	Weight Change (mg)	Weight Change per Unit Area (mg/dm^2)
Zircaloy-4	4.17	0.9482	0.9490	+0.8	+19.18
SS304	4.68	2.1031	2.1039	+0.8	+17.09
SG1	6.24	4.4468	4.4467	-0.1	-1.60
SG2	6.24	4.3921	4.3922	+0.1	+1.60
SG3	6.24	4.4067	4.4063	-0.4	-6.41
SG4	6.24	4.4554	4.4554	0.0	0.0
SG5	6.24	4.4564	4.4562	-0.2	-3.20
SG6	6.24	4.4155	4.4155	0.0	0.0

Table 4.2 Coolant chemistry before and after exposure in Run 1

Conditions	Before	After
Boron concentration (ppm)	2022	1986
pH @ room temperature	6.35	6.19
$pH_{300°C}$	6.94	6.95
Fe concentration (ppb)	-	very low**
Ni concentration (ppb)	-	32.1±0.93
Mn concentration (ppb)	-	22.4±3.1
Zn concentration (ppb)	0.4*	5.8±1.1

*from the de-ionized water

**below the detection limit

There are several techniques used to analyse the oxide films grown on the samples. In this run, SG1, SG3, SG6, SS304 and Zirc-4 were analysed with EDX and SEM, while Zirc-4, SS304, SG3 and SG6 were analysed with SIMS. Only SG3 was analysed with XPS. The results are presented and discussed as follows:

4.1.1.1 EDX and SEM Analyses

SG1 was examined with EDX to estimate the elemental compositions of oxide formed on its convex surface. The results at three different locations along the circumferential line, as explained in Figure 3.7, are shown in Table 4.3. It should be kept in mind that the EDX results include contributions from the composition of the underlying metal, since the oxide was quite thin. From the result, the elemental compositions of SG1 before and after exposure are seen to be different. It indicates the presence of an oxide film formed on the surface of the sample. Moreover, the elemental compositions are slightly different at different locations, possibly because they were exposed to slightly different coolant temperatures. However, the differences are within measurement error. Table 4.3 indicates that the weight percentage of Fe and Ni of the sample decreased during exposure, while the weight percentage of Cr increased. This could be caused by the preferential dissolution of Fe and Ni from the substrate alloy and the formation of a Cr-rich oxide during the first stage of corrosion (Carrette *et al.*, 2003) and is consistent with the increase of the Fe and Ni concentrations in the coolant during exposure as shown in Table 4.2. The weight percentage of Ti was greater after exposure, most likely because of the incorporation of Ti from the autoclave and the test section into the oxide film and/or the precipitation of TiO_2 on the SG1 surface. Surprisingly, Zr and Cu were found in significant amounts after exposure. Such Zr came from the heater cladding material but the source of Cu remains unclear.

Table 4.3 EDX result from the convex surface of SG1 in Run 1

Position	Wt%							
	Ni	Fe	Cr	Mn	Ti	Cu	Zr	O
-90°	63.35	9.25	16.40	0.22	0.77	1.12	0.05	7.83
30° (Facing the heater)	64.71	9.45	17.12	0.19	0.56	1.16	0.06	5.91
+90°	62.57	9.08	16.11	0.15	0.87	1.23	0.14	8.83
Before exposure	70.83	9.63	15.40	0.26	0.39	*	-	2

*was not recorded

In addition, SG1 was sectioned at the circumferential line and was analysed with EDX and SEM. The SEM cross-section images are shown in Figure 4.2. They confirm the presence of an oxide film on the surface. The oxide film was very thin (approximately 0.1 μm) as can be seen at the outside of the bright zone in Figure 4.2.

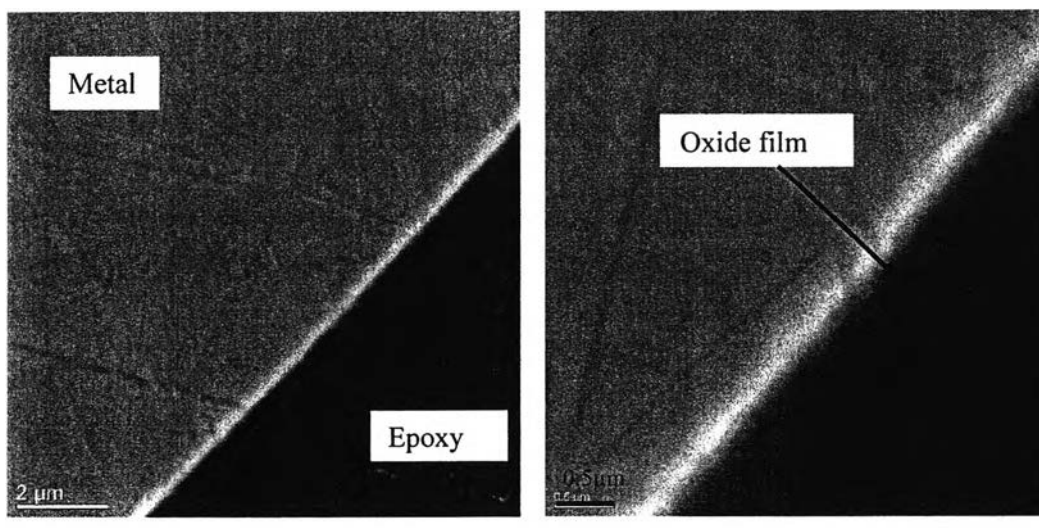

(a) (b)

Figure 4.2 SEM cross-section image of oxide film grown on SG1 in Run 1 at the 30° position (facing the heater); (a) at low magnification (b) at higher magnification.

Table 4.4 shows the result of EDX analyses on the cross-sectional surface along three different locations on the radial line, as illustrated by Figure 3.9. The result shows that the metal contents (except Ti and Cu) tend to decrease slightly toward the M/MO interface (A is at the M/MO interface), possibly because of the diffusion of oxygen into the alloy. The amount of Ti and Cu is significant near the M/MO interface, no doubt due to the incorporation of Ti and Cu from the coolant. However, the 0.1 μm oxide film is too thin to be analysed accurately with EDX.

Table 4.4 EDX result on the cross-sectional surface along radial lines of SG1 in Run 1

Location	Wt%					
	Ni	Fe	Cr	Ti	Cu	Zr
-90°, A	69.71	9.33	16.19	0.21	0.95	-
-90°, B	72.54	10.14	16.69	0.28	0.78	-
-90°, C	71.85	9.76	16.72	0.23	0.79	-
30°, A*	71.71	9.56	16.17	0.24	1.01	-
30°, B*	71.76	9.94	16.27	0.24	0.43	-
30°, C*	72.03	9.96	16.89	0.29	0.88	-
+90°, A	70.86	9.66	15.96	0.33	1.11	-
+90°, B	71.76	9.73	16.74	0.23	0.73	-
+90°, C	71.95	10.28	16.99	0.26	0.87	-

*facing the heater

Next, the convex surfaces of SG3, SG6, SS304 and Zircaloy-4 were analysed with SEM. The surface morphology on different materials was different, reflecting different compositions. Figure 4.3 shows the surface morphology of SG3 and SG6. The surfaces are almost identical because they were exposed to almost the same temperature in their relative positions. As can be seen in Figure 4.3, the surfaces were covered with a sparse layer of acicular crystallites. This needle-like

morphology seems to occur at scratches or other defects, presumably because such areas are preferential sites for oxidation. Similarities with the results of Neves *et al.* (2008) suggest that the needle-like features are NiO.

Surface morphologies of SS304 and Zircaloy-4 are shown in Figure 4.4. The surface of SS304 was covered by a crystallite layer overlaying a layer that had no obvious crystallinity. From Table 4.5, comparing the average elemental compositions on crystallites and on the underlying layer (an area next to crystal), it appeared that the Cr content in the crystallite layer was lower than that in the underlying layer, since the Fe/Cr ratio in the crystallite layer was higher than that in the underlying layer. It indicated that the crystallite layer was a Fe-rich layer and the underlying layer was a Cr-rich layer. These results are consistent with the result reported by Tapping *et al.*, (1986). They reported that the oxide formed on SS304 is commonly a two-layer oxide consisting of an outer, $NiFe_2O_4$ crystallite layer with an inner, amorphous $(Fe, Cr)_2O_3$ layer. Later publications suggest the inner layer is based on iron chromite, $FeCr_2O_4$ (Lister, 2004).

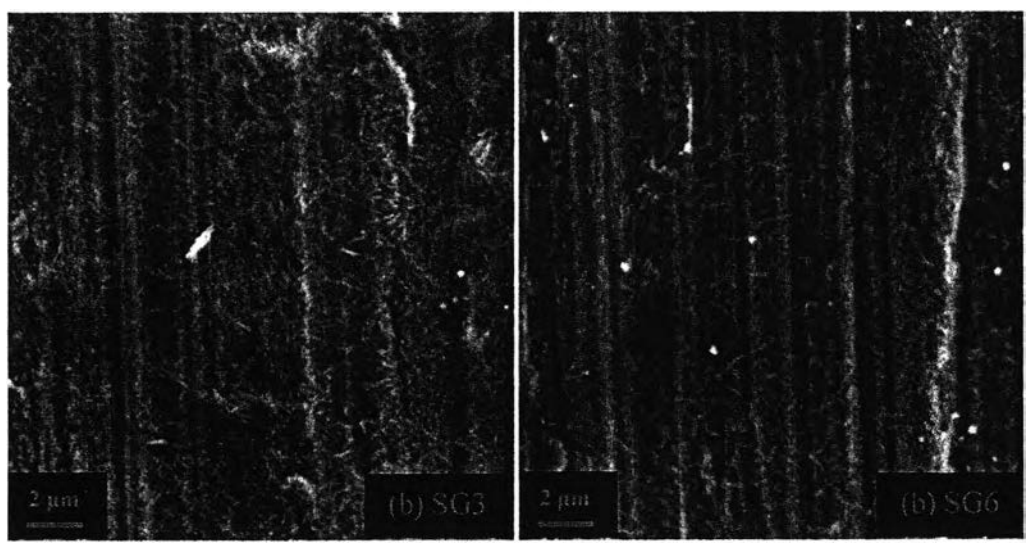

Figure 4.3 SEM images of (a) SG3 and (b) SG6 in Run 1.

On the Zircaloy-4 surface, platelet oxides were observed, especially associated with cracks or scratches as shown in Figure 4.4 (b). The EDX results in Table 4.6 show that Zr is the majority composition in the platelet oxides,

indicating that these oxides should be ZrO_2. Some regular strip-like features were observed on the underlying layer possibly associated with marks left from machining

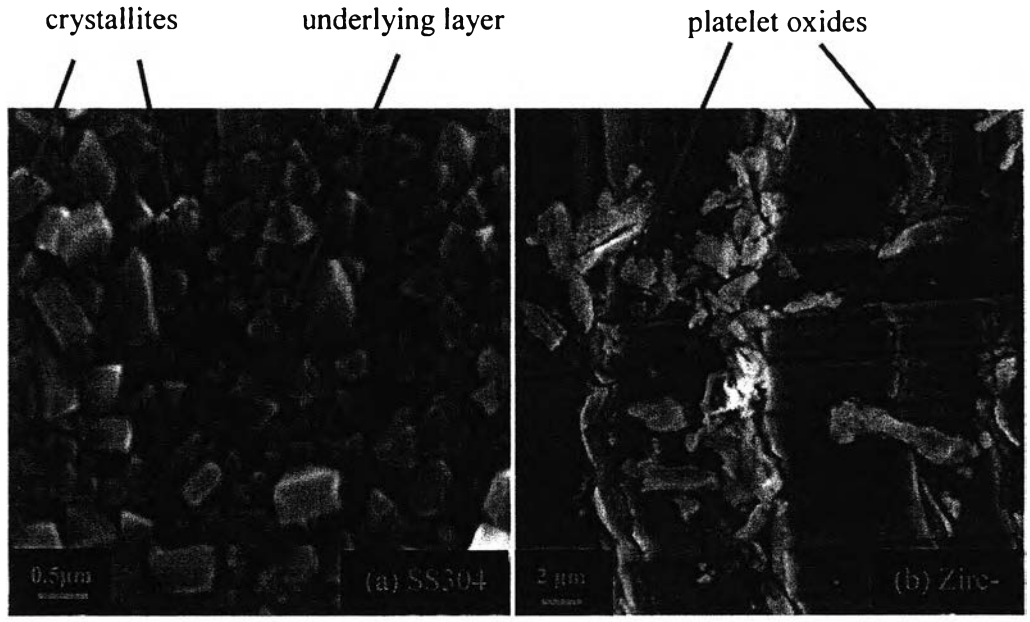

Figure 4.4 SEM images of (a) SS304 and (b) Zirc-4 in Run 1.

Table 4.5 EDX analyses on the convex surface of SS304 in Run 1

Position	Wt%				
	Ni	Fe	Cr	O	Fe/Cr
Crystallite layer	4.89	46.45	9.86	38.8	4.12
Underlying layer	8.4	49.89	16.44	25.27	3.04

Table 4.6 EDX analyses on the convex surface Zircaloy-4 in Run 1

Position	Wt%					
	Ni	Fe	Cr	Zr	Sn	O
Platelet oxide	0.37	0.56	0.19	65.95	0.94	31.99

4.1.1.2 SIMS Analysis

SIMS analyses were performed on Zircaloy-4, SS304, SG3, and SG6 sample bands and the results are shown in Figure 4.5-4.8. For SG samples, depth profiles were obtained from the locations facing the heater. Figure 4.5 shows the depth profile of the exposed Zircaloy-4. After 10 days, the oxide film mainly consisted of Zr and Sn, which are the main compositions of the Zircaloy-4 as shown in Table 4.7. The oxide film was enriched in Ni, Fe, Cr, Ti and Cu at the solution interface, possibly due to the deposition of metal oxides of these elements from the coolant.

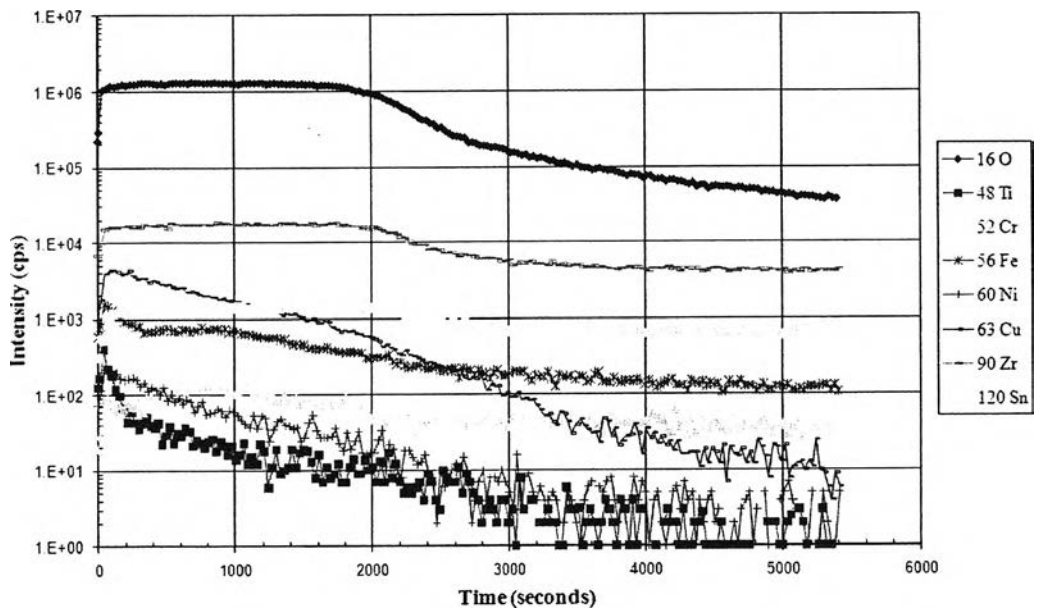

Figure 4.5 SIMS analysis on Zircaloy-4 in Run 1.

Table 4.7 Compositions of Zircaloy-4 and SS304

Composition	Wt.%	
	Zircaloy-4*	**SS304****
Cr	0.1	18-20
Fe	0.2	68-73
Ni	0.007	8-10.5
C	-	0.08 max
Si	-	1.0 max
P	-	0.045 max
S	-	0.03 max
Zr	98.2	-
Sn	1.5	-

*(Glasstone and Sesonske, 1981)

**(Rahn, 1984)

Figure 4.6 and Figure 4.7 show depth profiles of SG3 and SG6 respectively. The elemental intensities of SG3 and SG6 are very slightly different, possibly because they were exposed to slightly different coolant temperatures. The results show that the oxides were enriched in Fe and Cr. The oxide films seem not to be duplex oxides as commonly observed in the oxide formed on Ni-based alloy in high-temperature water (Lister, 2003), possibly because ten days is too short an exposure to accomplish complete oxide development. However, it is expected that duplex oxide films would form if the samples were exposed for longer exposure times, resulting in coolant saturated with metal ions. Titanium incorporated into the oxide may be from the test section and/or the base material. Cu is also detected by SIMS analysis and by EDX analysis. From the SIMS results on SG3 and SG6, the intensity of Cu was unchanged throughout the long sputtering time. It is possible that Cu observed in the oxides comes from the SG alloys. However, Cu possibly comes from the lubricant used in this work, which has Cu as its constituent.

Figure 4.8 shows a depth profile of the exposed SS304. The oxide film was slightly enriched in Fe and Cr. As with SG3 and SG6, significant amounts of Cu and Ti were also observed.

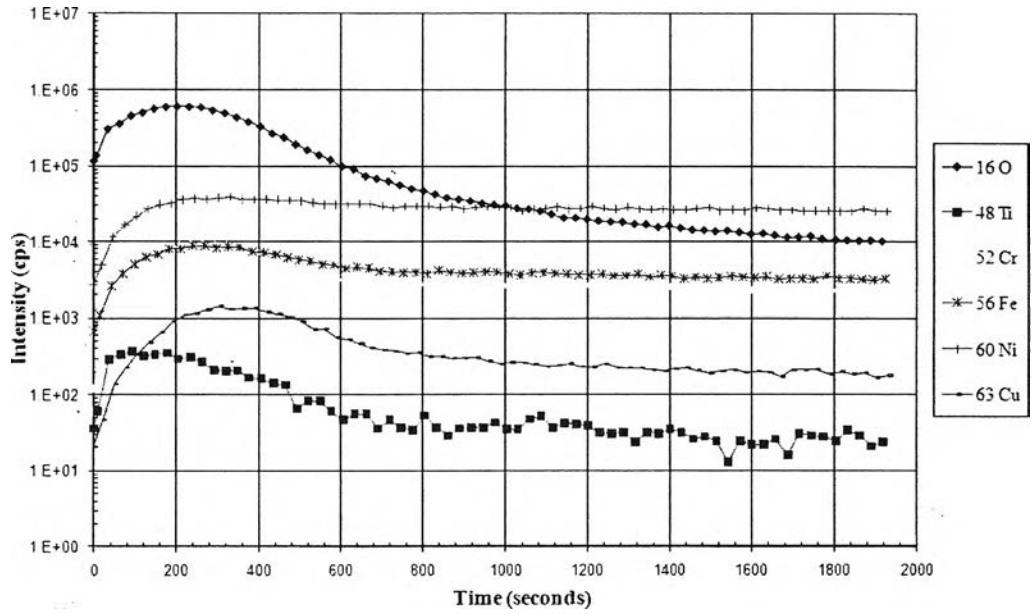

Figure 4.6 SIMS analysis on SG3 in Run 1.

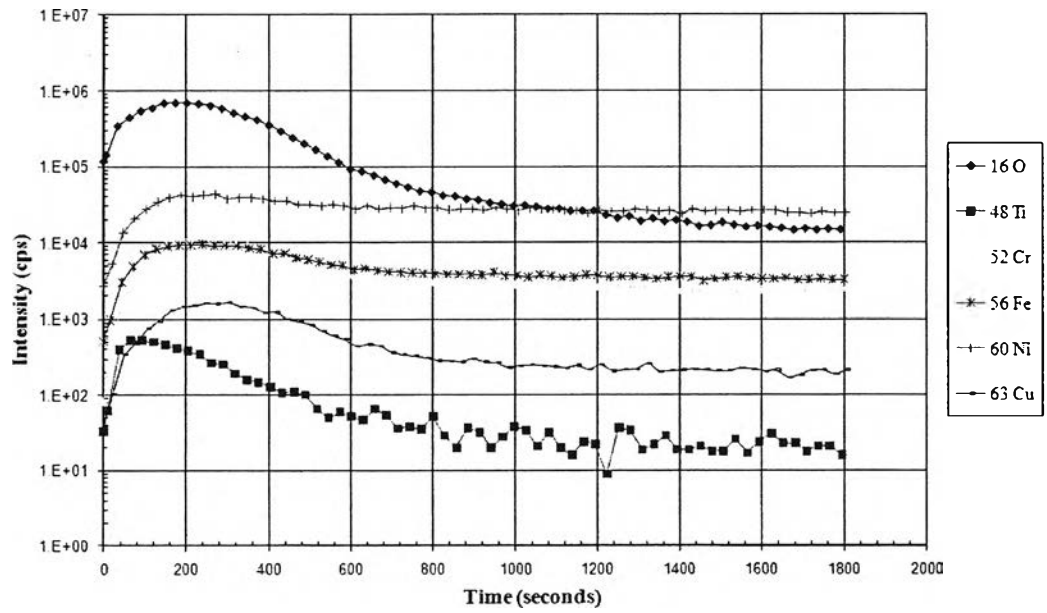

Figure 4.7 SIMS analysis on SG6 in Run 1.

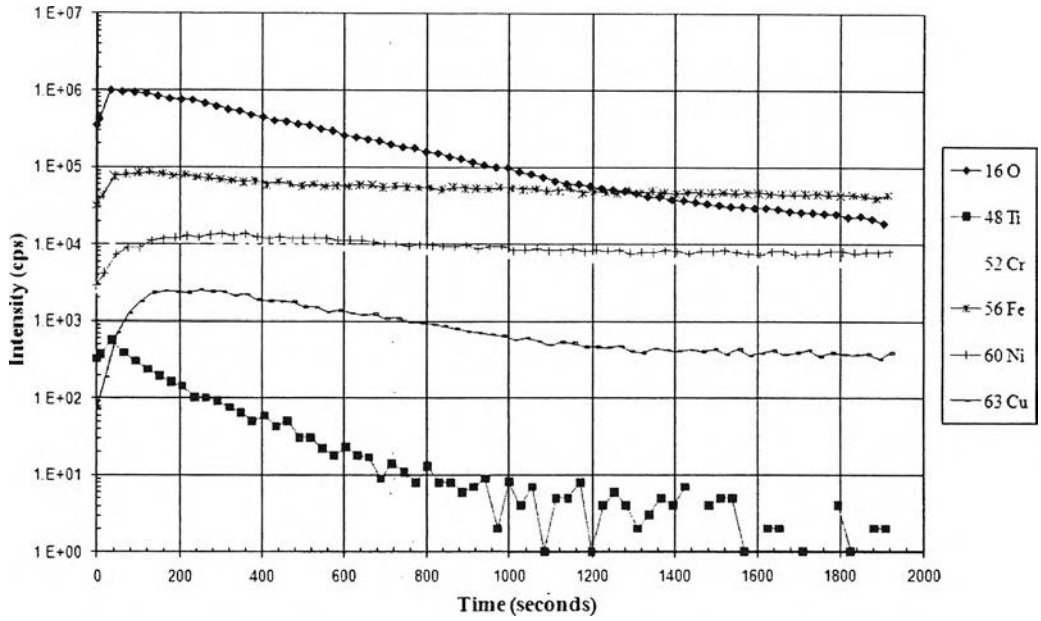

Figure 4.8 SIMS analysis on SS304 in Run 1.

4.1.1.3 XPS Analysis

Figure 4.9 shows a depth profile of exposed SG3 at the location facing the heater (-15°). The XPS profiles are consistent with the SIMS profiles, though they do not give detailed chemical information. They mainly indicate that the oxide film grown on SG3 was ~0.1 μm thick and was slightly enriched in Cr. This thickness was determined from the point where the intensity of oxygen reaches 50% of its initial value (~120 minutes of etch time) and calculated by the sputter rate at 1.2 nm/min based on an Al_2O_3/Al standard. Some boron content was observed in the oxide film by this analysis. It may have come from precipitation from residual solution after exposure. Also, Ti is indicated but Zr and Cu are not.

In addition, XPS was used to examine the chemical state of the oxide film grown on SG3. The survey signals in Table A.1 show that there are many elements found on the surface of SG3. Carbon and Cl are likely contaminants. The oxidation states of the main elements (Ni, Fe and Cr) were determined. Figure 4.10 shows the Ni $2p_{3/2}$ core level spectra of the oxide indicating that the three main components are metallic Ni, $Ni(OH)_2$ and NiO. Their position and peak size (percentage of area) are shown in Table A.2 in Appendix A1. The metallic Ni found in the Ni $2p_{3/2}$ spectrum may be due to some ion-beam reduction from either the

previous SIMS analyses or the previous XPS depth profile, but is also possible from the exposure under the reducing conditions of the coolant.

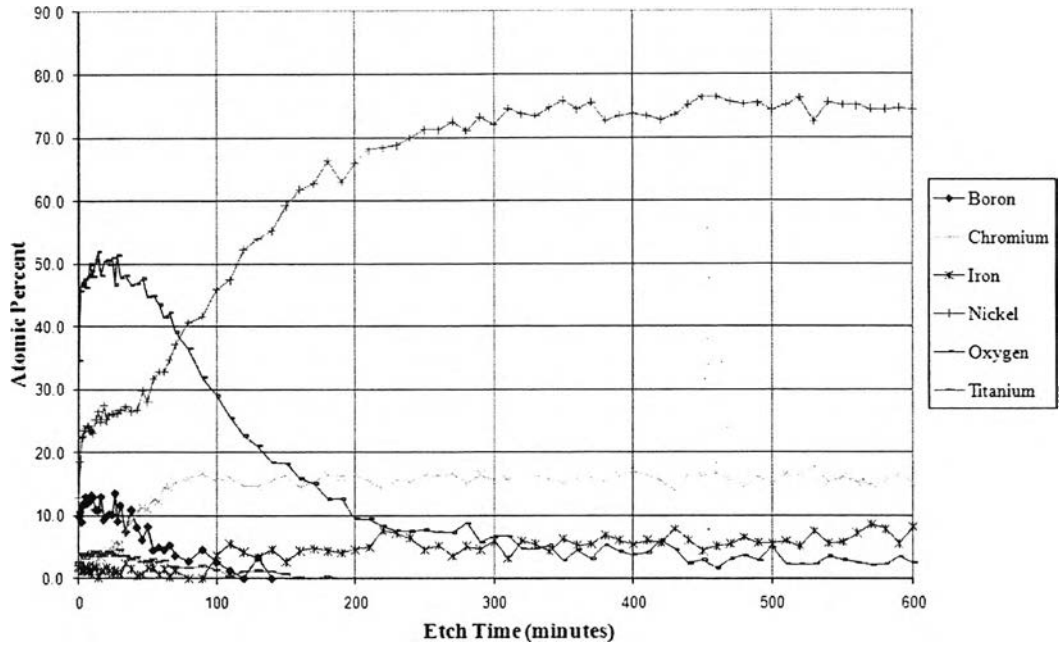

Figure 4.9 XPS depth profile on SG3 (-15°) in Run 1.

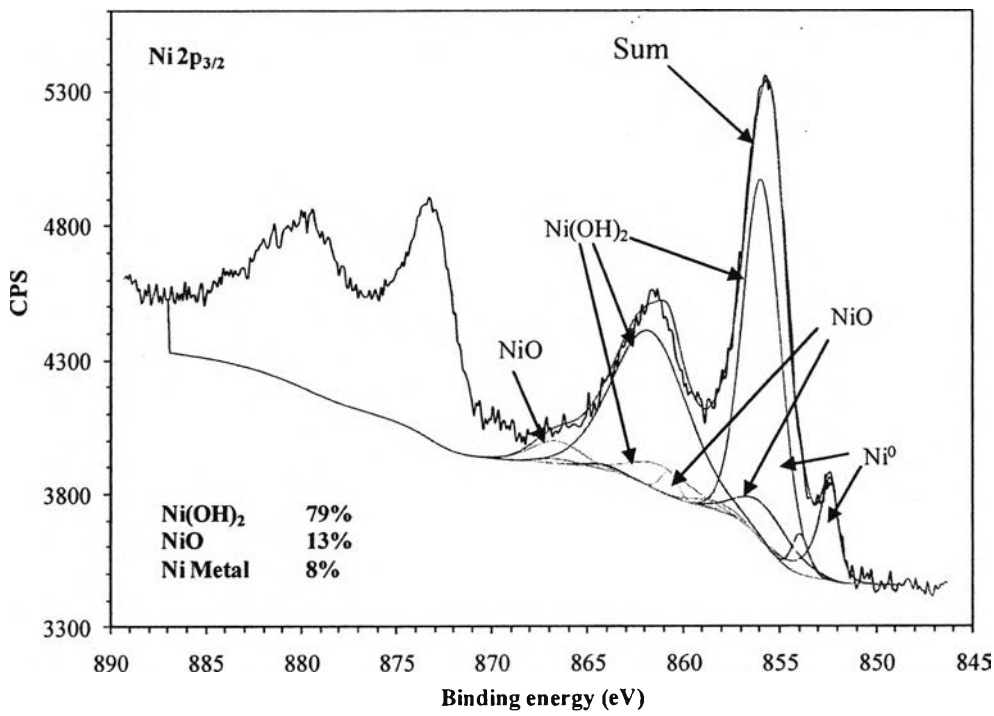

Figure 4.10 Ni $2p_{3/2}$ core level spectra of oxide film grown on SG3 in Run 1.

Figure 4.11 shows the Cr $2p_{3/2}$ core level spectra, which are characteristic of Cr^{3+}. The Cr^{3+} was detected in the form mainly of Cr_2O_3 but also with the possibility of $Cr(OH)_3$. Their position and peak size (percentage of area) are shown in Table A.3 in Appendix A1.

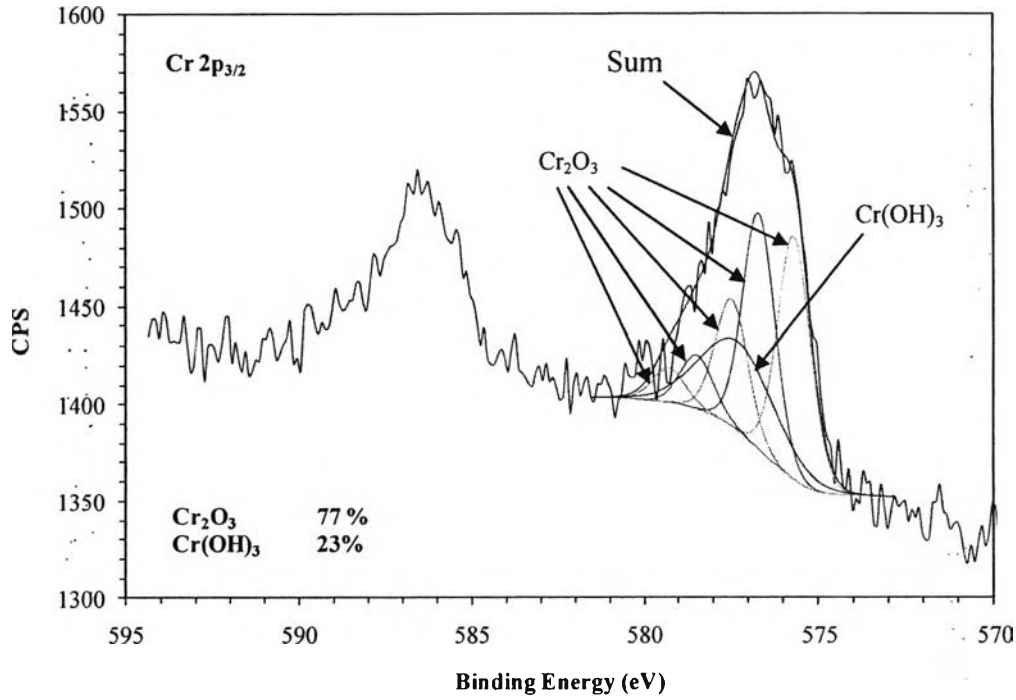

Figure 4.11 Cr $2p_{3/2}$ core level spectra of oxide film grown on SG3 in Run 1.

For Fe 2p spectra in general, Allen *et al.* (1974) found that they were particularly difficult to analyse because of a steeply rising background and broadened line widths. In this study, also, Fe chemical states could not be analysed because the Fe 2p peak was relatively weak and was overlapped with a Ni Auger signal, as shown in Figure 4.12.

The oxidation state of Ti was also determined. Figure 4.13 shows the Ti $2p_{3/2}$ core level spectra, which are characteristic of Ti^{4+}. This confirms the presence of titanium in the oxide, which may be in the form of $FeTiO_3$ (ilmenite) and/or TiO_2 (Lister *et al.*, 2002).

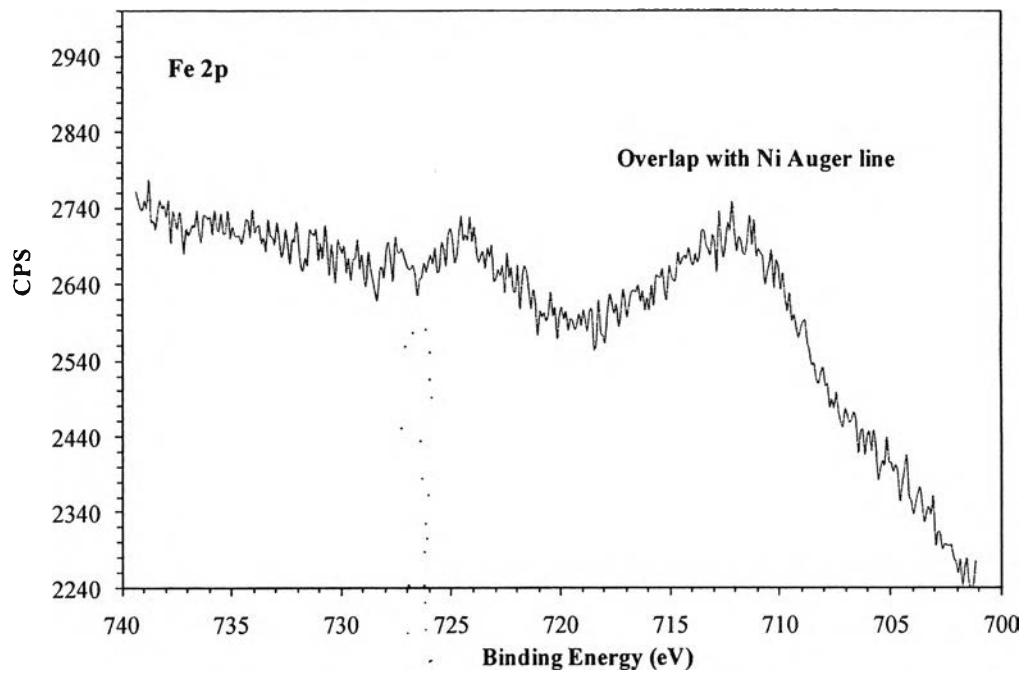

Figure 4.12 Fe 2p core level spectra of oxide film grown on SG3 in Run 1.

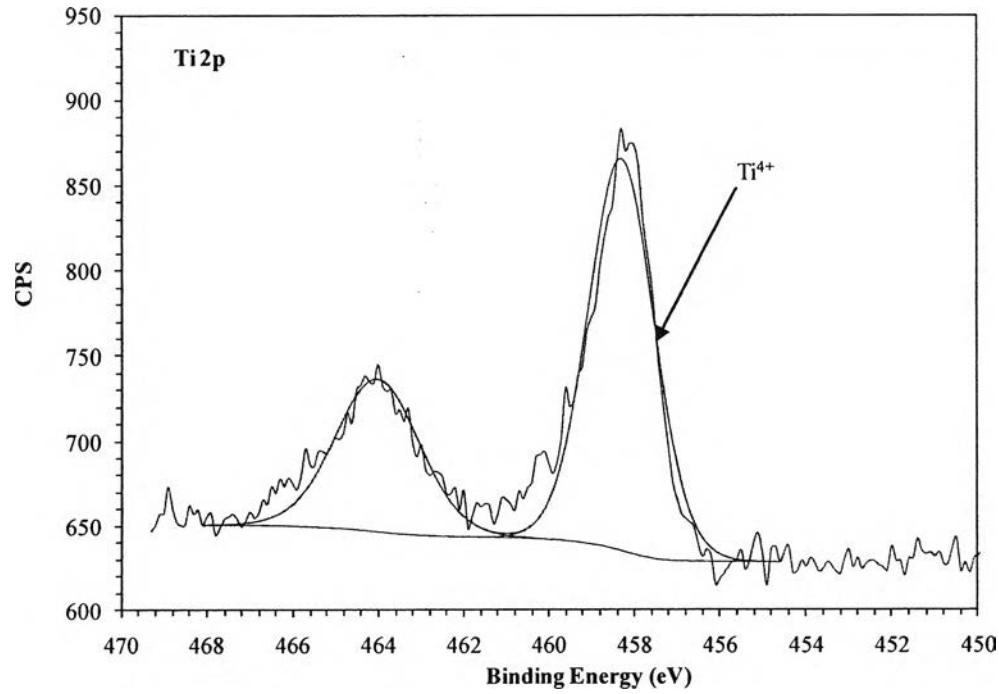

Figure 4.13 Ti 2p core level spectra of oxide film grown on SG3 in Run 1.

From the SIMS analysis, it was found that the oxide film was enriched in Fe and Cr. From the XPS analysis, the Cr $2p_{3/2}$ (which is characteristic of Cr^{3+}) could be as Cr_2O_3 (McIntyre *et al.*, 1979) or $FeCr_2O_4$ (McIntyre and Zetaruk, 1977). Chromium enrichment was always observed from the atomic N_{Cr}/N_{Fe} ratio as calculated from the total Cr $2p_{3/2}$ and total Fe 2p3/2 peaks (Machet *et al.*, 2002). From the quantitative XPS analysis shown in Table 4.8, the N_{Cr}/N_{Fe} ratio is 2. It indicates the presence of $FeCr_2O_4$.

Thus, the oxide film grown on Alloy 600 MA in this run should be composed of $FeCr_2O_4$, Cr_2O_3, $Cr(OH)_3$, NiO, $Ni(OH)_2$ and TiO_2 and possibly metallic Ni and $FeTiO_3$. The oxide thickness on the SG samples (Alloy 600 MA) is estimated to be 0.1 μm, which corresponds roughly to a corrosion rate of the underlying metal of 0.38 mdd (1.62 μm/a).

Table 4.8 Quantitative XPS analysis of oxide film grown on SG3 in Run 1 (at.%)

Core level spectra	Ni 2p	Fe 2p	Cr 2p	O1s	Ti 2p	Cr/Fe
SG3	5.1	0.3	0.6	27.5	0.7	2

4.1.2 Run 2

In this run, samples were exposed for five days to coolant of similar chemistry to that of Run 1 but without boron. During exposure, samples darkened; an example is shown in Figure 4.14. As shown in Figure 4.15, the color of SG3 in Run 2 was brighter (i.e. more metallic) than that of SG1 in Run 1, no doubt because of the shorter exposure time. The weight changes of samples are reported in Table 4.9. Some SG samples gained weight and some lost weight, while the weight of the SS304 sample remained unchanged. The Zircaloy-4 sample gained weight significantly more than the SG samples. From the result, however, it appears that most SG samples in Run 2 lost weight, compared with SG samples in Run 1. In this run, the coolant was not analysed after the exposure.

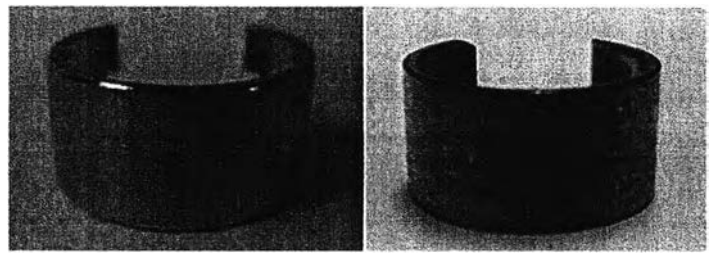

(a) (b)

Figure 4.14 SG3 sample band in Run 2 (a) before exposure and (b) after exposure.

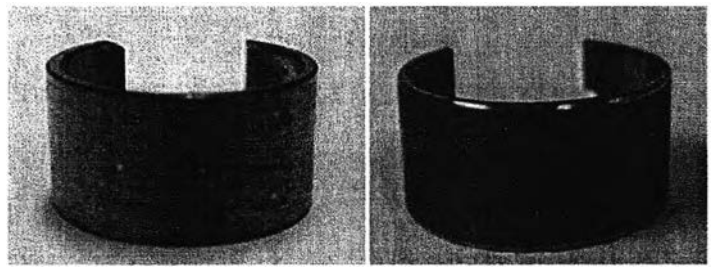

(a) (b)

Figure 4.15 Photographs of SG sample bands (a) SG3 in Run 2 and (b) SG1 in Run 1.

Table 4.9 Weight of the sample bands before and after exposure in Run 2

Sample	Surface Area (cm^2)	Before (g)	After (g)	Weight Change (mg)	Weight Change per Unit Area (mg/dm^2)
Zircaloy-4	4.17	0.9430	0.9437	+0.7	+16.79
SS304	4.68	2.0660	2.0660	0.0	0.0
SG1	6.24	4.4047	4.4046	-0.1	-1.60
SG2	6.24	4.3854	4.3858	+0.4	+6.41
SG3	6.24	4.3856	4.3855	-0.1	-1.60
SG4	6.24	4.3439	4.3438	-0.1	-1.60
SG5	6.24	4.4694	4.4696	-0.2	-3.20
SG6	6.24	4.3973	4.3972	-0.1	-1.60

In this run, SG2, SG3, SS304 and Zirc-4 were analysed with EDX and SEM and were compared with the samples in Run 1 to examine the effect of exposure time and boron on oxide formation. The results are presented and discussed as follows:

4.1.2.1 EDX and SEM Analyses

SG2 and SG3 were analysed with EDX on the convex surface. The EDX results are shown in Table 4.10. The elemental compositions before and after exposure are different, indicating the presence of oxide films. The elemental compositions of SG2 and SG3 were slightly different. From the EDX results, the weight percentage of Fe and Ni of SG3 sample after exposure decreased and the weight percentage of Cr increased, corresponding to the changes observed on SG1 in Run 1. This results from the preferential dissolution of Fe and Ni from the substrate alloy during the first stage of corrosion (Carrette *et al.*, 2003), as discussed earlier and possibly due to an increase in both chromium and oxygen concentration. For SG2, the weight percentage of Fe, Ni and Cr during exposure increased and the total weight percentage of elements exceeded 100. This was apparently caused by a surface effect, since the surfaces of samples are convex and not every analysis would have been done at exactly the same angle of incidence. It should be kept in mind that EDX results are only semi-quantitative and in these cases influenced by the underlying metal.

Copper was found in significant amounts after exposure on SG2 but not on SG3. Zirconium from the heater cladding material was also found on SG2 and SG3 after exposure. The weight percentage of O on SG3 during exposure increased because of the formation of an oxide film.

Table 4.10 EDX result from the convex surface of SG2 and SG3 in Run 2

Sample	Wt%						
	Ni	Fe	Cr	Ti	Cu	Zr	O
SG2	74.01	10.16	17.3	0.29	1.15	0.07	**
SG3	69.28	8.53	16.61	0.29	-	0.06	5.23
Before exposure	70.83	9.63	15.40	0.39	*	-	2

*was not recorded

**cannot be determined from difference from 100, since the total weight percentage of elements on SG2 exceeds 100

Next, SEM was performed on the convex surfaces of SG2, SG3, SS304 and Zirc-4. Figure 4.16 shows the surface morphology of SG2 and SG3. It shows that the surfaces of SG2 and SG3 were almost identical. They were covered with needle-like oxides whose distribution was not uniform. They seem to be associated with scratches or defects on the surfaces, possibly because these areas are preferential sites for oxidation. From a comparison with the oxide formed on SG3 in Run 1, the sizes of the oxide needles are slightly different possibly due to the exposure time and/or the effect of boron, and the needle-like oxide coverage on SG3 in Run1 was greater, possibly because of longer exposure time and/or the effect of boron.

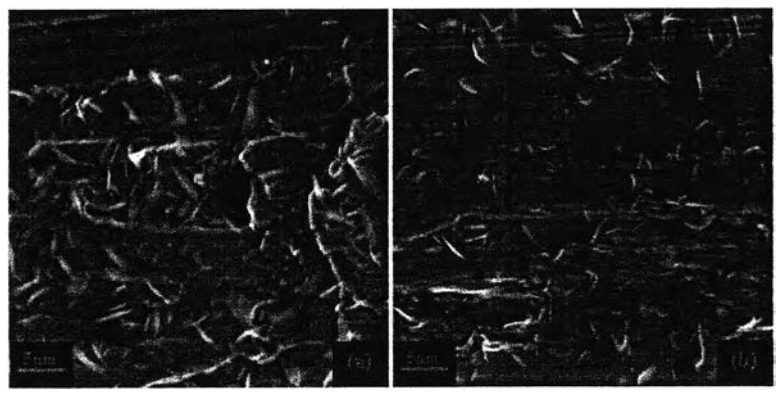

Figure 4.16 SEM images of (a) SG2 and (b) SG3 in Run 2.

The surface morphology of SS304 in Run 2 is shown in Figure 4.17 (a) and (b). A crystallite layer covers a layer having no obvious crystallinity. Table 4.11, comparing the elemental compositions of crystallites with that of the underlying layer, shows that the Cr content in the crystallite layer was lower than that in the underlying layer, and the Fe/Cr ratio in the crystallite layer was higher than that in the underlying layer. It indicates that the crystallite layer was Fe-rich and the underlying layer was Cr-rich, in agreement with the observations on SS304 in Run 1. However, the oxides formed on SS304 in Run 1 and Run 2 were different in size and density of crystallites, as shown in Figure 4.17. This may be due to the different exposure time. It may be explained, as reported by Tapping *et al.*, (1986), that at the start of exposure, the nucleation and growth of oxide occur rapidly resulting in the formation of big but relatively sparse crystallites as observed on SS304 in Run 2. With increasing exposure, oxide nucleation still occurs but dissolution begins to compete with crystal growth, with the result that crystallite density increases but crystallite size decreases - as observed on SS304 in Run 1. However, this would seem to contradict the theory of Ostwald ripening, which suggests that the smallest particles (with the highest surface energy) tend to dissolve to benefit the largest particles. Possibly, exposure times for both runs were too short for the transition from nucleation and growth to ripening to occur. According to Madras and McCoy (2004), the transition from nucleation and growth to ripening occurs over a long time period. However, this observation is possibly due to the effect of boron that will be confirmed later. The crystallites on SS304 in Run 1 had a narrow size range of 0.11 to 0.57 μm with an average of ~0.23 μm, while the size range on SS304 in Run 2 varied from 0.17 to 0.74 μm with an average of ~0.36 μm.

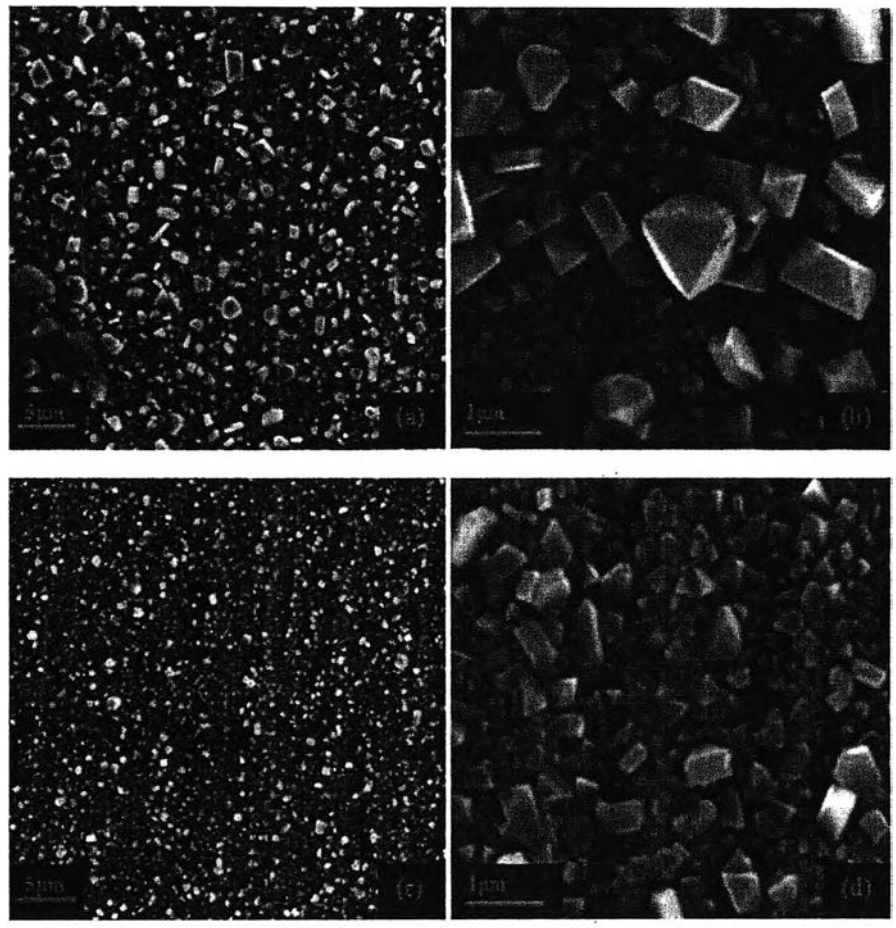

Figure 4.17 SEM images of SS304 in Run 2 (a and b) and in Run 1 (c and d).

Table 4.11 EDX analyses on the convex surface of SS304 in Run 2

Position	Wt%					
	Ni	Fe	Cr	Ti	O	Fe/Cr
Crystallite layer	2.02	63.84	3.23	0.27	30.91	19.76
Underlying layer	10.47	55.25	20.92	0.09	13.36	2.72

Figure 4.18 shows the surface morphology of Zirc-4 on its convex surface. Elongated oxide grew in cavities on the surface. The EDX result, shown in Table 4.12, indicates that the elongated oxides were probably ZrO_2. It is interesting to note that the oxide on Zirc-4 in Run 2 was similar to that on Zirc-4 in

Run 1, even though their exposure times were different. This observation may result from one of three possible hypotheses. First: since the exposure times for both runs were not too much different, differences were minimal. Second: it is due to the effect of boron and lithium. It is well known that a high lithium concentration in water (> approximately 30-100 ppm) can cause the accelerated corrosion of zirconium alloys when only lithium as lithium hydroxide is added to the water (McDonald *et al.*, 1984). Even though the lithium concentration in Run 2 was quite low (~0.27 ppm), it may have concentrated in the pores in ZrO_2 layers under boiling heat transfer conditions, resulting in accelerated corrosion (Cox *et al.*, 1996). Moreover, Pêcheur *et al.* (1993) noted that the presence of boron can reduce the corrosion rate of zirconium alloys because it inhibits lithium incorporation into the oxide film and counteracts the acceleration of corrosion by lithium. Therefore, it is likely that Zirc-4 exposed to the coolant in Run 2 containing only lithium was corroded more than Zirc-4 exposed to the coolant in Run 1 containing both boron and lithium. Third: the SEM only shows the top of the film; they may have different thicknesses.

However, Zirc-4 in Run 2 had higher corrosion rate than Zirc-4 in Run 1, as shown in Table 4.13. It is possibly because Zirc-4 in Run 2 was exposed in the coolant without boron concentration and for the short time (5 days).

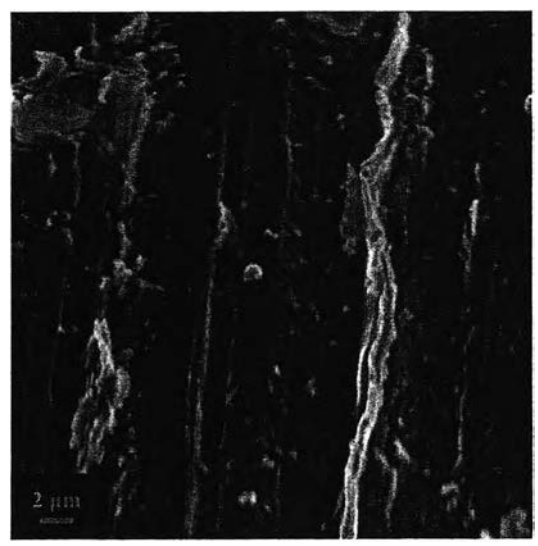

Figure 4.18 SEM image of Zirc-4 in Run 2.

Table 4.12 EDX analyses on the convex surface of Zirc-4 in Run 2

Position	Wt%			
	Fe	Zr	Sn	O
Platelet oxide	0.25	67.76	0.87	31.12

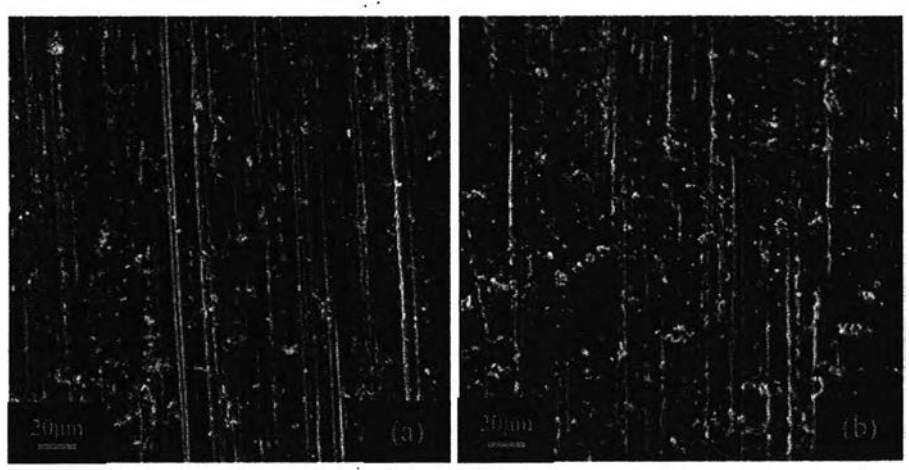

Figure 4.19 Comparison of surface morphologies of Zirc-4 in Run 1 (a) with Zirc-4 in Run 2 (b).

Table 4.13 Comparison of Zirc-4 corrosion rate between Run 1 and Run 2

Zirc-4 sample	Surface Area (dm^2)	Weight Change (mg)	Exposure Time (days)	Corrosion rate (mdd)
Run 1	0.0417	+0.8	10	1.92
Run 2	0.0417	+0.7	5	3.36

From the results of Run 1 and Run 2, it is concluded that the surface morphology of samples is affected by the time of exposure and the chemical environment (lithium and boron).

4.1.3 Run 3

Exposed SG3 in Run 3 was slightly darker than exposed SG1 in Run 1, even though they were exposed under similar conditions for the same time, possibly because they experienced slightly different coolant temperatures. Table 4.14 shows weight changes of the samples after Run 3. All samples gained weight fairly significantly, compared with weight changes of the samples in Run 1.

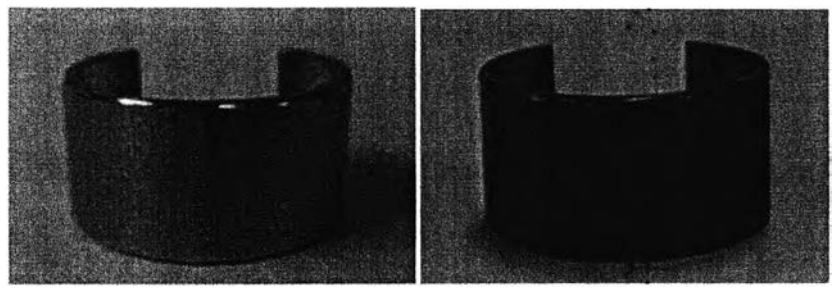

Figure 4.20 SG3 sample band in Run 3 (a) before exposure and (b) after exposure.

Table 4.14 Weight of the sample bands before and after exposure in Run 3

Sample	Surface Area (cm^2)	Before (g)	After (g)	Weight Change (mg)	Weight Change per Unit Area (mg/dm^2)
Zircaloy-4	4.17	0.9306	0.9327	+2.1	+50.36
SS304	4.68	2.0815	2.0821	+0.6	+12.82
SG1	6.17	4.3670	4.3687	+1.7	+27.55
SG2	6.17	4.3037	4.3052	+1.5	+24.31
SG3	6.17	4.3614	4.3628	+1.4	+22.69
SG4	6.17	4.3533	4.3547	+1.4	+22.69
SG5	6.17	4.3705	4.3717	+1.2	+19.45
SG6	6.17	4.3378	4.3393	+1.5	+24.31

After exposure, boron concentration, pH and iron concentration of the coolant were determined and the results are shown in Table 4.15. From the results,

boron concentration after exposure was higher than that before exposure. However, the difference is within the measurement error. The pH values before and after exposure were not significantly different. The concentrations of Ni, Fe and Mn in the coolant increased during exposure, no doubt due to the dissolution of these metal ions from the corrosion products and the base materials of SG and SS304 samples. From a comparison with the concentrations of these metal ions in the coolant in Run 1, the concentrations of the metal ions in Run 1 seemed higher than those in Run 3. This is possibly effected by the solubility of these metal ions in the coolant at slightly different temperatures and pHs. The higher Zn concentration after exposure is possibly due to the residual Zn contamination from the lubricant used in this work (ZnO is one of its constituents) and/or from the previous work (the autoclave was operated with water containing Zn).

Table 4.15 Coolant chemistry before and after exposure in Run 3

Conditions	Before	After
Boron concentration (ppm)	1989	2047
pH @ room temperature	6.42	6.43
$pH_{295°C}$	7.01	7
Fe concentration (ppb)	-	2.8±1.0
Ni concentration (ppb)	-	10.0±0.93
Mn concentration (ppb)	-	11.9±3.1
Zn concentration (ppb)	0.4*	7.1±1.1

*from the de-ionized water

In this run, SG3, SS304 and Zirc-4 were analysed with EDX and SEM and only the SS304 sample was analysed with XPS. The results in this run were compared with those in Run 1 to examine the effect of SG heat treatment and bulk temperature on oxide formation. The results are presented and discussed as follows:

4.1.3.1 EDX and SEM Analyses

SG3 was analysed with EDX on its convex surface and the results are shown in Table 4.16. It shows that the elemental compositions before and after exposure were different, indicating the growth of an oxide film on the surface. The weight percentage of Fe and Ni decreased during exposure, while the weight percentage of Cr increased. This was due to the preferential dissolution of Fe and Ni from the substrate alloy during the first stage of corrosion (Carrette *et al.*, 2003) and possibly because of the increase of oxygen in the alloy. In addition, the weight percentages of Ti, Cu and Zr during exposure increased, most likely due to the formation of the oxides of these metals and/or the incorporation of these metals into the oxide film. Such Ti and Zr possibly come from the test section and the heater cladding material. The Cu possibly comes from the SG alloys and/or the lubricant.

Table 4.16 EDX result from the convex surface of SG3 in Run 3

Sample	Wt%						
	Ni	Fe	Cr	Ti	Cu	Zr	O
SG3	59.8	9.23	16.1	0.95	1.04	0.14	10.99
Before exposure	71.56	9.41	15.09	0.29	*	-	2.54

*was not recorded

Figure 4.21 shows the surface morphology of SG3. SG3 was covered with the needle-like oxides whose size and coverage were slightly different from those on SG3 in Run 1. The size of oxide needles in Run 3 was slightly smaller but the oxide coverage in Run 3 was higher than those in Run 1. This is probably because of the higher coolant temperature resulting in the higher oxide nucleation rate (Mullin, 1993) and/or the effect of heat treatment. Moreover, it is found that the oxide coverage on SG3 in Run 3 (Alloy 600 TT) was uniform throughout the surface more than that on SG3 in Run 1 (Alloy 600 MA) possibly due to the effect of heat treatment.

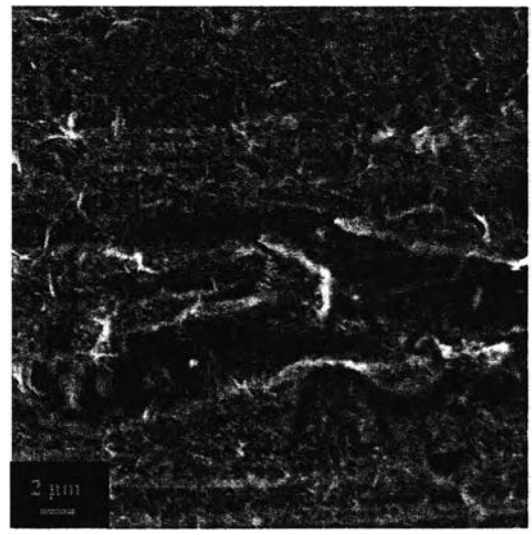

Figure 4.21 SEM image of SG3 in Run 3.

In Figure 4.22 (b), SS304 in Run 3 is seen to be covered with a layer of tiny crystals with some larger crystallites. The underlying oxide layer is not clearly seen because of high crystallite coverage. These oxides were analysed for the compositions with EDX as tabulated in Table 4.17. As mentioned earlier, the EDX results also include the composition of the underlying metal. The composition of the underlying layer then was determined by EDX performed on the layer of tiny crystals. It was found that the Cr content in the large crystallite was lower, while the Fe/Cr ratio in the large crystallite was higher than those in the underlying layer indicating that the large crystallite was Fe-rich and the underlying layer was Cr-rich.

The major differences between SS304 surfaces exposed to the coolant in Run 3 and in Run 1 were the crystallite size and coverage. The crystallites in Run 3 were smaller, but their coverage was higher, than those in Run 1, as shown in Figure 4.22, possibly because of the different coolant temperature. Mullin (1993) suggests that the nucleation rate increases with increasing temperature. Since the coolant temperature in Run 3 (300°C) was higher than that in Run 1 (295°C), the crystal nucleation in Run 3 would occur more rapidly than that in Run 1, resulting in the higher crystallite coverage. The effect may have been augmented by a higher corrosion rate at the higher temperature. Note that higher crystal nucleation results in lower crystal growth for the same amount of corrosion.

Figure 4.23 shows the surface morphology of Zirc-4 after Run 3. Elongated oxides were observed, especially in the grooves. Moreover, small crystals were scattered on the surface. According to the EDX results in Table 4.18, the elongated oxide should be ZrO_2 and the small crystals should be CuO (Tenorite or black copper oxide). A magnified SEM image of a small crystal is shown in Figure 4.24. The Cu in the coolant possibly comes from the SG alloys. The oxide morphology of Zirc-4 in Run 3 was similar to that in Run 1, presumably because they were exposed to similar coolant conditions.

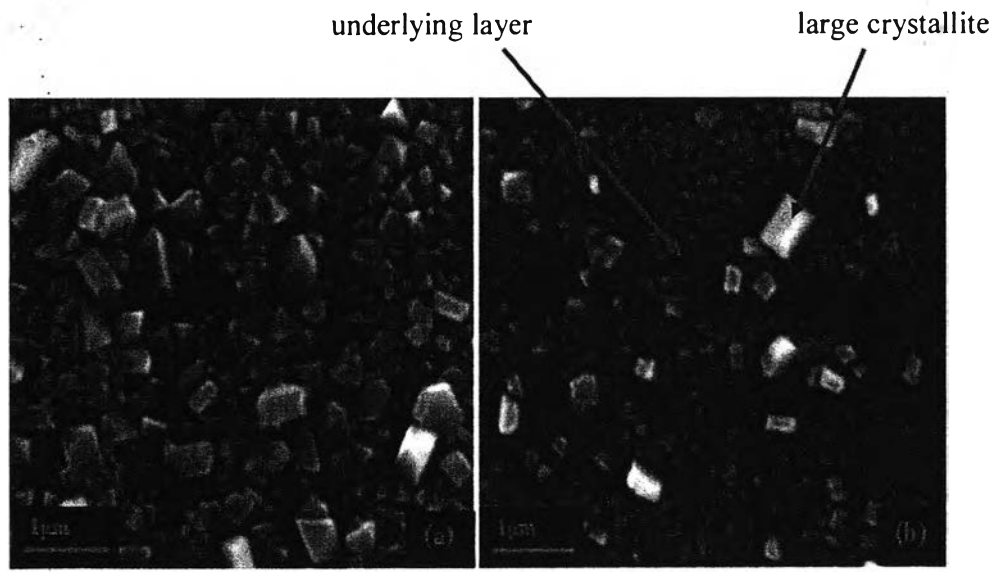

Figure 4.22 SEM image of SS304 in (a) Run 1 and (b) Run 3.

Table 4.17 EDX analyses on the convex surface of SS304 in Run 3

Position	Wt%					
	Ni	Fe	Cr	Ti	O	Fe/Cr
Crystallite layer	6.13	57.61	11.18	0.71	22.61	5.15
Underlying layer	10.07	61.67	20.5	0.22	4.49	3.01

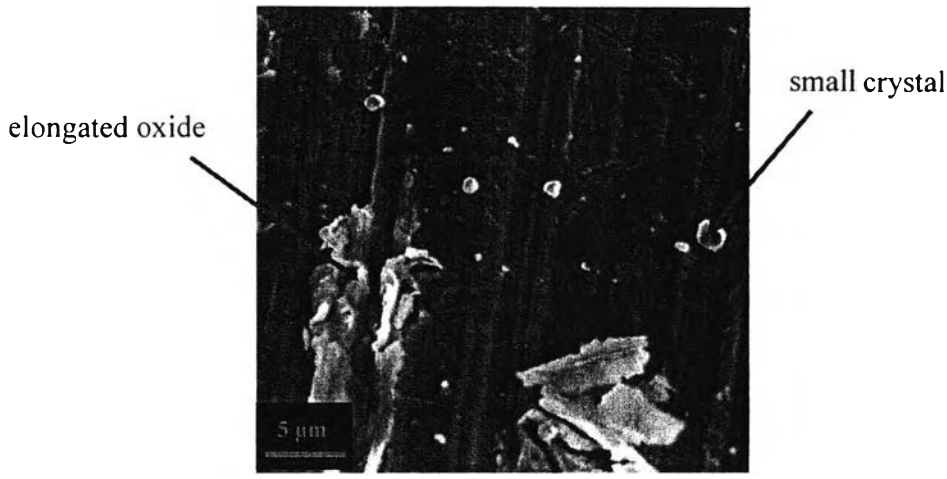

Figure 4.23 SEM image of Zirc-4 in Run 3.

Table 4.18 EDX analyses on the convex surface of Zirc-4 in Run 3

Position	Wt%					
	Ni	Fe	Cu	Zr	Sn	O
Elongated oxide	-	0.32	-	77.77	1.04	20.87
Small crystal	1.71	-	80.41	13.58	-	4.3

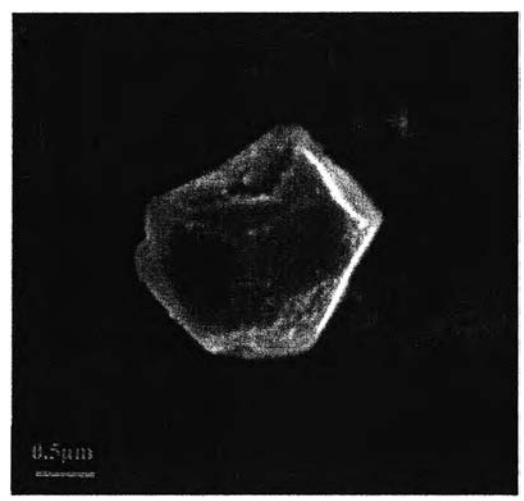

Figure 4.24 Magnified SEM image of small crystal on Zirc-4 surface in Run 3.

Table 4.19 shows corrosion rate of Zirc-4 in Runs1-3. As discussed previously, Zirc-4 in Run 2 had higher corrosion rate than Zirc-4 in Run 1 because of the shorter exposure time and no boron concentration, so Zirc-4 in Run 2 was expected to have higher corrosion rate than Zirc-4 in Run 3. However, from the result, it appears that the corrosion rate of Zirc-4 in Run 3 was higher than that in Run 2 possibly due to the higher coolant temperature. This indicates that the corrosion rate of Zirc-4 was affected by temperature more than the exposure time and boron concentration. Therefore, from a comparison between the corrosion rates of Zirc-4 in Run 3 and that in Run 1, Zirc-4 in Run 3 had much higher corrosion rate, certainly due to the higher coolant temperature.

Table 4.19 Corrosion rates of Zirc-4 in Run 1, Run 2 and Run 3

Zirc-4 sample	Surface Area (dm^2)	Weight Change (mg)	Exposure Time (days)	Corrosion rate (mdd)
Run 1	0.0417	+0.8	10	1.92
Run 2	0.0417	+0.7	5	3.36
Run 3	0.0417	+2.1	10	5.04

4.1.3.2 XPS Analysis

XPS was performed on a SS304 sample to examine the chemical states of the oxide film before and after sputtering. The oxide layer was sputtered through until the metal had been reached (the sizes of all element peaks stayed the same). There were six sputtering levels, each corresponding to 50 nm. The survey spectra before sputtering showed peaks of Zn, Ni, Fe, Cr, Ti, C and O at different binding energies (BE), as shown in Figure A.4 in Appendix A. The peak of O was very strong, indicating the oxidation on the surface of sample. According to the comparison of binding energies of these peaks with the reference energies (Physical Electronics, 1995), these chemical states can be assigned to oxides as shown in Table 4.20.

Table 4.20 Possible oxides on SS304 surface before sputtering in Run 3

Peak	Binding Energy (eV)	Possible Oxide States
Zn $2p_{3/2}$	1022.0	ZnO
Ni $2p_{3/2}$	856.3	$Ni(OH)_2$*
Fe $2p_{3/2}$	710.0	FeO, Fe_2O_3
Cr $2p_{3/2}$	577.1	Cr_2O_3
Ti $2p_{3/2}$	458.3	TiO_2

*by comparison with published data (Machet *et al.*, 2004)

Since the Fe $2p_{3/2}$ peak was observed at a BE of 710.0 eV, which was in between the BEs of FeO (709.5 eV) and Fe_2O_3 (710.9 eV), it is possible that the Fe $2p_{3/2}$ peak is characteristic of Fe^{2+} or Fe^{3+}. Therefore, the Fe $2p_{3/2}$ spectra not only could be FeO and Fe_2O_3, but also could be $Ni_xFe_{3-x}O_4$ ($x \leq 1$). From the quantitative XPS analysis, as shown in Table 4.21, the atomic N_{Fe}/N_{Ni} ratio as calculated from the total Fe $2p_{3/2}$ and total Ni $2p_{3/2}$ peaks is 2.45. This value is in good agreement with that expected from the presence of $Ni_{0.87}Fe_{2.13}O_4$, as commonly observed in the outer oxide layer of SS304 (Lister, 2003). Moreover, from the calculation, the atomic percentages of the metal ions in Table 4.21 are consistent with the possible oxides in Table 4.20 and it indicates the surplus oxygen in the oxide, which was greater than the oxygen required to form those possible oxides.

Thus, the outer oxide layer of SS304 possibly consisted of ZnO, $Ni(OH)_2$, FeO, Fe_2O_3, Cr_2O_3, TiO_2 and $Ni_{0.87}Fe_{2.13}O_4$. Since there was no Zn addition in the coolant in this run, Zn was likely as a contaminant from the de-ionized water. Titanium came from the test section.

Table 4.21 Quantitative XPS analysis of oxide film grown on SS304 in Run 3 before sputtering (at.%)

Core Level Spectra	Zn $2p_{3/2}$	Ni $2p_{3/2}$	Fe $2p_{3/2}$	Cr $2p_{3/2}$	Ti $2p_{3/2}$	C $2p_{3/2}$	O $2p_{3/2}$	Fe/Ni
SS304	11.7	3.5	8.6	5.3	1.9	16	53	2.45

Figure 4.25 shows spectra of Ni $2p_{3/2}$ during sputtering. It seems that two components were detected in these spectra: a signal of metallic nickel at a BE of 852.9 eV and another signal at a BE of 854.5 eV, which is attributed to $Ni(OH)_2$ or NiO. The peak of the latter signal was relatively shallow and broad, possibly due to the small amount of nickel oxides and an overlapping of nickel oxide peak and metallic Ni peak (resulting of the dissolution of metallic Ni from the base metal). The signal of the nickel oxides disappeared after first sputtering and with increased sputtering level the signal of metallic Ni increased continuously until the third level, after which it stayed the same. This means that most of nickel oxides were in the outer oxide layer.

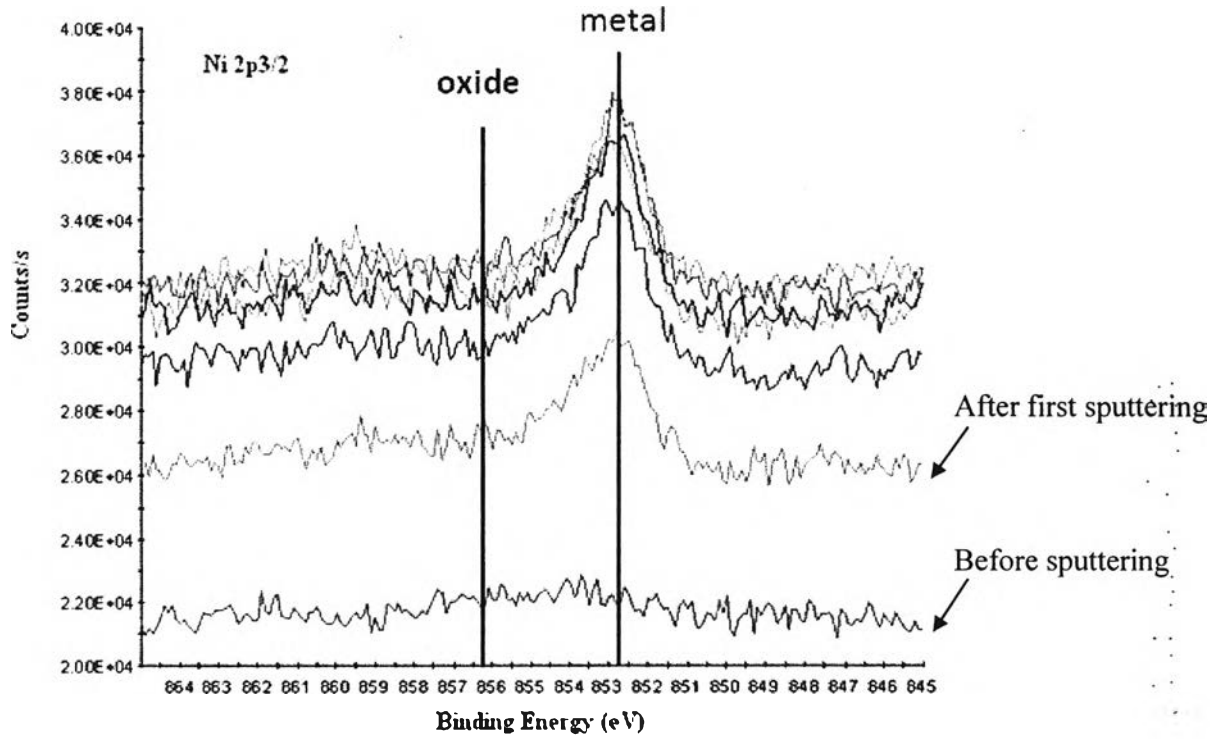

Figure 4.25 Ni $2p_{3/2}$ core level spectra of oxide film grown on SS304 as function of sputtering (Run 3).

The changes in Fe $2p_{3/2}$ spectra with sputtering are shown in Figure 4.26. There were two components detected in these spectra; a signal of metallic iron at a BE of 707.0 eV and a signal of iron oxides at a BE of 710.0 eV. The signal of iron oxides was highest at the surface before sputtering and then decreased with increasing sputtering level until it disappeared after the third sputtering. The signal of metallic Fe was observed after the first sputtering and then increased with increasing sputtering level until the third level, after which it stayed the same. These indicate that most of iron oxides were in the outer oxide layer and some of them were in the inner oxide layer, possibly as iron chromite.

According to the Cr $2p_{3/2}$ core spectra (Figure 4.27), the signal at a BE of 577.1 eV, which is attributed to Cr_2O_3, increased during the first sputtering and then decreased after the second sputtering until it disappeared after the fourth sputtering. Whilst the signal of Cr_2O_3 decreased, the signal at a BE of 574.1 eV, which is attributed to metallic Cr, increased until the fourth sputtering, after

which it stayed the same. From these observations, it is likely that Cr_2O_3 was observed in the inner oxide layer more than in the outer oxide layer.

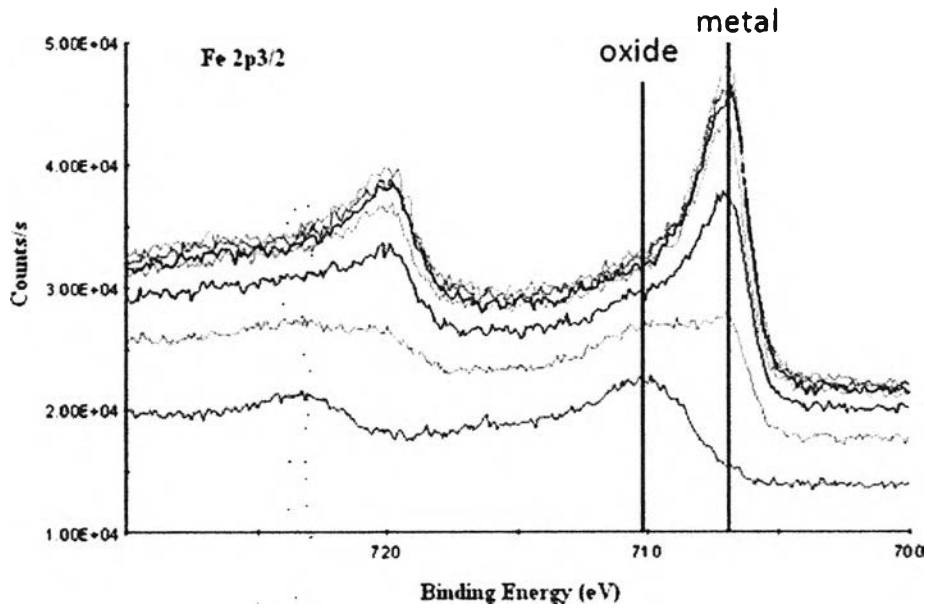

Figure 4.26 Fe $2p_{3/2}$ core level spectra of oxide film grown on SS304 as function of sputtering (Run 3).

Figure 4.28 shows the spectra of Ti $2p_{3/2}$. The signal at a BE of 458.3 eV, which is characteristic of Ti^{4+}, was observed only before sputtering, indicating the presence of Ti in the outer oxide layer, possibly in the form of TiO_2. The spectra of Zn $2p_{3/2}$ are shown Figure 4.29. The signal of Zn $2p_{3/2}$ was also observed only on the oxide before sputtering, at a BE of 1022 eV, possibly due to Zn contamination from the de-ionized water and lubricant.

From the spectra of O 1s, as shown in Figure 4.30, the signal decreased with increasing sputtering level until the fifth level, after which it stayed almost the same. The thickness of the oxide film can be estimated from the point where the intensity of the O 1s signal reached 50% of its initial value (after third sputtering). Therefore, the thickness of the oxide film on SS304 was approximately 0.15 μm.

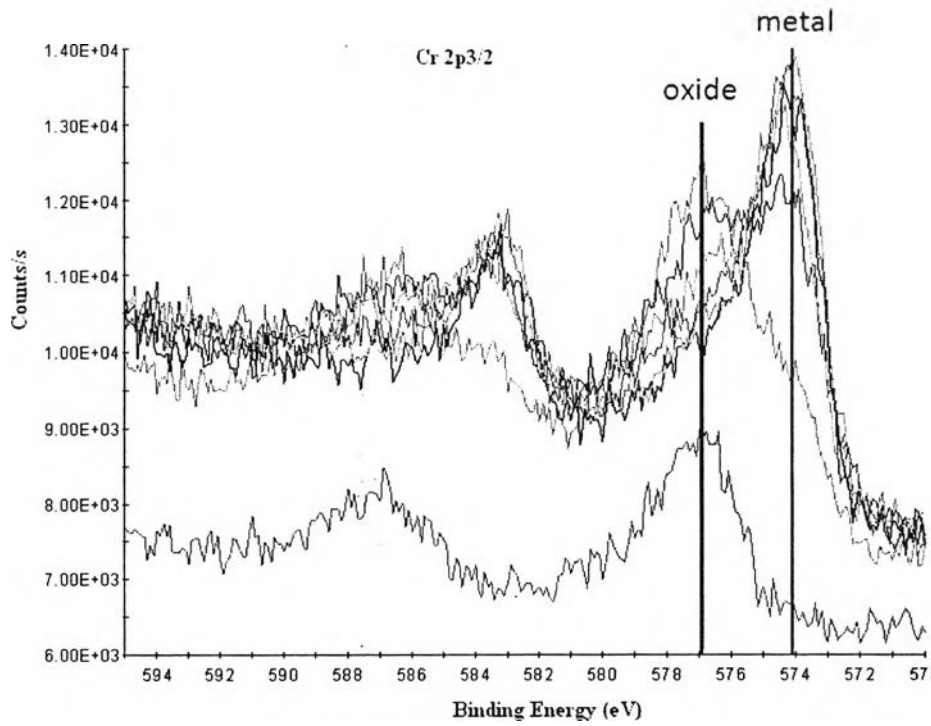

Figure 4.27 Cr $2p_{3/2}$ core level spectra of oxide film grown on SS304 as function of sputtering (Run 3).

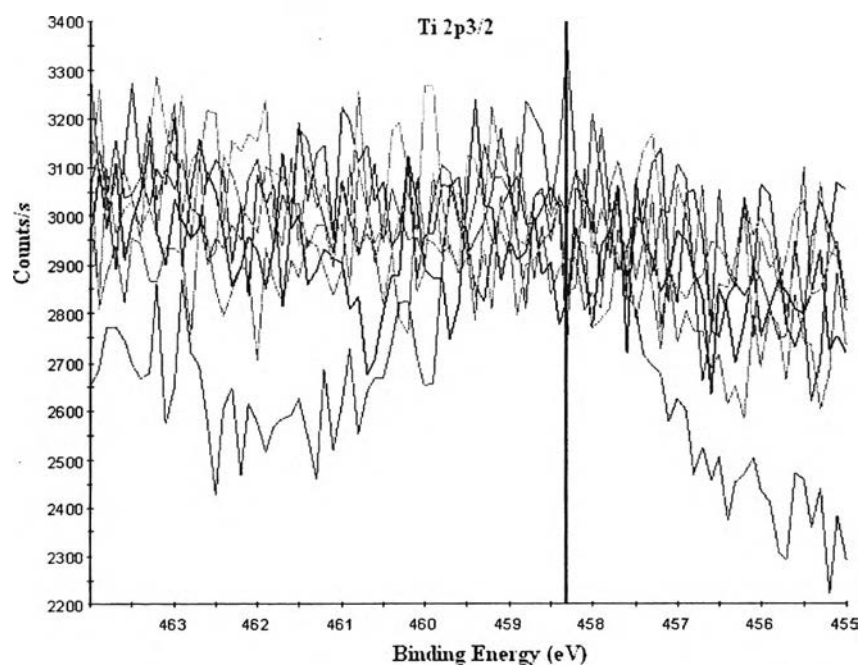

Figure 4.28 Ti $2p_{3/2}$ core level spectra of oxide film grown on SS304 as function of sputtering (Run 3).

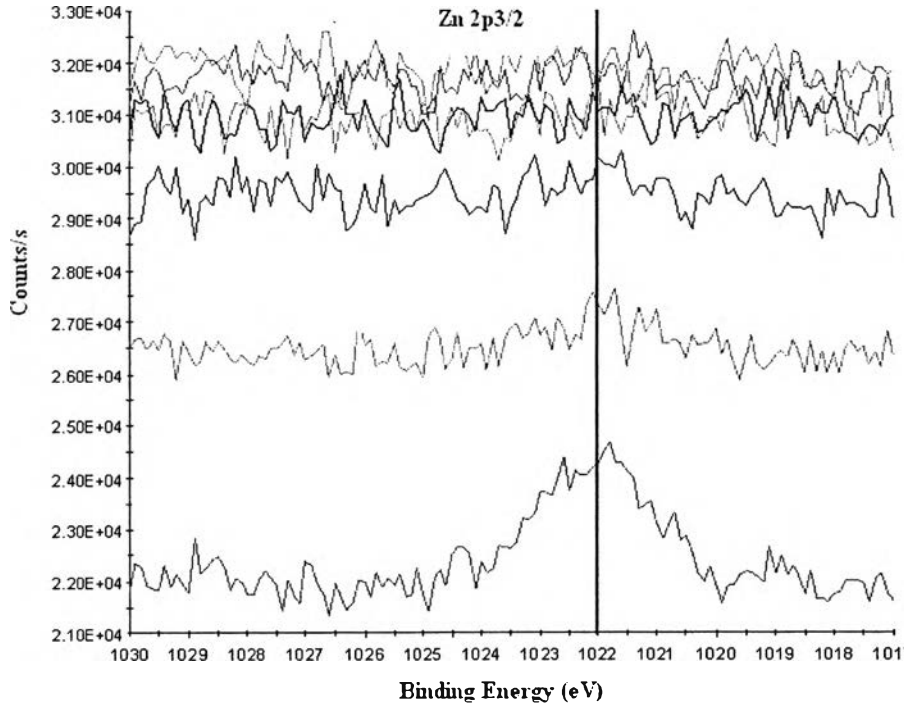

Figure 4.29 Zn $2p_{3/2}$ core level spectra of oxide film grown on SS304 as function of sputtering (Run 3).

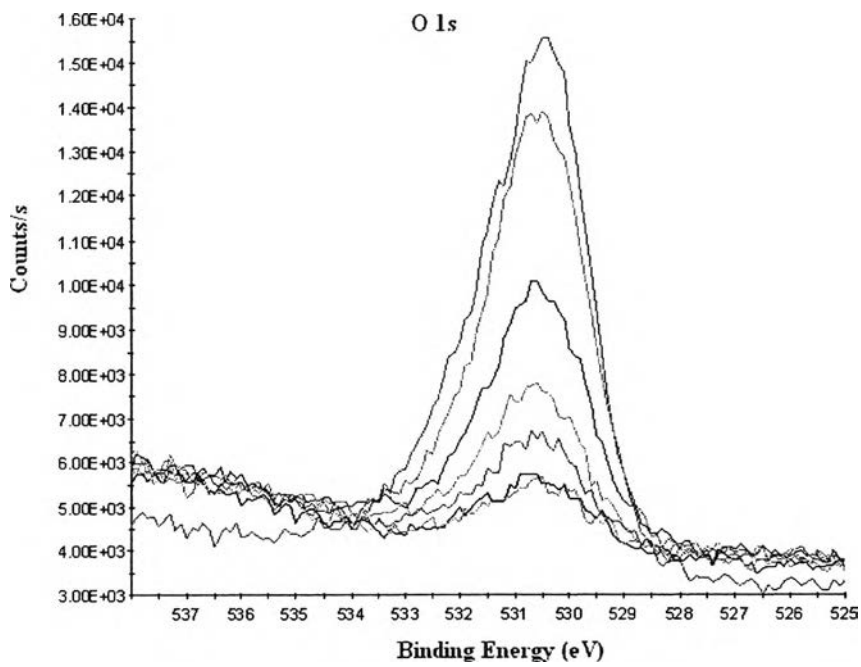

Figure 4.30 O 1s core level spectra of oxide film grown on SS304 as function of sputtering (Run 3).

As a conclusion, the results from XPS analysis indicate that the crystallite layer (as the outer oxide layer) on SS304 sample was enriched in Ni and Fe and possibly consisted of ZnO, $Ni(OH)_2$, FeO, Fe_2O_3, Cr_2O_3, TiO_2 and $Ni_{0.87}Fe_{2.13}O_4$. The underlying layer (as the inner oxide layer) was enriched in Cr, possibly as $FeCr_2O_4$. These observations are consistent with the results from EDX analysis. The thickness of the oxide film was approximately 0.15 μm, which was somewhat thicker than the oxide film on Alloy 600 MA in Run 1 (~0.1 μm), possibly because SS304 has a lower corrosion resistance than Alloy 600 MA and was exposed to higher coolant temperature since the SG samples were cooled.

4.2 Corrosion Test in the Ti-2 Autoclave without Heat Transfer

4.2.1 Run 4

Alloy 600 MA and TT, Alloy 690 MA, CD and TT, Alloy 800 MA and SP, SS304 and Zirc-4 were exposed to coolant at 300°C for 30 days. All samples were darkened during exposure; examples are shown in Figure 4.31.

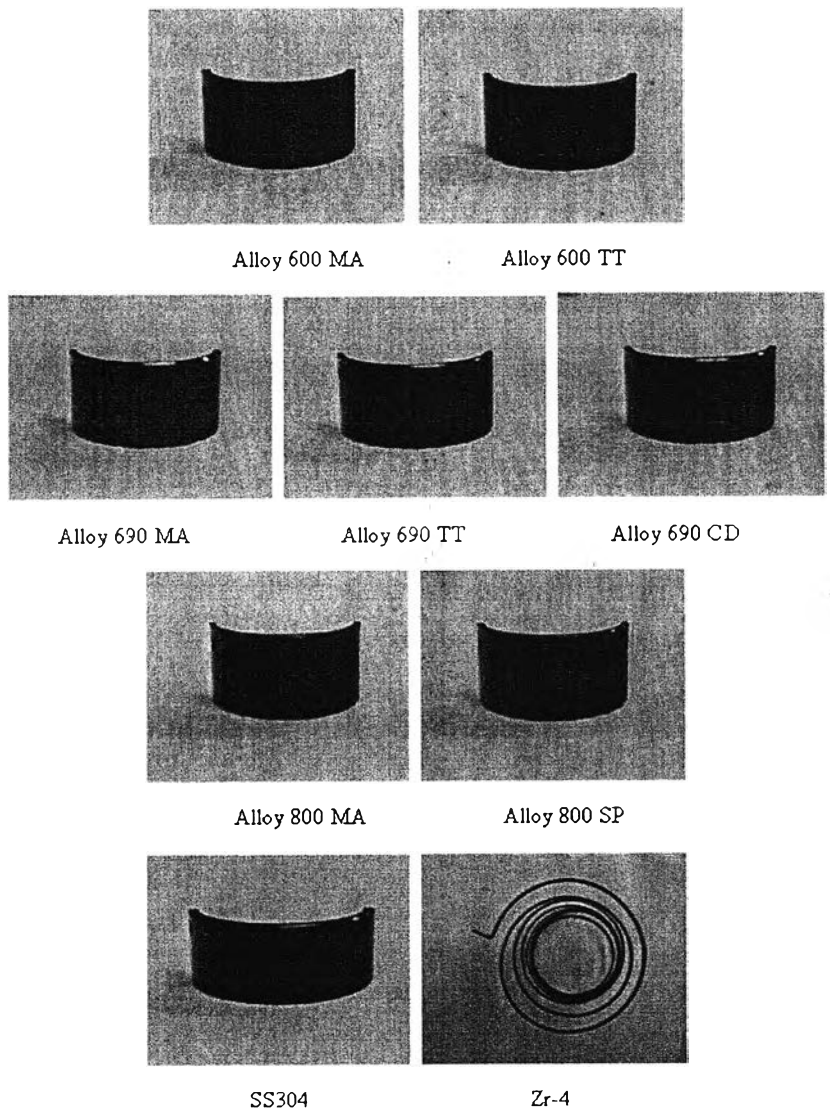

Figure 4.31 Samples after exposure in Run 4.

From Figure 4.31, for the same materials, the colors after exposure were different with different heat treatments; (i) for Alloy 600, TT provided the color darker than MA, (ii) for Alloy 690, TT had the darkest color followed by CD and MA and (iii) for Alloy 800, SP was darker than MA. For MA and TT, Alloy 800 had the darkest color followed by Alloy 600 and Alloy 690. Table 4.22 shows the weight changes of samples. Some SG samples and SS304 samples during exposure gained weight, while some of them lost weight. Weight changes were possibly affected by removing the samples from the stainless steel wires on the sample tree. Zircaloy-4 gained weight much more than the other samples even considering its much greater weight before exposure.

Table 4.22 Weight of the samples before and after exposure in Run 4

Sample	Surface Area (cm^2)	Before (g)	After (g)	Weight Change (mg)	Weight Change per Unit Area (mg/dm^2)
Zircaloy-4	87.78	22.8466	22.9136	+67	+76.33
SS304-1	9.02	4.3085	4.3091	+0.6	+6.65
SS304-2	9.02	4.2258	4.2256	-0.2	-2.22
SS304-3	9.02	4.3586	4.3588	+0.2	+2.22
SS304-4	9.02	4.3697	4.3704	+0.7	+7.76
SS304-5	9.02	4.3650	4.3642	-0.8	-8.87
SS304-6	9.02	4.3717	4.3713	-0.4	-4.43
SS304-7	9.02	4.4513	4.4511	-0.2	-2.22
SS304-8	9.02	4.3939	4.3941	+0.2	+2.22
Alloy 600MA (Westinghouse)	6.52	2.4906	2.4909	+0.3	+4.60
Alloy 600 TT (Westinghouse)	6.49	2.4806	2.4812	+0.6	+9.24
Alloy 690 MA (Valinox)	6.51	2.2762	2.2754	-0.8	-12.29

Table 4.22 Weight of the samples before and after exposure in Run 4 (cont.)

Sample	Surface Area (cm^2)	Before (g)	After (g)	Weight Change (mg)	Weight Change per Unit Area (mg/dm^2)
Alloy 690 TT (Sandvik)	6.49	2.3558	2.3558	0.0	0.00
Alloy 690 TT (Valinox)	6.49	2.2393	2.2390	-0.3	-4.62
Alloy 690 CD (Valinox)	6.50	2.3351	2.3353	+0.2	+3.08
Alloy 800 MA (Unknown)	6.40	1.7781	1.7779	-0.2	-3.12
Alloy 800 SP (Sandvik)	6.48	2.1255	2.1251	-0.4	-6.17

Table 4.23 shows coolant chemistry before and after exposure. Boron concentration after exposure was higher than that before exposure, but the difference is within the measurement error. The pH values before and after exposure are slightly different. The higher concentration of Ni, Fe and Mn in the coolant after exposure is because of the dissolution of these metal ions from the corrosion products and the base materials of SG and SS304 samples. However, in this run, the concentrations of these metal ions after exposure were lower than those in Run 3, even though the exposure time in Run 4 was longer than that in Run 3. This is possibly effected by the solubility of these metal ions. Since the corrosion products were mainly composed of nickel-ferrite ($Ni_xFe_{3-x}O_4$), the pH_T value for the minimum solubility is 7.4 (Song and Lee, 1999). Therefore, the corrosion products in Run 4 (pH_T 7.4) had lower solubility than those in Run 3 (pH_T 7.01), resulting in the lower concentrations of metal ions in the coolant. As mentioned earlier in Run 1 and Run 3, the higher Zn concentration after exposure possibly resulted from the residual Zn contamination

from the lubricant used in this work (ZnO is one of its constituents) and/or from the previous work (the autoclave was operated with water containing Zn).

Table 4.23 Coolant chemistry before and after exposure in Run 4

Conditions	Before	After
Boron concentration (ppm)	1990	2089
pH @ room temperature	6.67	6.72
$pH_{300°C}$	7.4	7.37
Fe concentration (ppb)	-	very low**
Ni concentration (ppb)	-	1.5±0.93
Mn concentration (ppb)	-	9.3±3.1
Zn concentration (ppb)	0.4*	5.9±1.1

*from the de-ionized water

**below the detection limit

In this run, all SG samples, SS304-1, SS304-5 and a small part of the Zr-coil were analysed with EDX and SEM for studying the effect of SG alloy heat treatment and composition on oxide formation. The results are presented and discussed as follows:

4.2.1.1 EDX and SEM Analyses

SEM was performed on the convex surfaces of SG and SS304 samples and on the surface of the Zirc-4 piece. Figure 4.32 shows the oxide morphologies on Alloy 600 MA and TT. They were both covered with mostly platelet crystals overlaying a needle-like oxide layer, but their crystallite size and coverage were different. The platelets on Alloy 600 MA were bigger, but their coverage was lower, than those formed on Alloy 600 TT. Also, the crystallite coverage on Alloy 600 TT was more uniform than that on Alloy 600 MA. These results are possibly caused by the fact that mill annealing (MA) processed at ~1000°C for few minutes results in carbide precipitation within the grain boundaries, causing the Cr depletion around the grain boundaries. Thermal treatment (TT)

processed at 700-720°C for 10-15 hours after mill annealing (MA) dissolves carbides into solid solution and then precipitates some within the grains, as illustrated in Figure 4.33. However, Cr depletion at the grain boundaries is reduced, and carbide-precipitate distribution throughout the grain is made uniform. Therefore, it is hypothesized that Alloy 600 TT could be corroded uniformly across the grains, while Alloy 600 MA may have been more corroded at the grain boundaries. For about the same amount of corrosion, lower crystallite coverage resulted in larger crystallites, as observed on Alloy 600MA. Alloy 600 TT was darker than Alloy 600 MA, possibly because of its higher crystallite coverage.

Alloy 600 MA and TT were analysed with EDX on their convex surfaces at 0° (as explained in Figure 3.8) and the results are shown in Table 4.24 and Table 4.25. It should be noted that the elemental compositions before exposure refer to the elemental compositions of base metal. The elemental compositions before and after exposure are different, indicating the presence of oxide layers, but Alloy 600 MA and TT had the same trend. The weight percentage of Ni tended to decrease while the weight percentage of Fe increased in the platelets. They are possibly nickel ferrite, i.e., trevorite ($NiFe_2O_4$), because the Raman spectra of platelet crystals, as shown in Figure C.1 in Appendix C, were observed at the same positions of the main spectra of the nickel ferrite, as shown in Figure C.2-C.4 in Appendix C. The underlying layer had the highest Cr content compared with the platelets and the base metal – possibly a Ni-Fe chromite. Titanium, Cu and Zr were observed in the oxides on both materials. Titanium and Zr come from the test section and heater cladding material, while Cu possibly comes from the SG alloys and/or the lubricant.

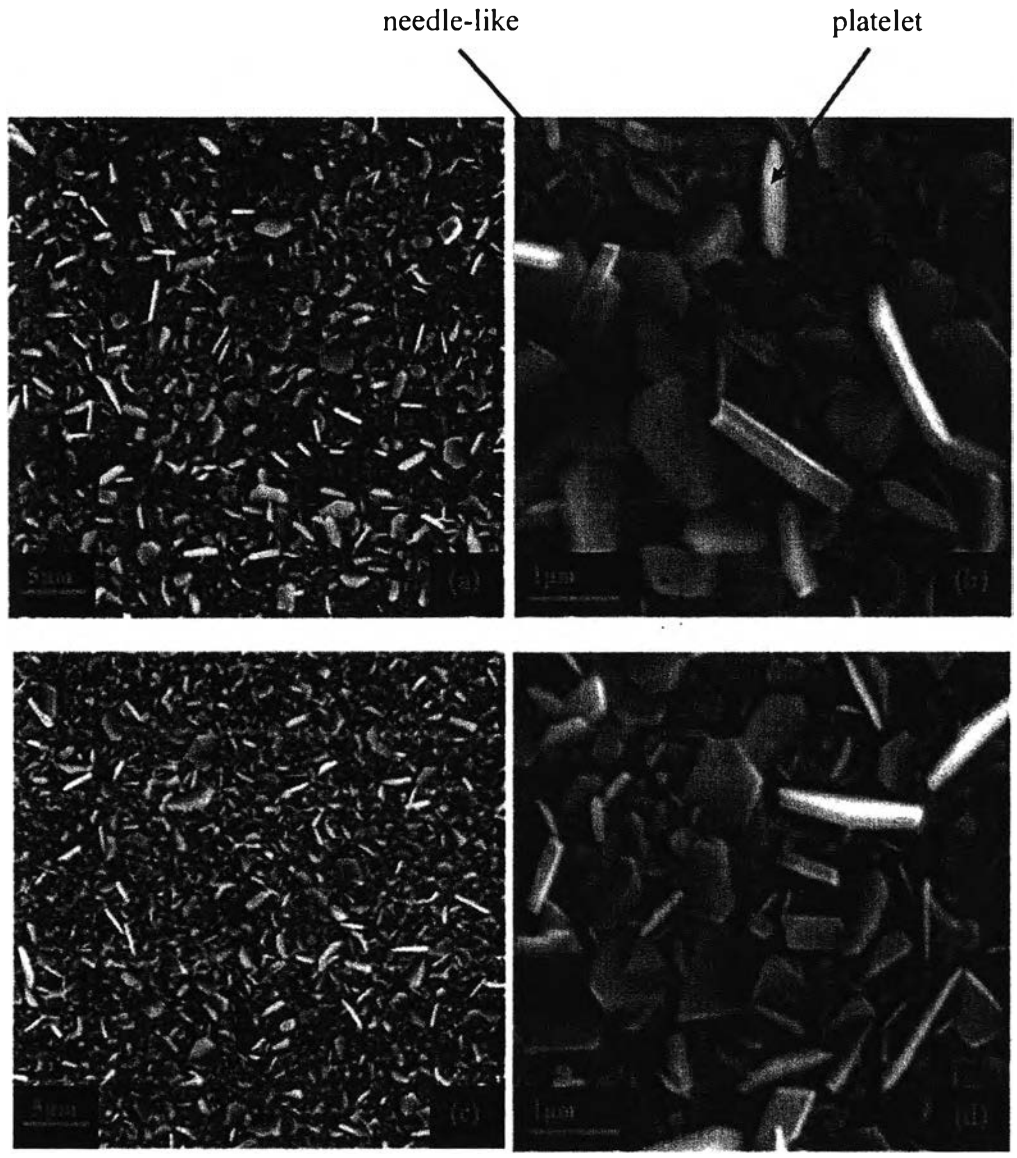

Figure 4.32 SEM images of Alloy 600 MA (a and b) and Alloy 600 TT (c and d).

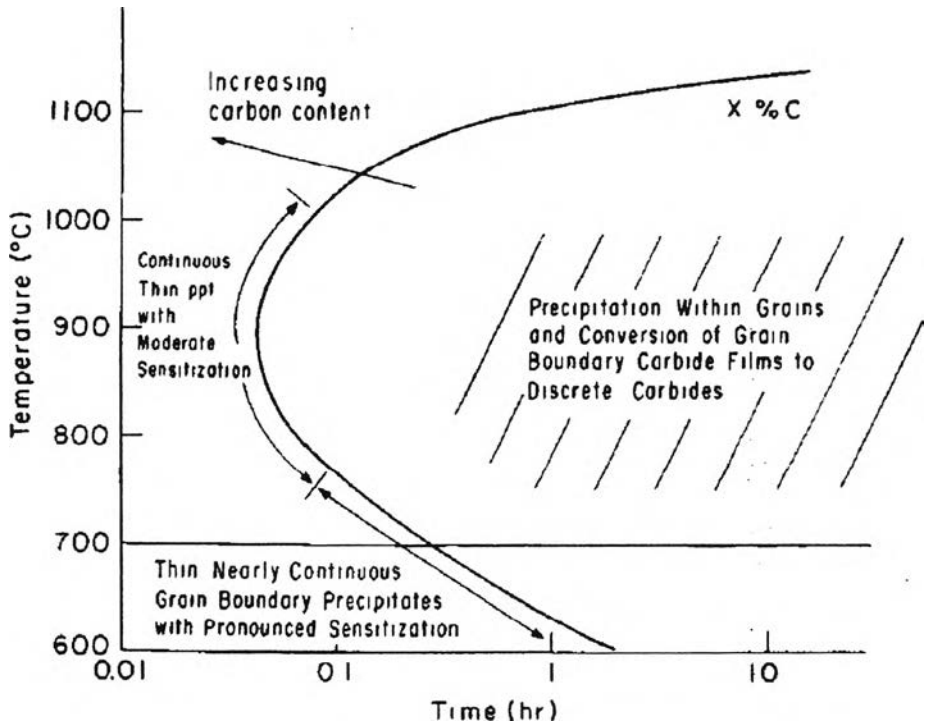

Figure 4.33 Schematic of a carbide precipitation (a time-temperature-transformation, TTT) diagram for Inconel 600 (Scarberry *et al.*, 1976).

Table 4.24 EDX result from the convex surface of Alloy 600 MA in Run 4

Position	Wt%						
	Ni	Fe	Cr	Ti	Cu	Zr	O
Platelet	34.66	24.04	7	4.86	0.61	0.1	28.73
Needle-like layer	64.19	12.4	15.69	1.2	1.04	0.07	5.41
Before exposure	70.83	9.63	15.40	0.39	*	-	2

*was not recorded

Table 4.25 EDX result from the convex surface of Alloy 600 TT in Run 4

Position	Wt%						
	Ni	Fe	Cr	Ti	Cu	Zr	O
Platelet	41.77	22.02	9.42	3.43	0.61	0.19	22.56
Needle-like layer	64.53	13.16	15.81	1.16	0.88	0.07	4.39
Before exposure	71.56	9.41	15.09	0.29	*	-	2.54

*was not recorded

It is interesting to note that Alloy 600 TT in Run 3, which was exposed to coolant for 10 days, formed a single oxide layer, while Alloy 600 TT in Run 4, which was exposed to coolant for 30 days, formed a double oxide layer, as shown in Figure 4.34. The different morphologies were presumably the results of exposure time and slightly different chemistries ($pH_{300°C}$ in Run 3 was 7.01 and in Run 4 was 7.4).

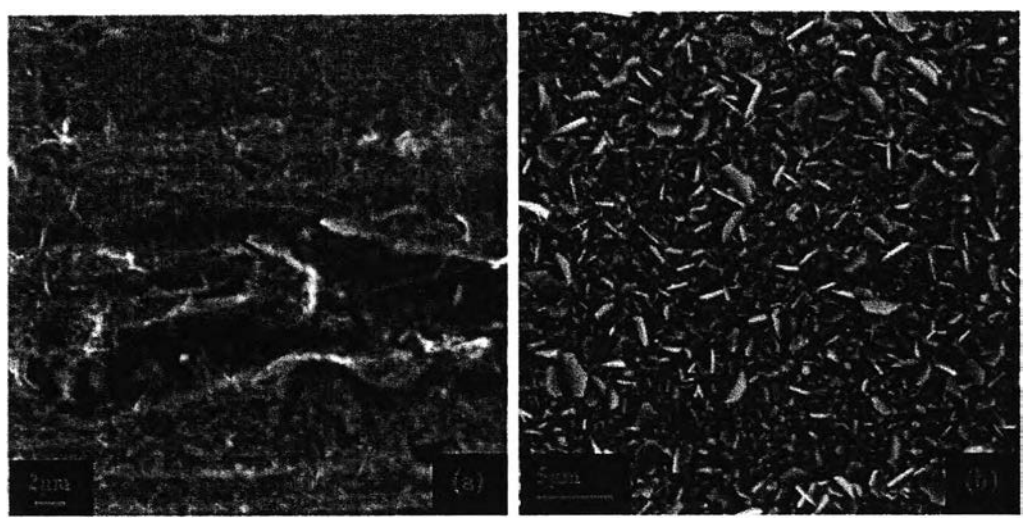

Figure 4.34 Comparison of SEM images of Alloy 600 TT in Run 3 (a) with Alloy 600 TT in Run 4 (b).

Oxide morphologies on Alloy 690 MA, TT and CD are shown in Figure 4.35-4.37, respectively. They were covered with polyhedral crystallites having high surface coverage; an underlying layer cannot be seen. Morphologies were different according to the different heat treatments. Alloy 690 CD was covered with the largest crystallites followed by Alloy 690 MA and TT. The morphologies on Alloy 690 TT from Sandvik and Valinox were slightly different, possibly because they were processed with slightly different temperatures and times; for example, Alloy 690 is processed at 720°C for Sandvik and at 716°C for Valinox. However, both of them were covered with a compact layer of tiny crystallites with larger crystallites.

Figure 4.37 shows that Alloy 690 CD was covered with crystallites having two sizes. The smaller crystallites were observed all over the general surface, possibly because such areas had high defect structures due to cold work, resulting in high oxide nucleation; the bigger crystallites were observed in cavities, probably resulting from higher concentration of solution species in the cavities. From a comparison of SEM images of Alloy 690 MA, TT and CD from Valinox as shown in Figure 4.38, on the general surface TT had the smallest average crystallite size, while the crystallites on MA were smaller than those on CD. Thermal treating (TT) had the highest crystallite coverage followed by MA and then CD. Therefore, the oxide formed on Alloy 690 TT was likely more compact than that on Alloy 690 MA and Alloy 690 CD. According to the colors of Alloy 690 MA, TT and CD, TT was darkest no doubt because of the highest crystallite coverage, but MA was brighter than CD, even though its crystallite coverage was higher than that of CD (possibly because of a more porous crystallite layer).

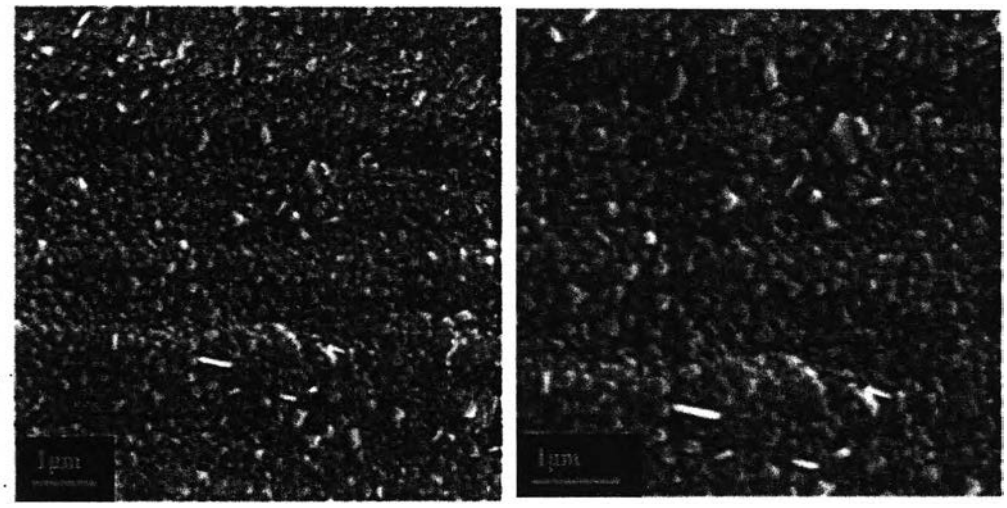

Figure 4.35 SEM images of Alloy 690 MA in Run 4.

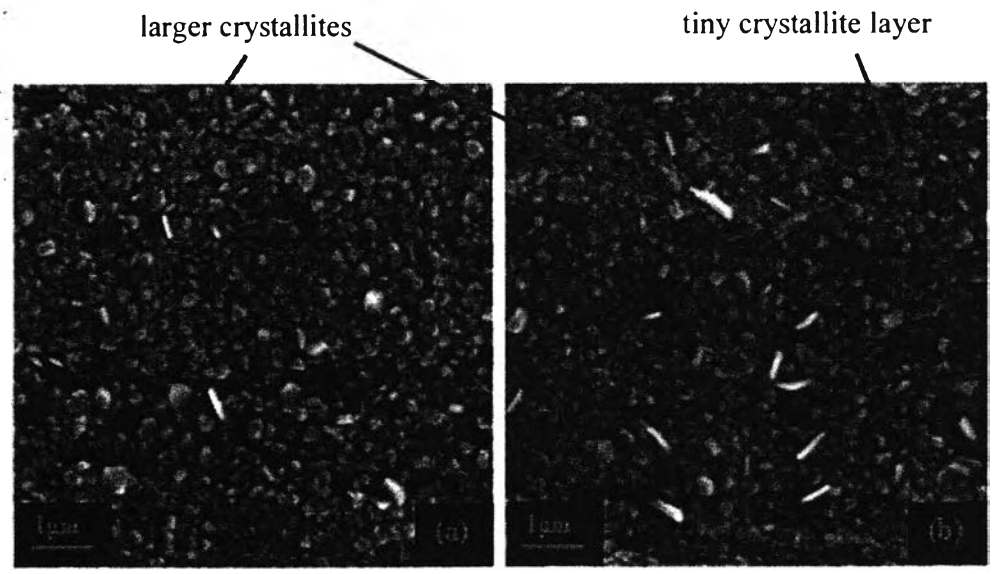

Figure 4.36 SEM images of Alloy 690 TT from Sandvik (a) and Valinox (b) in Run 4.

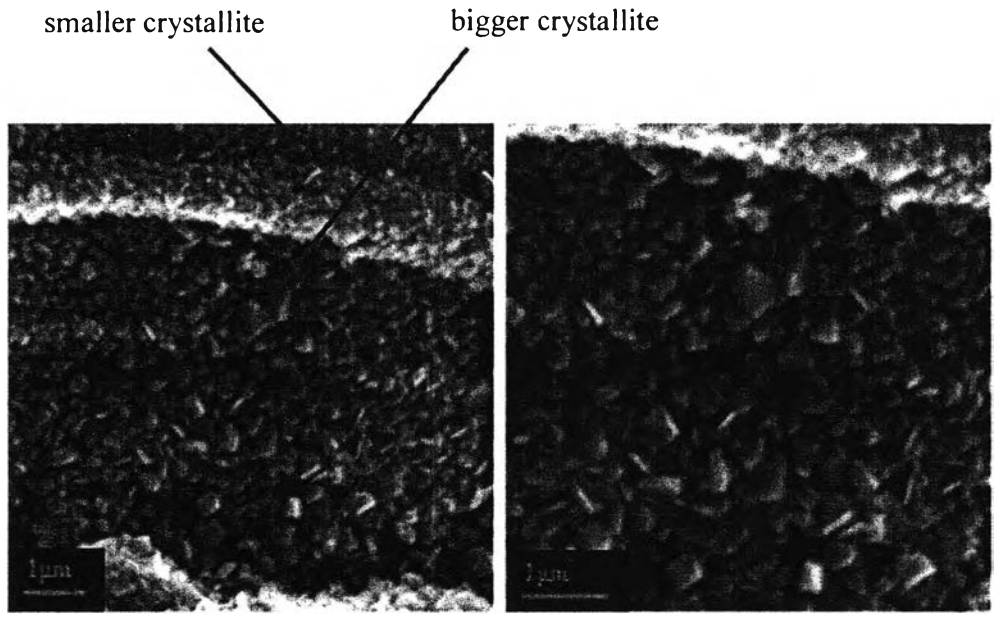

Figure 4.37 SEM images of Alloy 690 CD in Run 4.

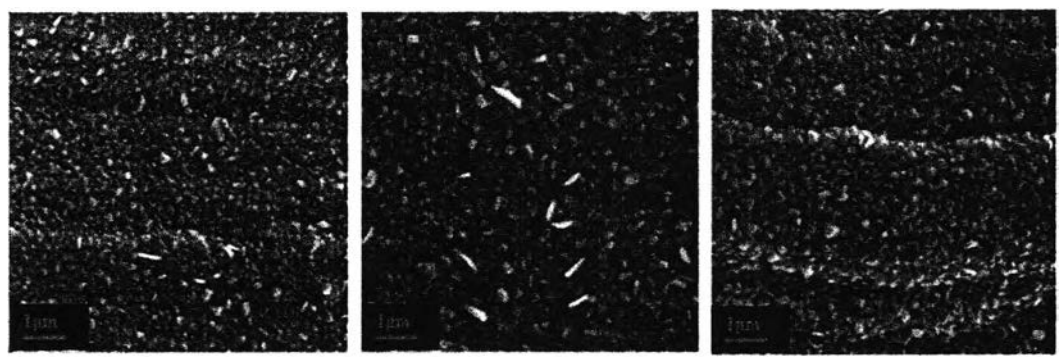

Figure 4.38 SEM images of Alloy 690 MA, TT and CD in Run 4.

Next, EDX analysis was performed on Alloy 690 MA, TT and CD and the results are shown in Table 4.26-4.28. It should be noted that the elemental compositions of the underlying layer were determined by analysing on the surface between crystallites. On all three materials, the weight percentage of Fe tended to increase toward the crystallite layer, while the weight percentage of Cr was the highest in the underlying layer. This indicates that the crystallite layer was Fe-

rich and the underlying layer was Cr-rich, which is consistent with the results reported by Sennour *et al.* (2008).

Table 4.26 EDX result from the convex surface of Alloy 690 MA from Valinox in Run 4

Position	Wt%						
	Ni	**Fe**	**Cr**	**Ti**	**Cu**	**Zr**	**O**
Crystallite layer	12.57	49.44	7.41	1.64	0.34	0.17	28.43
Underlying layer	53.49	12.01	28.99	1.26	0.85	0.1	3.3
Before exposure	56.37	9.47	27.41	0.33	*	-	6.42

*was not recorded

Table 4.27 EDX result from the convex surface of Alloy 690 TT from Valinox in Run 4

Position	Wt%						
	Ni	**Fe**	**Cr**	**Ti**	**Cu**	**Zr**	**O**
Crystallite layer	38	16.51	28.07	2.21	0.72	0.16	14.33
Underlying layer	50.06	11.79	32.48	1.37	1.04	0.1	3.16
Before exposure	57.55	9.80	27.37	0.30	*	-	4.98

*was not recorded

Table 4.28 EDX result from the convex surface of Alloy 690 CD from Valinox in Run 4

Position	Wt%						
	Ni	Fe	Cr	Ti	Cu	Zr	O
Crystallite layer	35.87	18.71	23.66	2.79	0.96	0.1	17.91
Underlying layer	52.86	12.94	27.52	1.09	0.6	0.11	4.88
Before exposure	57.37	10.03	27.23	0.44	*	-	4.93

*was not recorded

Scanning electron micrographs from exposed Alloy 800 MA and SP are shown in Figure 4.39. They were both covered with crystallites overlaying an apparently amorphous layer, but they had different crystallite sizes and coverages. Since shot peening strengthens the surface by creating defects that resulted in a high oxide nucleation rate, the crystallites on Alloy 800 SP were smaller than those on Alloy 800 MA, but their coverage was higher. The higher crystallite coverage led to the darker color as mentioned earlier.

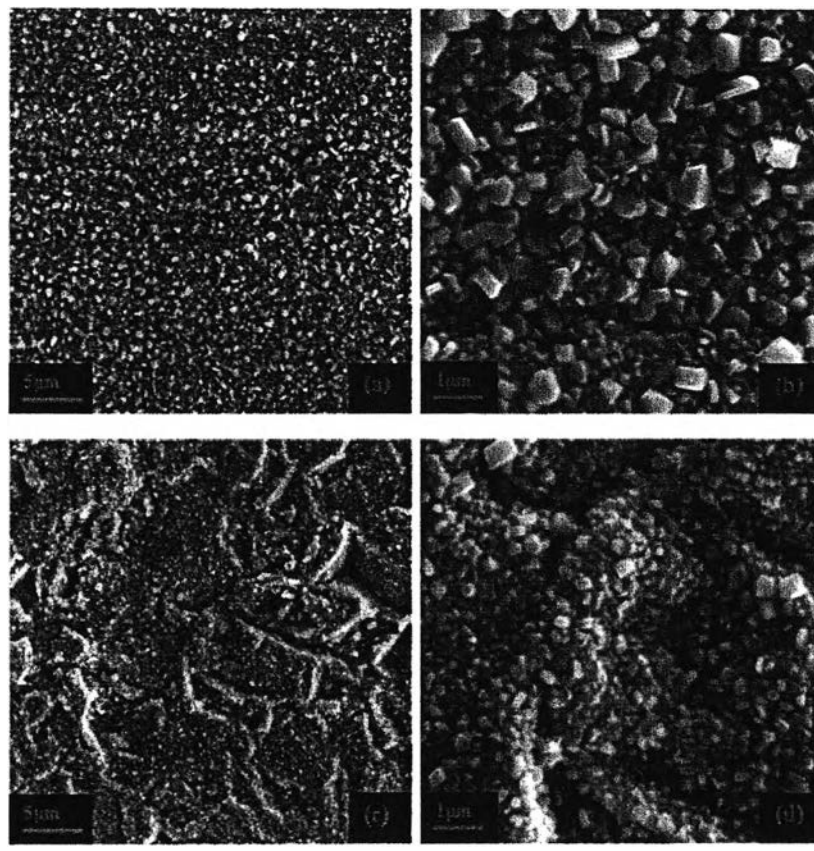

Figure 4.39 SEM images of Alloy 800 MA (a and b) and Alloy 800 SP (c and d) in Run 4.

The EDX results in Table 4.29 and Table 4.30 show that the weight percentage of Ni decreased toward the crystallite layer, probably due to the release of Ni to the coolant (however, the Fe content of the crystallites was lower, but the Fe/Cr ratio was higher, than in the underlying layer). These indicate that the crystallites on Alloy 800 MA and SP were Fe-rich and the underlying layers were Cr-rich, as observed on Alloy 600 and Alloy 690. However, the crystallite shape on Alloy 600 (mostly platelet) was different from that on Alloy 690 and Alloy 800 (mostly octahedral), but they were probably nickel ferrite, $(Ni_xFe_{1-x})Fe_2O_4$ (confirmed by LRS spectra, as shown in Figure C.1 in Appendix C, compared with the Raman spectra of nickel ferrite in Figure C.2-C.4 in Appendix C). This difference may have been due to the different ratio of Ni to Fe in the nickel ferrite, as shown in Table 4.31, probably affected by the nature of the base metal and the saturation of the

coolant in Ni and Fe cations, resulting in the spectral shift. From the EDX results in Table 4.31, in general the Fe/Ni ratio of nickel ferrite is not less than 2, but it was observed on Alloy 600, possibly because of interference from the base metal. The Fe/Ni ratios in crystallites on Alloy 690 and Alloy 800 suggested that crystallites might be $Ni_{0.6}Fe_{2.4}O_4$ on Alloy 690 and $NiFe_2O_4$ on Alloy 800.

Table 4.29 EDX result from the convex surface of Alloy 800 MA in Run 4

Position	Wt%						
	Ni	Fe	Cr	Ti	Cu	Zr	O
Crystallite layer	21.54	39.4	8.78	1.95	0.59	0.16	27.58
Underlying layer	31.55	41.7	21.87	1.12	1.14	0.14	2.48
Before exposure	31.94	43.04	19.29	0.35	*	-	5.38

*was not recorded

Table 4.30 EDX result from the convex surface of Alloy 800 SP in Run 4

Position	Wt%						
	Ni	Fe	Cr	Ti	Cu	Zr	O
Crystallite layer	22.25	39.81	13.07	1.87	0.44	0.12	22.44
Underlying layer	29.34	40.88	23.9	1.59	0.68	0.14	3.47
Before exposure	31.59	41.96	20.96	0.54	*	-	4.95

*was not recorded

Table 4.31 Ni and Fe ratio in crystallite on Alloy 600, Alloy 690 and Alloy 800 in Run 4

SG alloy	At%		
	Ni	Fe	Fe/Ni
Alloy 600	46.48	33.88	0.73
Alloy 690	16.64	68.79	~4
Alloy 800	28.31	54.45	~2

Figure 4.40 compares the oxides on Alloy 600, Alloy 690 and Alloy 800 processed by mill annealing (MA). Alloy 600 MA had the biggest crystallites followed by Alloy 800 MA and then Alloy 690 MA, while the crystallite coverage of Alloy 690 MA was higher than that of Alloy 800 MA, which was higher than that of Alloy 600 MA. Clearly, the SG alloy composition had a large effect on the oxide morphology. The compactness of the oxide formed on Alloy 690 MA suggests that it may have been more protective than that on Alloy 800 MA and on Alloy 600 MA. It is most likely effected by the Cr content in the alloys, since the weight percentage of Cr in Alloy 690 is the highest followed by Alloy 800 and then Alloy 600 as shown in Table 2.2. Chromium is a significant component of protective oxides, as shown in Table 2.4. Terachi *et al.* (2008) found that 20% Cr alloy produced finer oxide particles in the inner oxide layer and had a thinner oxide than 5% Cr alloy, and they indicated that increasing the Cr content in alloy can reduce the corrosion rate.

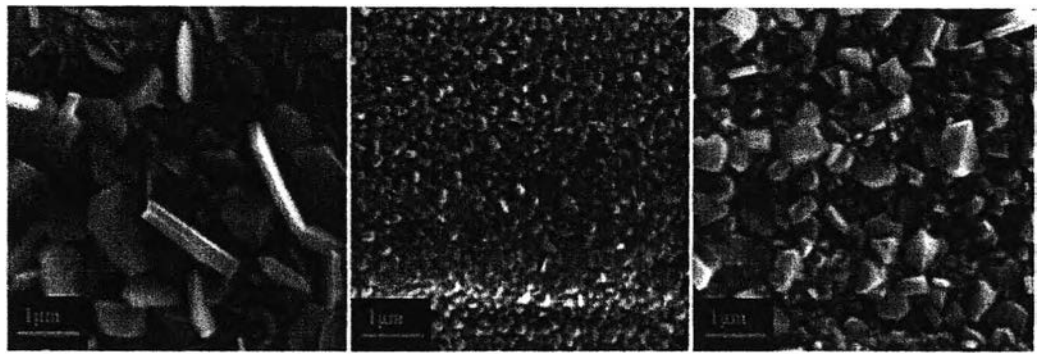

Alloy 600 MA Alloy 690 MA Alloy 800 MA

Figure 4.40 SEM images of Alloy 600 MA, Alloy 690 MA and Alloy 800 MA in Run 4.

From a comparison between oxide morphologies on Alloy 600 TT and Alloy 690 TT in Figure 4.41, it is seen that the crystallites on Alloy 600 TT were bigger, while the crystallite coverage was lower, than on Alloy 690 TT. This observation parallels that of Alloy 600 MA and Alloy 690 MA, indicating that the oxide formed on Alloy 690 TT was more protective than Alloy 600 TT – again, no doubt due to the Cr content of the alloy.

In summary, according to the EDX and SEM results of SG samples, all SG materials were covered with crystallites overlaying an apparently amorphous layer, which cannot be seen on Alloy 690 because of its compact oxide. The crystallites were Fe-rich and the underlying layer was Cr-rich, however, but the crystallite sizes and coverages depended on the heat treatment and the alloy composition. For the same heat treatment, the higher-Cr alloys apparently produced more protective oxide (finer and more compact crystallites) than the lower-Cr alloys. In addition, heat treatment effects were observed on all alloys, but were overshadowed by effects of alloy composition. The compactness of the oxide on Alloy 690 suggests that the crystallites would be resistant to spalling – particularly in comparison to Alloy 600 and even Alloy 800 – which would reduce material transport and therefore radiation field build-up in reactor primary coolants.

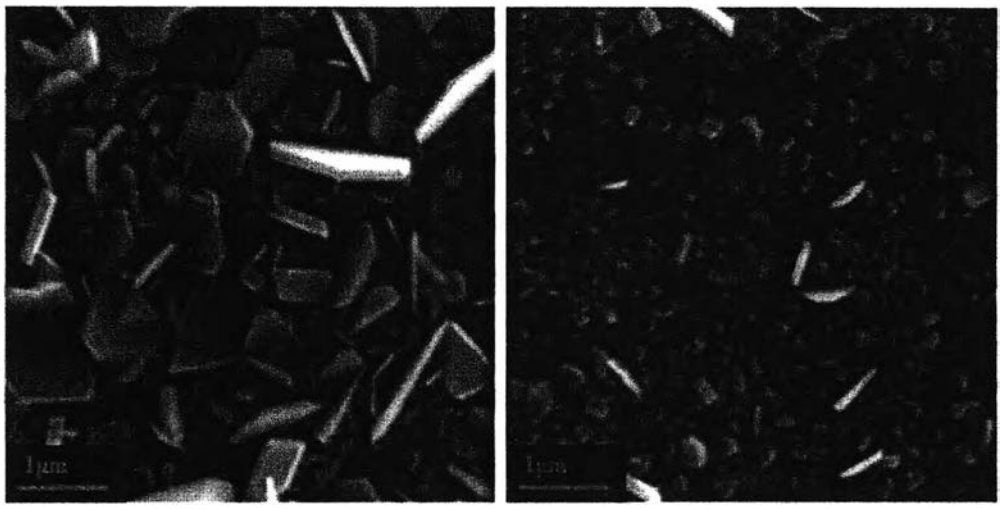

Alloy 600 TT Alloy 690 TT

Figure 4.41 Comparison of the surface morphologies of Alloy 600 TT with Alloy 690 TT in Run 4.

Besides the SEM and EDX analyses on the convex surface of Alloy 600 MA, Alloy 600 MA was sectioned at the circumferential line and was analysed with SEM and EDX on the cross-sectional surface. The SEM cross-section image is shown in Figure 4.42. It shows that the oxide film was very thin (as can be seen at the outside of the bright zone), even though the sample was exposed to the coolant for longer time compared with the Alloy 600 MA in Run 1. This is possibly because some oxides were damaged during the epoxy resin molding. However, this suggests that the oxide thickness cannot be estimated by this technique. EDX was performed on the cross-sectional surface at three locations along the radial line, as illustrated in Figure 3.9. The results, as shown in Table 4.32, show that the Ni and Fe contents tended to decrease, while the Cr content tended to increase toward the M/MO interface (A is at the M/MO interface), possibly because of the formation of Cr-rich oxide closed to the M/MO interface. The amount of Ti, Zr and Cu was significant near the M/MO interface due to the incorporation of Ti, Zr and Cu from the coolant. However, again, the oxide film was too thin to be analysed accurately with EDX.

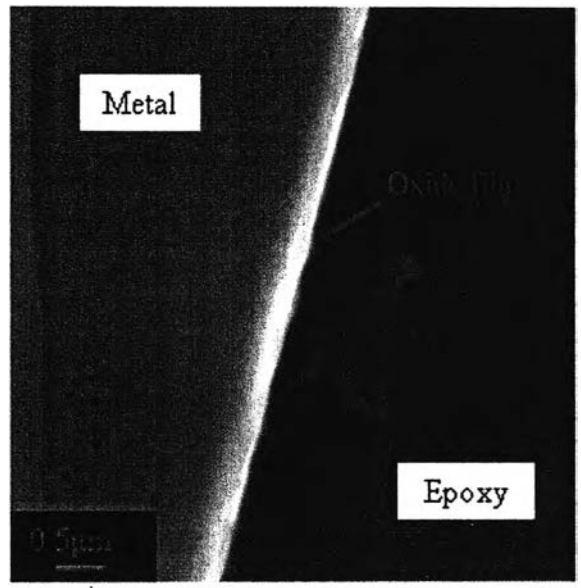

Figure 4.42 SEM cross-section image of oxide film grown on Alloy 600 MA in Run 4.

Table 4.32 EDX result on the cross-sectional surface along radial lines of Alloy 600 MA in Run 4

Location	Wt%					
	Ni	Fe	Cr	Ti	Cu	Zr
A	66.7	9.08	16.79	0.37	1.7	0.12
B	68.23	9.74	16.24	0.63	1.4	0.24
C	69.61	9.71	16.12	0.33	1.25	0.11

In this run, eight samples of SS304 were exposed to the coolant. The representative samples SS304-1 (weight gain) and SS304-5 (weight loss) had oxide morphologies as shown in Figure 4.43. They had similar oxides, even though their weight changes were different, viz. a layer of large crystallites on top of much smaller crystallites. However, some grooves or fissures were observed on SS304-5 as can be seen in Figure 4.43, but not on SS304-1.

Table 4.33 and Table 4.34 show the EDX results on SS304-1 and SS304-5. The weight percentage of Fe in the crystallites was lower, but its Fe/Cr ratio was higher, than in the underlying layer. These indicate that the crystallite layer was Fe-rich and the underlying layer was Cr-rich.

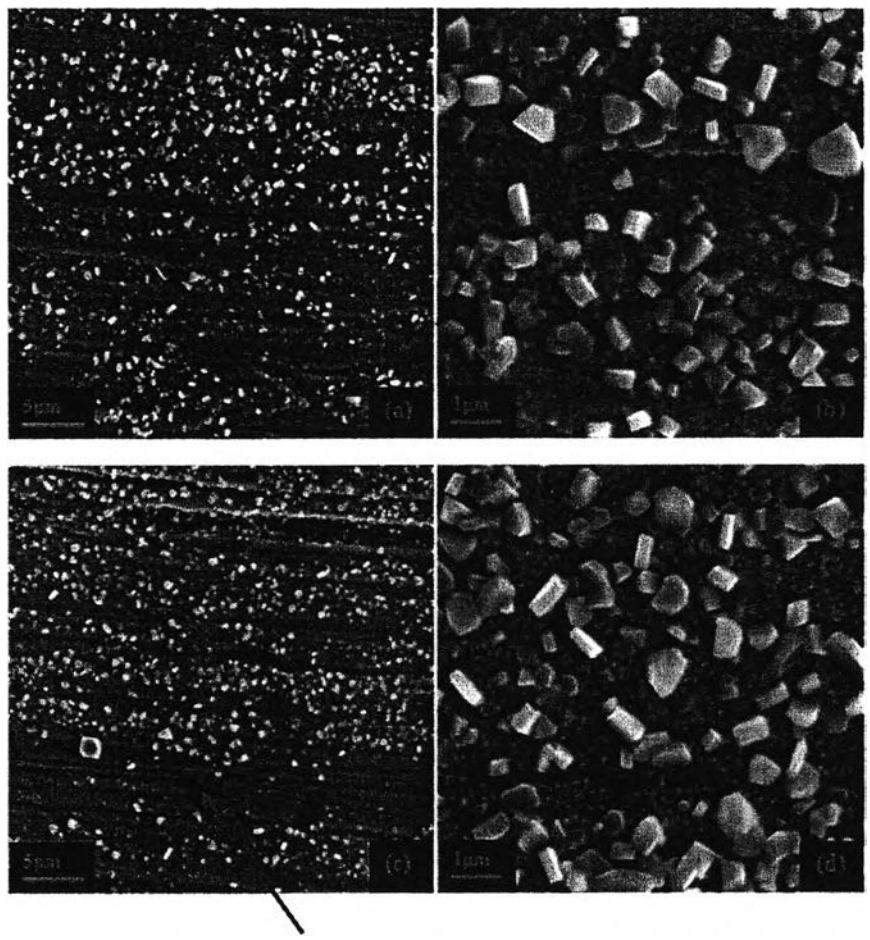

Figure 4.43 SEM images of SS304-1 (a and b) and SS304-5 (c and d) in Run 4.

Table 4.33 EDX result from the convex surface of SS304-1 in Run 4

Position	Wt%					
	Ni	Fe	Cr	Ti	O	Fe/Cr
Crystallite layer	9.92	57.84	17.63	0.56	12.53	3.28
Underlying layer	10.33	60.91	19.99	0.59	6.59	3.08

Table 4.34 EDX result from the convex surface of SS304-5 in Run 4

Position	Wt%					
	Ni	Fe	Cr	Ti	O	Fe/Cr
Crystallite layer	5.66	29.48	7.21	18.92	38.15	4.09
Underlying layer	9.95	64.51	19.64	0.17	4	3.28

A comparison with SS304 in Run 3, which was exposed to coolant with a lower $pH_{300°C}$ than that in Run 4 and for only 10 days, showed that the small crystallites on SS304 in Run 3 were slightly bigger (difficult to see from the micrographs) and had higher coverage, while the large crystallites on SS304 in Run 3 were smaller and had lower coverage, as shown in Figure 4.44. This observation is consistent with the effect of exposure time, as reported by Ziemniak and Hanson (2002), and obeys the theory of Ostwald ripening; the smallest particles (with the highest surface energy) tend to dissolve to benefit the largest particles with increasing time. However, it is also possibly due to the slightly different coolant pH.

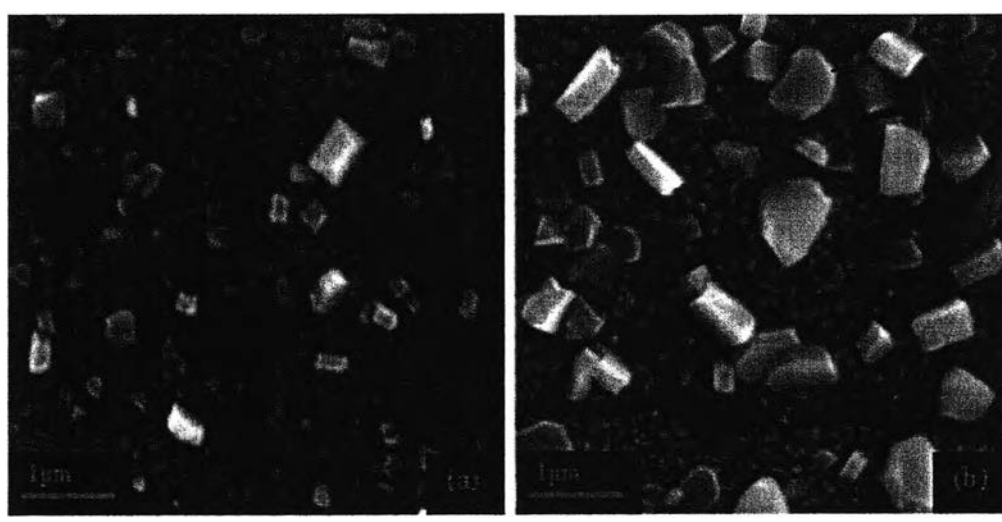

Figure 4.44 Comparison of the surface morphologies of SS304 in Run 3 (a) with SS304 in Run 4 (b).

On the Zirc-4 sample, amorphous oxides were observed on the general surface, while platelets and elongated oxides were observed in cavities, as shown in Figure 4.45. Furthermore, oxide crystals were sparsely scattered over the surface. From the EDX result in Table 4.35, Zr was the major constituent of the amorphous, platelet and elongated oxides, indicating that they should be ZrO_2. Titanium and Fe were the major constituents of the crystals, indicating that they were probably ilmenite ($FeTiO_3$).

A comparison with the oxide formed on Zirc-4 in Run 3 (as shown in Figure 4.46) indicates that most of the oxide in Run 3 was observed in scratches or cavities but in Run 4 it was distributed over the surface. This difference was probably due to the exposure time, and since at the start of exposure material was mainly corroded at scratches and cavities (because these areas are preferential sites for oxidation), most of the oxide was found in those areas as observed on Zirc-4 in Run 3. With increasing time, other areas started to corrode, resulting in more oxide distributed over the surface, as observed on Zirc-4 in Run 4. However, Table 4.36 shows the corrosion rate of Zirc-4 in Run 3 and Run 4. Zircaloy-4 in Run 3 had a higher corrosion rate, than in Run 4, possibly because the corrosion rate is relatively high at start of exposure and there was heat flux through the Zirc-4 surface in Run 3.

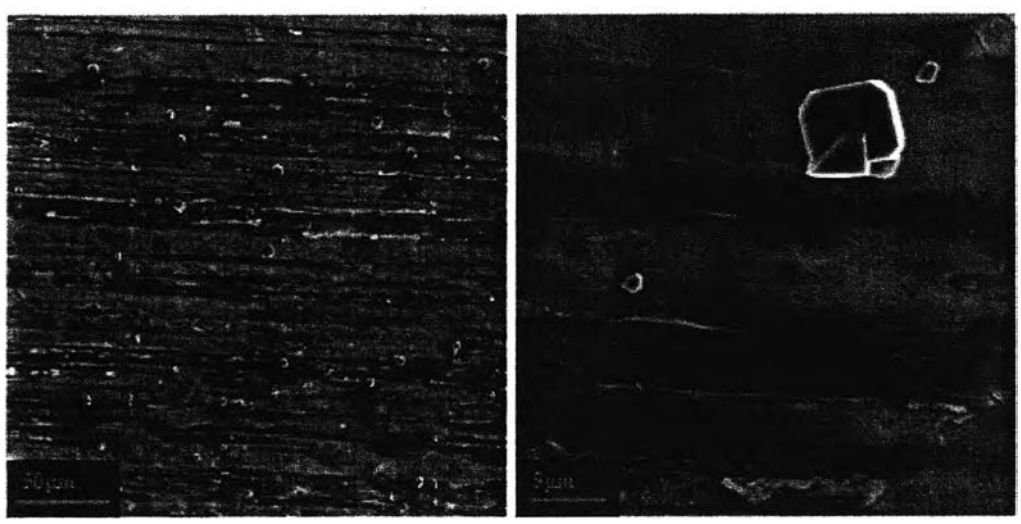

Figure 4.45 SEM images of Zirc-4 in Run 4.

Table 4.35 EDX result from the surface of Zirc-4 in Run 4

Position	Wt%					
	Ni	Fe	Cu	Zr	Ti	O
Amorphous oxide	0.55	0.82	0.72	77.73	0.59	19.59
Platelet/Elongated oxide	0.5	1.14	0.57	70.66	0.77	26.36
Crystal oxide	0.78	29.72	0.3	2.37	27.63	39.2

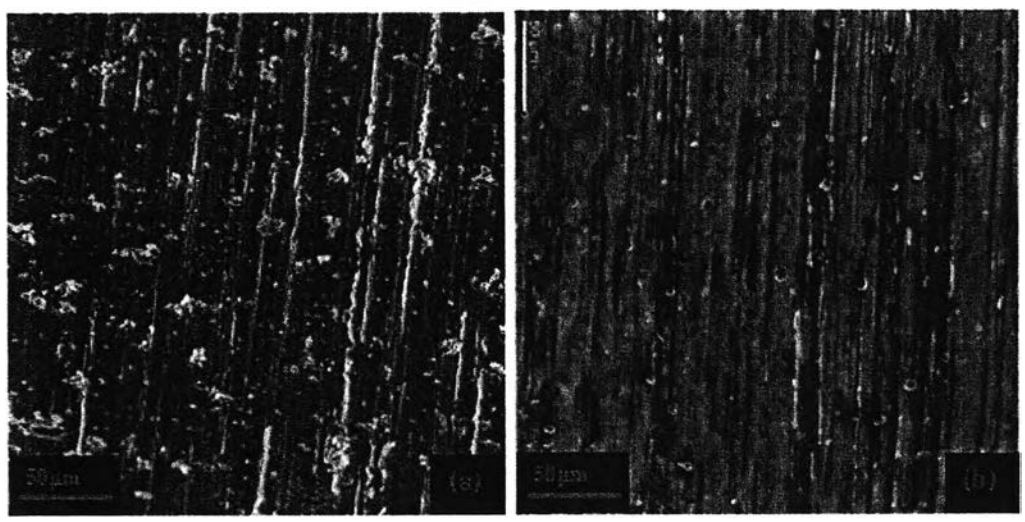

Figure 4.46 Comparison of the surface morphologies of Zirc-4 in Run 3 (a) with Zirc-4 in Run 4 (b).

Table 4.36 Comparison of Zirc-4 corrosion rate between Run 3 and Run 4

Zirc-4 sample	Surface Area (dm^2)	Weight Change (mg)	Exposure Time (days)	Corrosion rate (mdd)
Run 3	0.0417	+2.1	10	5.04
Run 4	0.8778	+67	30	2.54

4.2.2 Run 5

Samples in this run were the same as those in Run 4, but they were exposed to the coolant containing 20 ppb Zn (boron and lithium concentrations were similar to those in Run 4) for 30 days. The samples were darkened during exposure as shown in Figure 4.47 and their colors were different with different heat treatments and materials and corresponded with those in Run 4. However, the colors in this run were darker than those in Run 4.

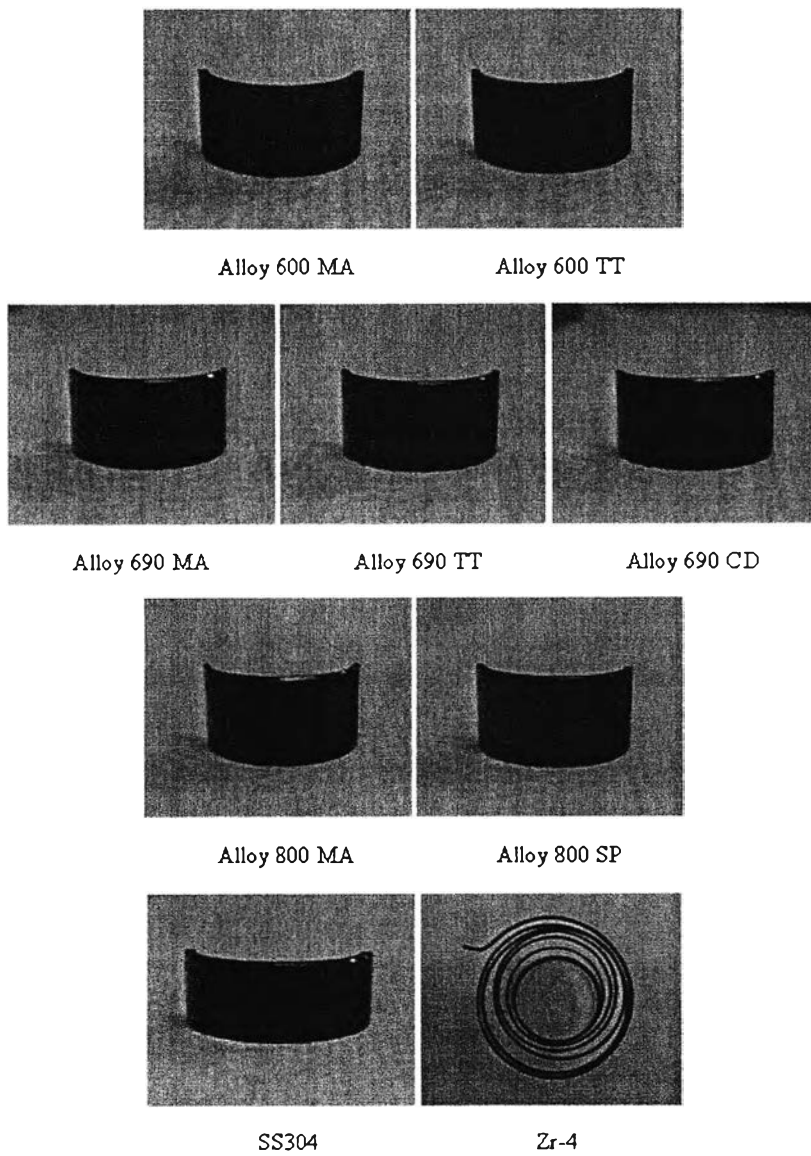

Figure 4.47 Samples after exposure in Run 5.

Table 4.37 shows the weight changes of samples after exposure. Most of SS304 samples lost weight, except SS304-5 and SS304-8 (weight gain), while all SG samples and Zirc-4 sample gained weight. The weight loss is possibly due to the dissolution of metal ions from the materials during exposure and the removing of samples from the stainless steel wires on the sample tree.

Table 4.37 Weight of the samples before and after exposure in Run 5

Sample	Surface Area (cm^2)	Before (g)	After (g)	Weight Change (mg)	Weight change per unit area (mg/dm^2)
Zircaloy-4	87.28	22.8554	22.8692	+13.8	+15.81
SS304-1	9.02	4.3516	4.3511	-0.5	-5.54
SS304-2	9.02	4.3941	4.3939	-0.2	-2.22
SS304-3	9.02	4.3396	4.3395	-0.1	-1.11
SS304-4	9.02	4.4873	4.4871	-0.2	-2.22
SS304-5	9.02	4.4007	4.4010	+0.3	+3.32
SS304-6	9.02	4.5117	4.5115	-0.2	-2.22
SS304-7	9.02	4.4024	4.4022	-0.2	-2.22
SS304-8	9.02	4.2791	4.2792	+0.1	+1.11
Alloy 600MA (Westinghouse)	6.52	2.4670	2.4671	+0.1	+1.53
Alloy 600 TT (Westinghouse)	6.49	2.4054	2.4060	+0.6	+9.24
Alloy 690 MA (Valinox)	6.51	2.2444	2.2448	+0.4	+6.14
Alloy 690 TT (Sandvik)	6.49	2.3916	2.3918	+0.2	+3.08
Alloy 690 TT (Valinox)	6.49	2.2749	2.2751	+0.2	+3.08
Alloy 690 CD (Valinox)	6.50	2.3686	2.3688	+0.2	+3.08

Sample	Surface Area (cm^2)	Before (g)	After (g)	Weight Change (mg)	Weight change per unit area (mg/dm^2)
Alloy 800 MA (Manufacturer Unknown)	6.40	1.8792	1.8798	+0.6	+9.38
Alloy 800 SP (Sandvik)	6.48	2.1050	2.1061	+1.1	+16.98

The boron concentration, coolant pH and iron concentration were measured before and after exposure and are shown in Table 4.38. The boron concentration after exposure was much higher than that before exposure due to the leakage at the start of exposure; however, it is expected that the lithium concentration was also increased by the leak. The pH values before and after exposure were slightly different but the difference was within the measurement error. In this run, again, the higher concentration of Ni, Fe and Mn in the coolant after exposure resulted of the dissolution of these metal ions from the oxides and the base materials of SG and SS304 samples. In this run, since Zn stock solution was added in the coolant to obtain a Zn concentration of 20 ppb, the Zn concentration in Run 5 was relatively higher than those in Runs 1, 3 and 4. The decrease of Zn concentration after exposure was certainly the result of the incorporation of Zn in the oxides on the samples. Moreover, the concentration of Fe in the coolant after exposure in Run 5 was higher than that in Run 4, possibly resulting from the replacement of Fe (II) by Zn (II) in the ferrite. However, the concentration of Ni in this run was lower than those in Run 4, possibly due to the Zn addition effect; the protective oxide was produced and acted as a barrier to inhibit the dissolution of the metal ions from the corrosion products and the base materials.

Table 4.38 Coolant chemistry before and after exposure in Run 5

Conditions	Before	After
Boron concentration (ppm)	1993	3370
pH @ room temperature	6.74	6.40
$pH_{300°C}$	7.4	7.3**
Fe concentration (ppb)	-	3.4±1.0
Ni concentration (ppb)	-	very low***
Mn concentration (ppb)	-	24.4±3.1
Zn concentration (ppb)	20*	14.1±1.1

*from the Zn addition

**from the calculation by extrapolation

***below the detection limit

After exposure, all SG samples, SS304-4, SS304-5 and a small part of Zirc-4 were analysed with EDX and SEM for studying the effect of SG alloy heat treatment and composition on oxide formation. Moreover, the results in this run were compared with those in Run 4 for studying the effect of zinc concentration on oxide formation. The results are presented and discussed as follows:

4.2.2.1 EDX and SEM Analyses

All samples were analysed with EDX and SEM on the convex surfaces. Figure 4.48 shows the oxide morphologies of Alloy 600 MA and TT. They were both covered with uniform needle-like oxide and sparse platelet crystals; however, Alloy 600 TT had higher needle-like oxide coverage and had slightly bigger crystals, with higher coverage, than Alloy 600 MA. This observation was different from the results observed on Alloy 600 MA and TT in Run 4, probably because of the zinc addition. However, it is also possible that oxide formed on Alloy 600 TT was more compact than that on Alloy 600 MA, possibly due to the effect of heat treatment.

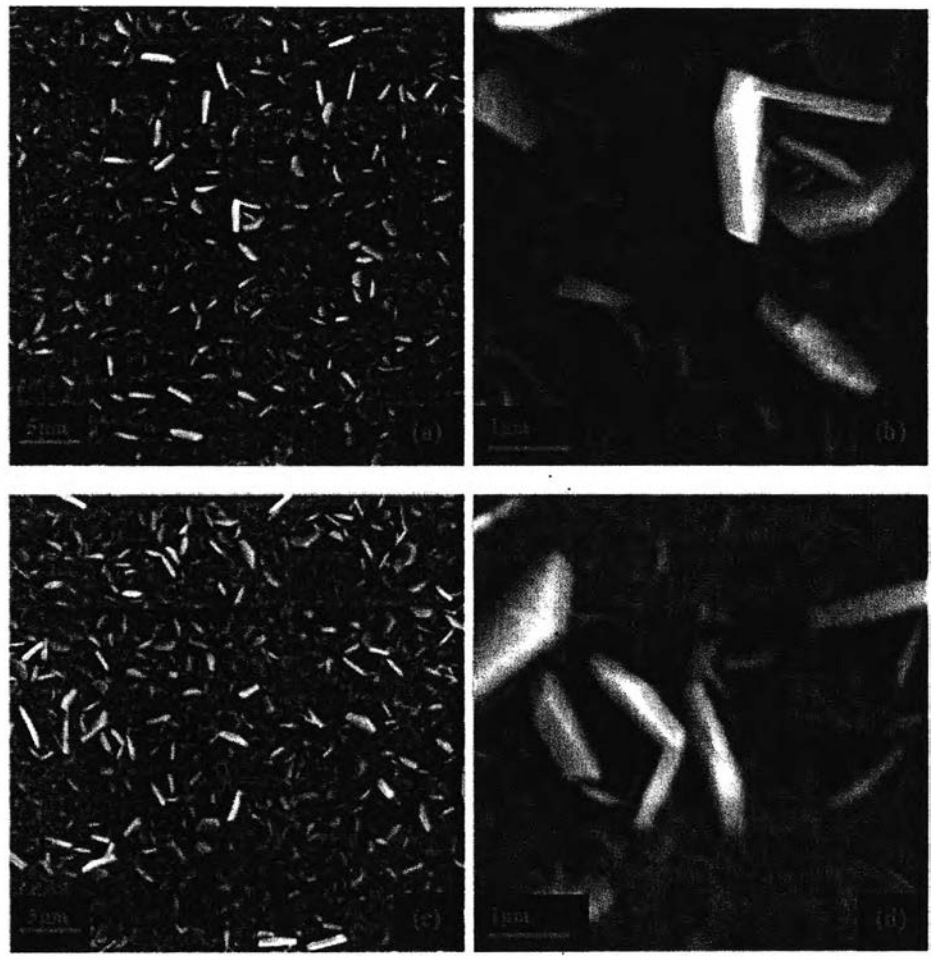

Figure 4.48 SEM images of Alloy 600 MA (a and b) and Alloy 600 TT (c and d) in Run 5.

Table 4.39 and Table 4.40 show the EDX results on Alloy 600 MA and TT, respectively. It should be noted that since the surfaces of Alloy 600 MA and TT were extensively covered with needle-like oxide, the elemental compositions of the underlying layer included results from the needle-like oxide. From the results, the weight percentage of Fe was the highest in the crystallite, while the weight percentage of Cr was the highest in the underlying layer, indicating that the crystallite was Fe-rich and the underlying layer was Cr-rich. Significant amounts of Ti, Zr and Cu were observed in the oxide. Titanium and Zr come from the test section and Zirc-4 sample, while Cu possibly comes from the SG samples and/or the lubricant. In addition, zinc was observed in both the crystallites and the underlying

layer. Note that the apparent concentration of Zn in the underlying layer (including the needles) will have been diluted by the EDX signal from the underlying metal.

Table 4.39 EDX result from the convex surface of Alloy 600 MA in Run 5

Position	Wt%							
	Ni	Fe	Cr	Ti	Cu	Zr	Zn	O
Platelet Crystallite	30.2	24.68	6.35	5.28	0.95	-	2.52	30.02
Underlying layer	64.67	10.7	16.21	1.22	1.32	0.08	0.48	5.32
Before exposure	70.83	9.63	15.40	0.39	*	-	-	2

*was not recorded

Table 4.40 EDX result from the convex surface of Alloy 600 TT in Run 5

Position	Wt%							
	Ni	Fe	Cr	Ti	Cu	Zr	Zn	O
Platelet Crystallite	36.26	21.83	8.11	5.72	1.12	0	2.73	24.23
Underlying layer	58.57	10.7	17.15	1.35	1.12	0.43	0.64	10.04
Before exposure	71.56	9.41	15.09	0.29	*	-	-	2.54

*was not recorded

Figure 4.49 shows oxide morphologies on Alloy 690 MA, TT and CD. The samples were covered with a layer of tiny crystallites with non-uniform large crystallites. The oxides on Alloy 690 TT from Sandvik and from Valinox were slightly different possibly because they were processed with slightly different temperatures and times, as mentioned in Run 4. Figure 4.50 compares the oxide

morphologies on Alloy 690 MA, TT and CD from Valinox. From a comparison of the size of tiny crystallites (difficult to see from the photographs), Alloy 690 TT had the smallest crystallites followed by Alloy 690 MA and CD in order of increasing size. The crystallite coverage on Alloy 690 TT was higher than that on alloy 690 MA and then Alloy 690 CD. This is likely that the layer of tiny crystallites on Alloy 690 TT was more compact than those on Alloy 690 MA and CD. This observation is in agreement with the results observed on Alloy 690 in Run 4.

The elemental compositions in the crystallite and in the underlying layer of Alloy 690 were determined using EDX performed on the biggest crystallite and on the layer of tiny crystallites. From the EDX results on Alloy 690 MA, TT and CD from Valinox, as shown in Table 4.41-4.43, the crystallite had the highest Fe content compared with the underlying layer and the base metal, while the underlying layer had the highest Cr content. These indicate that the crystallites were rich in Fe and the underlying layer was rich in Cr. Significant amounts of Ti and Cu and small amounts of Zr were observed in all oxides. Also, Zn was observed in both the crystallite and the underlying layer, indicating the incorporation of Zn in the oxides. As was the case of Alloy 600, the Zn in the underlying layer will be diluted by the EDX signal from the metal.

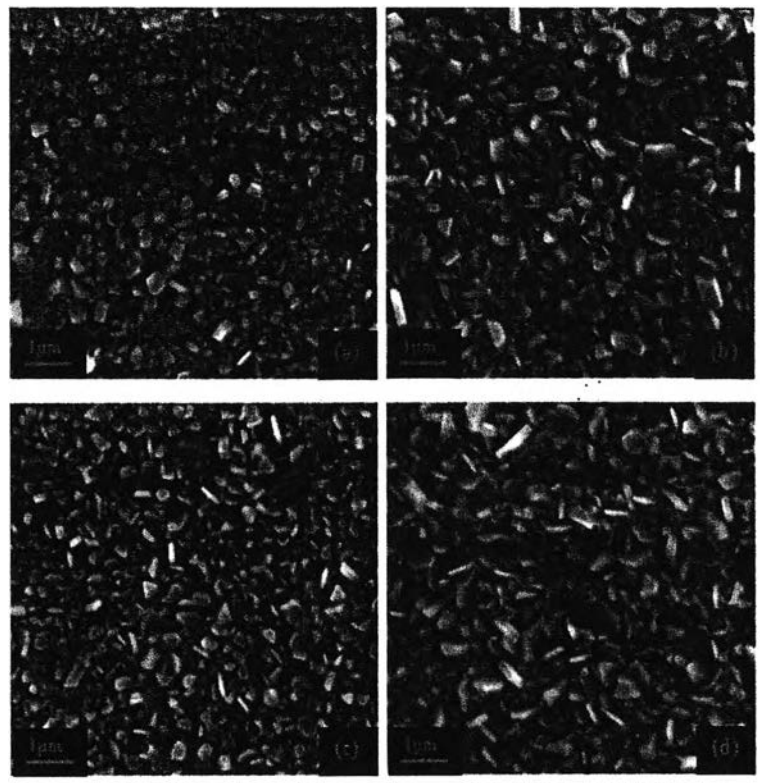

Figure 4.49 SEM images of Alloy 690 MA from Valinox (a), Alloy 690 CD from Valinox (b), Alloy 690 TT from Sandvik (c) and Alloy 690 TT from Valinox (d) in Run 5.

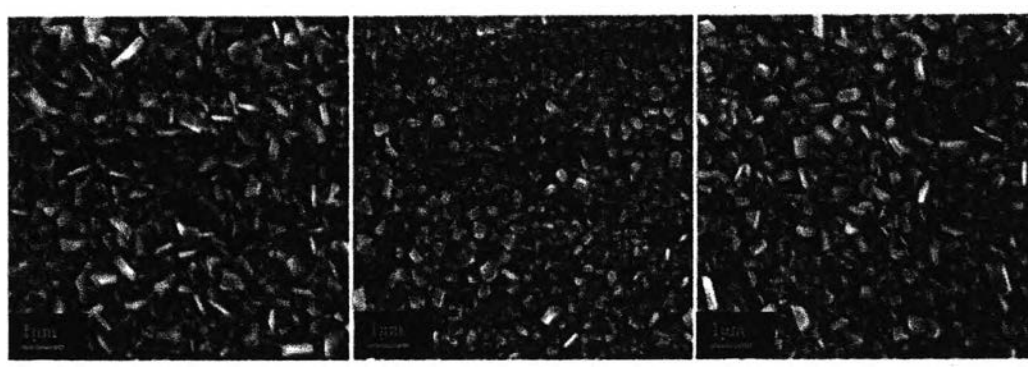

Figure 4.50 Comparison of SEM images of Alloy 690 TT, MA and CD from Valinox in Run 5.

Table 4.41 EDX result from the convex surface of Alloy 690 MA in Run 5

Position	Wt%							
	Ni	Fe	Cr	Ti	Cu	Zr	Zn	O
Crystallite	35.87	20.69	18.53	3.6	0.88	-	2.47	17.96
Underlying layer	50.45	12.95	28.01	1.5	1.09	-	1.39	4.61
Before exposure	56.37	9.47	27.41	0.33	*	-	-	6.42

*was not presented

Table 4.42 EDX result from the convex surface of Alloy 690 TT in Run 5

Position	Wt%							
	Ni	Fe	Cr	Ti	Cu	Zr	Zn	O
Crystallite	20.83	35.8	12.71	3.62	1.21	0.12	2.36	23.35
Underlying layer	49.96	12.93	30.01	1.44	0.77	-	0.76	4.13
Before exposure	57.55	9.80	27.37	0.30	*	-	-	4.98

*was not presented

Table 4.43 EDX result from the convex surface of Alloy 690 CD in Run 5

Position	Wt%							
	Ni	Fe	Cr	Ti	Cu	Zr	Zn	O
Crystallite	21.24	34.27	6.18	4.46	0.67	0.14	2.16	30.88
Underlying layer	52.78	12.02	27.67	1.07	1.06	-	0.92	4.48
Before exposure	57.37	10.03	27.23	0.44	*	-	-	4.93

*was not presented

Oxide morphologies on Alloy 800 MA and SP are shown in Figure 4.51. The samples were covered with a layer of tiny crystallites with large sparse crystallites. However, the crystallites on Alloy 800 MA were slightly bigger, but their coverage was lower, than those on Alloy 800 SP. This is presumably due to the higher defects on Alloy 800 SP by shot peening, resulting in a higher oxide nucleation.

The EDX results on Alloy 800 MA and SP in Table 4.44 and Table 4.45 show that the weight percentage of Cr was the highest in the underlying layer, while the Fe/Cr ratio (not shown) in the crystallite was higher than that in the underlying layer. These indicate that the crystallites were richer in Fe than the underlying layer, which was enriched in Cr. Zinc was observed in the crystallites and in the underlying layer. Titanium, Zr and Cu were also observed in the oxides.

A comparison of the oxides formed on Alloy 600, Alloy 690 and Alloy 800 processed by mill annealing (MA) is shown in Figure 4.52. According to the SEM pictures of the layers of tiny crystallites, the oxide formed on Alloy 690 was more compact than that on Alloy 800 and on Alloy 600. This is due to the Cr content of the alloys; Alloy 690 has the highest Cr content followed by Alloy 800 and then Alloy 600 (Cr is a significant component of protective oxides). Figure 4.53 compares the oxides formed on Alloy 600 and Alloy 690 processed by thermal treatment (TT). Again, Alloy 690 had an apparently more protective oxide than Alloy 600, no doubt because of the higher Cr content. It is clear that the SG alloy compositions, especially Cr content, had a large effect on the oxide morphology. This is consistent with the result found by Delabrouille *et al.* (2005), that the average size of small crystallites decreases with chromium content.

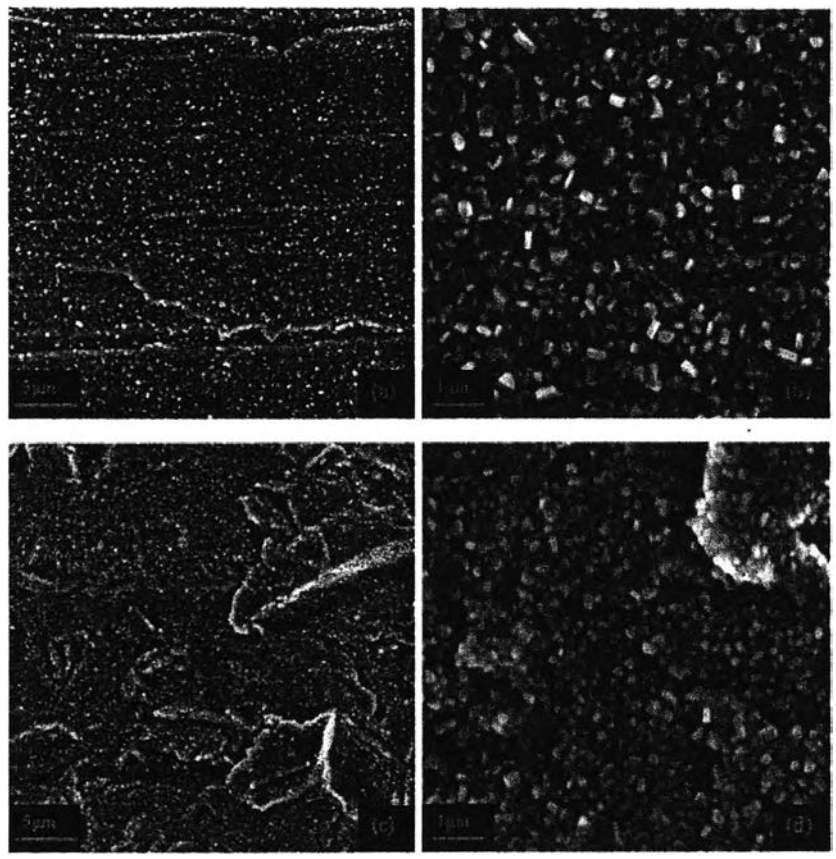

Figure 4.51 SEM images of Alloy 800 MA (a and b) and Alloy 800 SP (c and d) in Run 5.

Table 4.44 EDX result from the convex surface of Alloy 800 MA in Run 5

Position	Wt%							
	Ni	Fe	Cr	Ti	Cu	Zr	Zn	O
Crystallite	17.82	46.12	13.05	0.99	1.14	0.19	1.2	19.49
Underlying layer	30.7	43.23	20.96	0.54	1.29	0.25	0.62	2.41
Before exposure	31.94	43.04	19.29	0.35	*	-	-	5.38

*was not recorded

Table 4.45 EDX result from the convex surface of Alloy 800 SP in Run 5

Position	Wt%							
	Ni	Fe	Cr	Ti	Cu	Zr	Zn	O
Crystallite	12.04	34.85	9.95	1.07	0.22	0.11	1.24	40.52
Underlying layer	29.11	39.52	21.93	1.12	1.08	0.12	0.83	6.29
Before exposure	31.59	41.96	20.96	0.54	*	-	-	4.95

*was not recorded

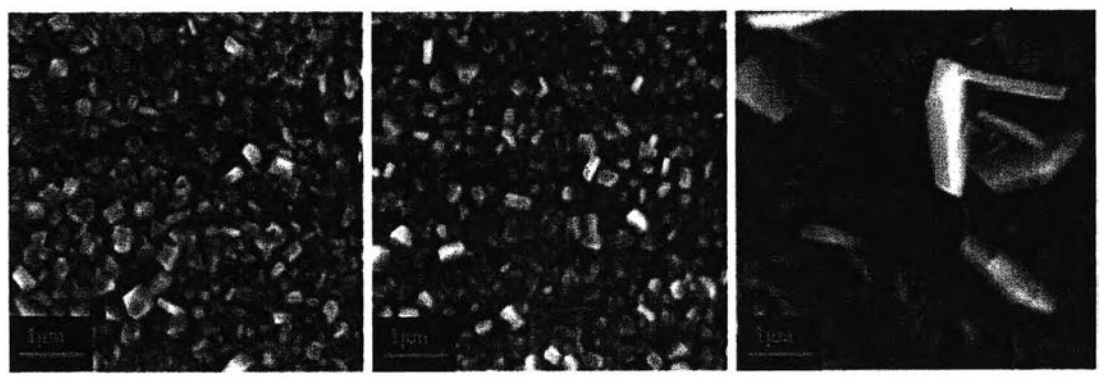

Alloy 690 MA Alloy 800 MA Alloy 600 MA

Figure 4.52 Comparison of SEM images of Alloy 600 MA, Alloy 690 MA and Alloy 800 MA in Run 5.

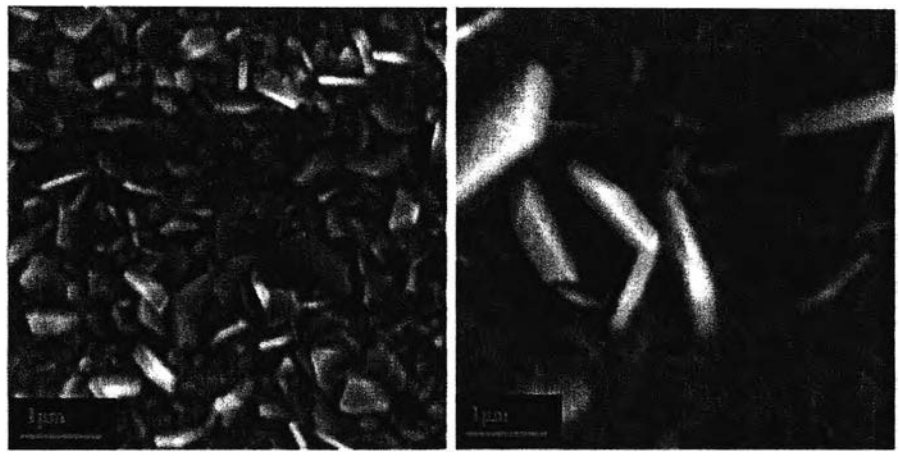

Alloy 690 TT Alloy 600 TT

Figure 4.53 Comparison of SEM images of Alloy 600 TT and Alloy 690 TT in Run 5.

In this run, the oxide morphologies on SS304 samples were represented by the oxide formed on SS304-4 (weight loss) and SS304-5 (weight gain) as shown in Figure 4.54. They were both covered almost identically with a layer of small crystallites and much larger crystallites (randomly distributed) overlaying an amorphous layer (difficult to see from micrographs), even though their weight changes were different. From the EDX results in Table 4.46 and Table 4.47, the major constituents in the large crystallites were Fe and Ti and the Fe/Ti ratio was equal to one, indicating that the large crystallites were possibly ilmenite ($FeTiO_3$). From a comparison of the EDX results on the small crystallite layer and the underlying layer, the weight percentages of Fe and Cr in the underlying layer were higher, but its Fe/Cr ratio was lower than that in the small crystallite layer. It indicates that the small crystallite layer was Fe-rich and the underlying layer was Cr-rich, possibly Ni-Fe chromite. The weight percentage of Zn was higher in the small crystallite layer than in the large crystallites or the underlying layer. This suggests that the incorporation of Zn in the oxide seems to produce fine crystals (close to the underlying layer or inner layer), resulting in the formation of tighter and more protective oxide, corresponding with the oxide formed on SS304 in the presence of Zn reported by Ziemniak and Hanson (2006) and Niedrach and Stoddard (1985).

However, EDX signals from thin underlying oxide are always confounded with signals from the metal.

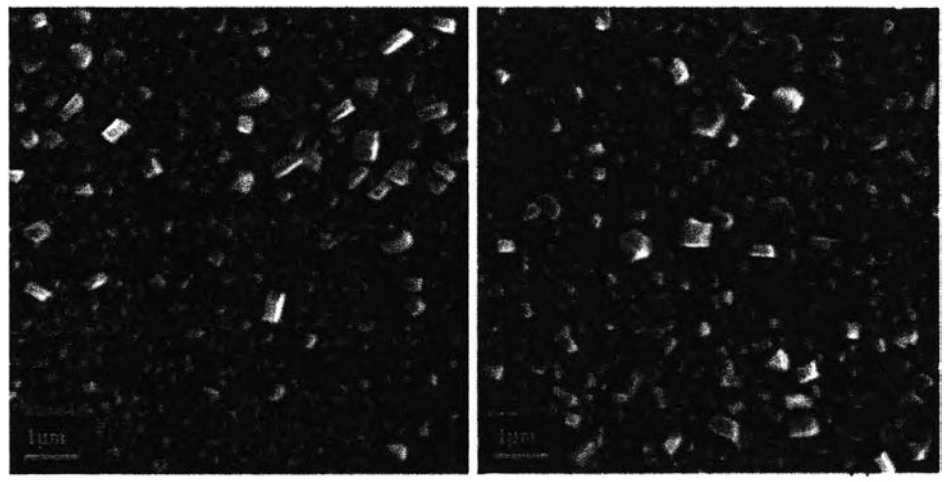

SS304-4 SS304-5

Figure 4.54 SEM images of SS304-4 and SS304-5 in Run 5.

Table 4.46 EDX result from the convex surface of SS304-4 in Run 5

Position	Wt%						
	Ni	Fe	Cr	Ti	Zn	O	Fe/Cr
Large Crystallite	3.38	25.52	2.7	25.06	0.68	41.72	9.45
Small Crystallite	6.49	53.06	10.75	1.03	1.24	26.18	4.94
Underlying layer	10.3	60.74	19.12	0.36	0.45	7.91	3.18

Table 4.47 EDX result from the convex surface of SS304-5 in Run 5

Position	Wt%						
	Ni	Fe	Cr	Ti	Zn	O	Fe/Cr
Large Crystallite	1.77	29.5	2.01	28.63	1.12	36.25	14.68
Small Crystallite	5.78	51.98	9.91	1.03	1.28	28.52	5.24
Underlying layer	10.37	57.31	18.31	0.57	1.15	10.52	3.13

On the Zirc-4 sample, an amorphous oxide was observed over all the surface, while platelet and elongated oxides were observed at scratches, as shown in Figure 4.55. Moreover, there were oxide crystals sparsely scattered on over the surface. From the EDX result in Table 4.48, the major constituent in the amorphous, platelet and elongated oxides was Zr, no doubt as ZrO_2. The oxide crystals were likely ilmenite ($FeTiO_3$) because their major constituents were Fe and Ti, with a Fe/Ti ratio close to one. The weight percentage of Zn was very low on this material.

Figure 4.55 SEM images of Zirc-4 in Run 5.

Table 4.48 EDX result from the surface of Zirc-4 in Run 5

Position	Wt%						
	Ni	Fe	Cu	Zr	Ti	Zn	O
Amorphous oxide	0.52	0.86	0.45	69.1	0.56	0.42	28.09
Platelet/Elongate oxide	0.19	1.36	0.18	58.81	1.05	-	38.41
Crystal oxide	1.04	29.88	-	0.63	30.27	0.42	37.76

A comparison of oxides formed on samples exposed to the Zn-free coolant (Run 4) with those exposed to the coolant containing 20 ppb Zn (Run 5) is shown in Figure 4.56-4.60 In both cases the crystallites on SG and SS304 samples presented a bimodal size distribution of large crystallites (non-uniformly distributed) and small crystallites (uniformly distributed), but their crystallite sizes, shapes and coverages were different, possibly due to a zinc effect and a slightly different coolant pH. Since the small crystallites in Run 5 were smaller than those in Run 4, presumably due to the formation of stable oxide ($ZnFe_2O_4$) instead of ferrite oxide with a high nucleation rate, it is likely that the SG and SS304 samples in Run 5 had more protective oxide layers than those in Run 4. This protective oxide probably results in the darker color than in Run 4, as mentioned earlier, and may have contributed to the difference in large crystallite shape and coverage.

From the EDX results, Zn was observed in the crystallites and in the underlying layer in the presence of 20 ppb zinc, indicating that Zn was incorporated in the crystallites possibly as Zn-ferrite, and in the underlying layer possibly as Zn-chromite. According to lattice energies of spinels as shown in Table 2.4, $ZnCr_2O_4$ has the highest lattice energy (the highest stability) compared with other spinels. Furthermore, the concentration of Zn added (20 ppb) was high enough to have high soluble Zn(II) in the coolant, relative to soluble Fe(II) and Ni(II). Thus, it is reasonable that Zn prefers to form $ZnCr_2O_4$ in the underlying layer (as an inner oxide layer) than to form Zn-Ni ferrite in the crystallites (as an outer oxide layer). Note that, as mentioned earlier, the EDX results show that the weight percentage of Zn in the crystallite was higher than that in the underlying layer, probably because of interference of the EDX signal from the base metal in the underlying layer result.

The oxides formed on Zirc-4 samples in Run 4 and Run 5 were similar and the weight percentage of Zn on oxide formed on Zirc-4 in the presence of 20 ppb Zn was very low. Therefore, it is likely that there was no, or only a small, effect of zinc on oxide formed on Zirc-4. However, the corrosion rates of Zirc-4 in Run 4 and Run 5 were different, as shown in Table 4.49. Zircaloy-4 in Run 5 had much lower corrosion rate, possibly because the top section of Zirc-4 coil in Run 5 was not exposed to the coolant due to the leak at the start of exposure. From an adjustment the surface area of Zirc-4 coil in Run 5 to the amount of exposed

surface (~0.52 dm^2), the corrosion rate came to 0.88 mdd; however, it was still lower than that in Run 4, possibly due to the slightly different coolant pH.

Titanium, Zr and Cu were observed in all oxides in Run 4 and Run 5, but the proportion of Ti incorporated in the crystallites on Alloy 600 and Alloy 690 in Run 5 was higher than in Run 4, probably because of the higher Ti concentration in the coolant, relative to other ions.

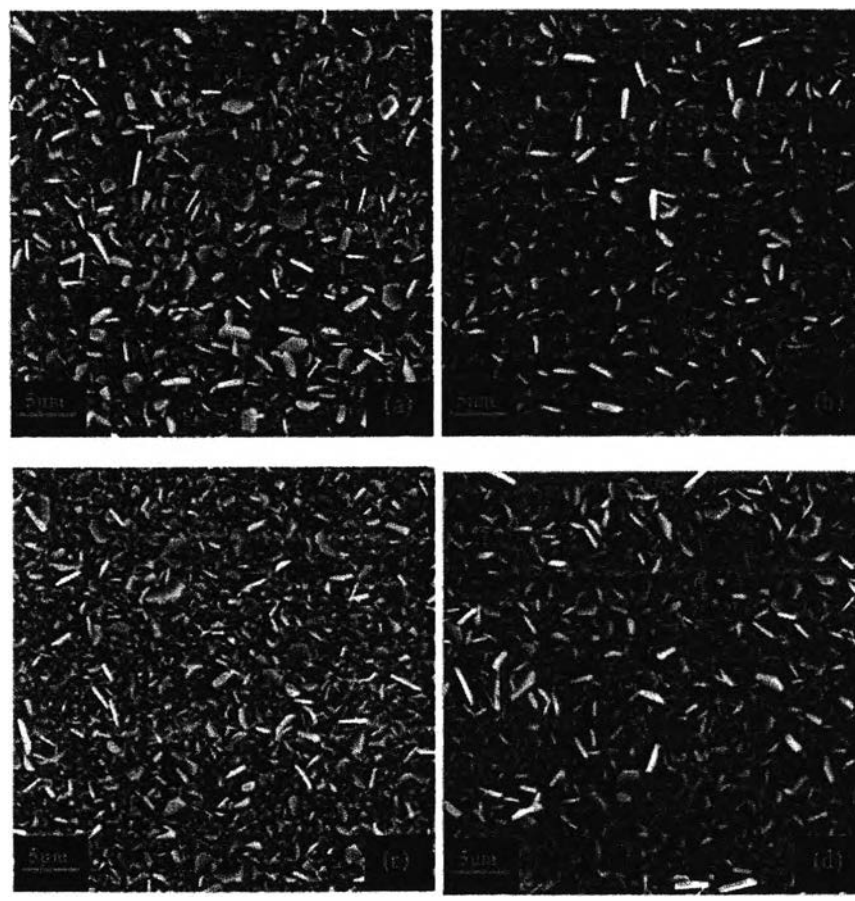

Figure 4.56 Comparison of the surface morphologies of Alloy 600 MA (a) and Alloy 600 TT (c) in Run 4 with Alloy 600 MA (b) and Alloy 600 TT (d) in Run 5.

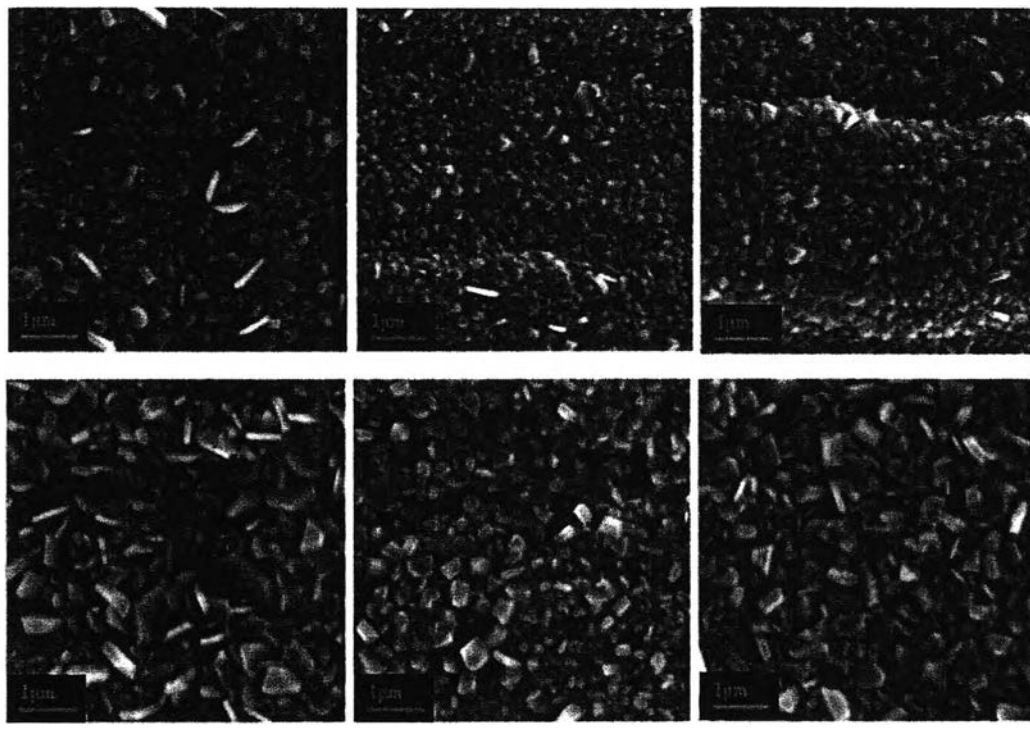

Figure 4.57 Comparison of the surface morphologies of Alloy 690 TT, MA and CD in Run 4 (top) with Alloy 690 TT, MA and CD in Run 5 (below).

In summary, according to the EDX and SEM results, it can be summarized that Zn was incorporated in the oxides on the SG and SS304 samples, resulting in the formation of protective oxide layer close to the underlying layer. Nevertheless, it cannot be exactly discussed that Zn was favorably incorporated in the crystallites (outer oxide layer) or in the underlying layer (inner oxide layer) and what is the oxide phase formed by zinc incorporation. These conclusions can be evaluated using other surface analysis techniques, i.e. SIMS and XPS. On the other hand, there was no, or a small, effect of zinc on the morphology of the oxide formed on Zirc-4 sample, although the corrosion rate was apparently reduced. However, the effect of Zn will be confirmed by a comparison of the results between Run 8 and Run 9.

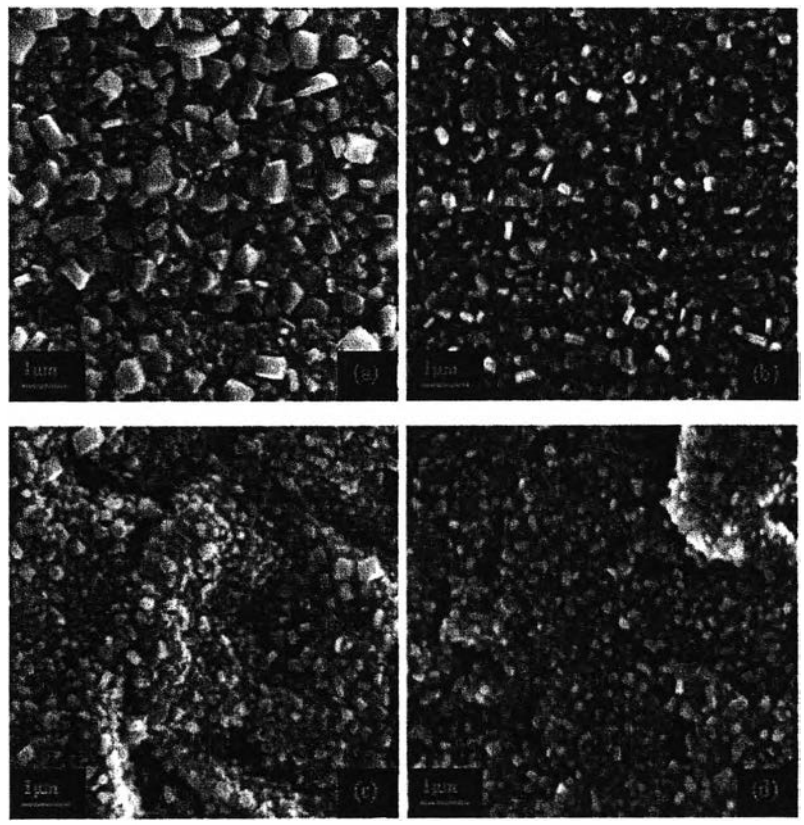

Figure 4.58 Comparison of the surface morphologies of Alloy 800 MA (a) and Alloy 800 SP (c) in Run 4 with Alloy 800 MA (b) and Alloy 800 SP (d) in Run 5.

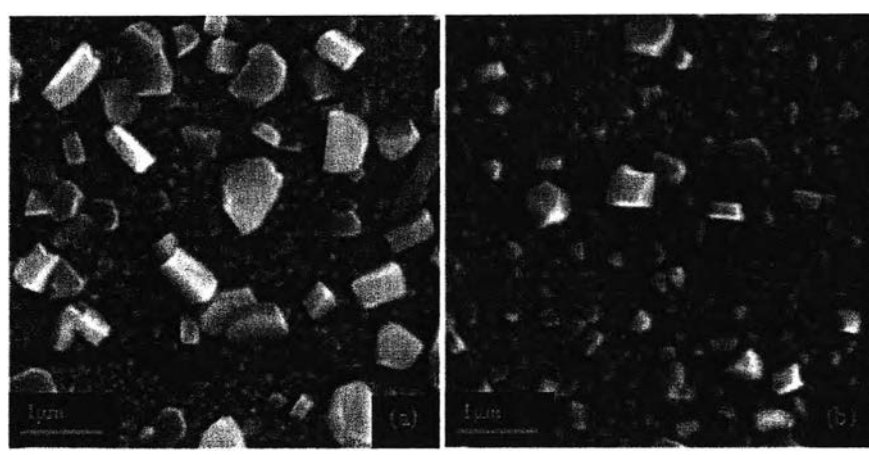

Figure 4.59 Comparison of the surface morphologies of SS304 in Run 4 (a) with SS304 in Run 5 (b).

Figure 4.60 Comparison of the surface morphologies of Zirc-4 in Run 4 (a) with Zirc-4 in Run 5 (b).

Table 4.49 Comparison of Zirc-4 corrosion rate between Run 4 and Run 5

Zirc-4 sample	Surface Area (dm^2)	Weight Change (mg)	Exposure Time (days)	Corrosion rate (mdd)
Run 4	0.8778	+67	30	2.54
Run 5	0.8728	+13.8	30	0.53

4.2.3 Run 6

Run 6 and Run 7 were undertaken to investigate the effect of boron on oxide film formation, which was unclear from the comparison of the results in Run 1 with those in Run 2 due to the exposure time effect. The samples used in these two runs were the same as those in Run 1 and Run 2; Alloy 600 MA, SS304 and Zirc-4, but there was no heat flux through the surface of Alloy 600 MA and Zirc-4 samples, resulting in no sub-cooled boiling on the Zirc-4 surface. Figure 4.61 shows photographs of the samples before and after exposure. After exposure, the Alloy 600 MA sample was slightly darker, while the SS304 and Zirc-4 samples were much darker than before exposure.

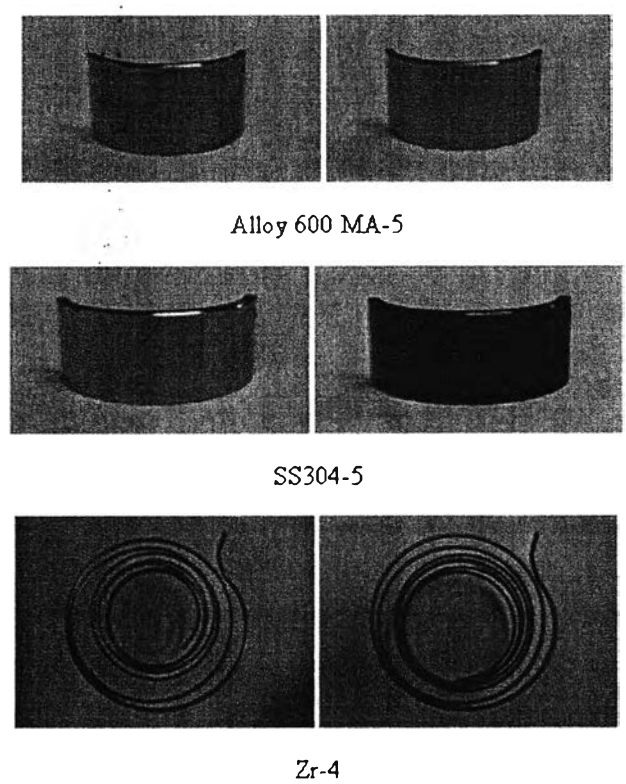

Figure 4.61 Samples before (left) and after (right) exposure in Run 6.

The weight changes of samples are shown in Table 4.50. All SG samples and Zirc-4 sample gained weight, but all SS304 samples lost weight, probably due to the dissolution of metal ions from the material.

Table 4.50 Weight of the samples before and after exposure in Run 6

Sample	Surface Area (cm^2)	Before (g)	After (g)	Weight Change (mg)	Weight change per unit area (mg/dm^2)
Zircaloy-4	87.28	22.6975	22.7048	+7.3	+8.36
SS304-1	9.02	4.2854	4.2850	-0.4	-4.43
SS304-2	9.02	4.2655	4.2653	-0.2	-2.22
SS304-3	9.02	4.1872	4.1869	-0.3	-3.32
SS304-4	9.02	4.2544	4.2542	-0.2	-2.22
SS304-5	9.02	4.5053	4.5051	-0.2	-2.22
SS304-6	9.02	4.3525	4.3523	-0.2	-2.22
SS304-7	9.02	4.3936	4.3934	-0.2	-2.22
SS304-8	9.02	4.3841	4.3840	-0.1	-1.11
Alloy 600MA-1 (Westinghouse)	6.52	2.3114	2.3116	+0.2	+3.07
Alloy 600MA-2 (Westinghouse)	6.52	2.3069	2.3070	+0.1	+1.53
Alloy 600MA-3 (Westinghouse)	6.52	2.3912	2.3913	+0.1	+1.53
Alloy 600MA-4 (Westinghouse)	6.52	2.3633	2.3634	+0.1	+1.53
Alloy 600MA-5 (Westinghouse)	6.52	2.3602	2.3602	0.0	0.0
Alloy 600MA-6 (Westinghouse)	6.52	2.3721	2.3721	0.0	0.0
Alloy 600MA-7 (Westinghouse)	6.52	2.3565	2.3566	+0.1	+1.53
Alloy 600MA-8 (Westinghouse)	6.52	2.3481	2.3482	+0.1	+1.53

The coolant pH, boron concentration and iron concentration before and after exposure were measured, as shown in Table 4.51. The boron concentrations and the pH values before and after exposure were slightly different. The differences, however, were within the measurement error. In this run, the concentrations of Ni, Fe and Mn after exposure, which resulted from the dissolution of these metal ions from the corrosion products and the base materials, seemed lower than those in Runs 1, 3, 4 and 5. This is possibly due to the shorter exposure time. The Zn concentration in this run was relatively high, although there was no Zn addition, no doubt due to the residual contamination with Zn from Run 5 and possibly due to the residual Zn contamination from the lubricant and/or from the previous work, as mentioned earlier.

Table 4.51 Coolant chemistry before and after exposure in Run 6

Conditions	Before	After
Boron concentration (ppm)	1990	2015
pH @ room temperature	6.32	6.39
$pH_{300°C}$	7.01	7.01
Fe concentration (ppb)	-	2.2±1.0
Ni concentration (ppb)	-	very low**
Mn concentration (ppb)	-	8.7±3.1
Zn concentration (ppb)	0.4*	10.5±1.1

*from the de-ionized water

**below the detection limit

The oxides formed on the samples were analysed with SEM and EDX. The results in this run will be compared with the results in Run 7 in order to examine effect of boron. The results are presented and discussed as follows:

4.2.3.1 EDX and SEM Analyses

Figure 4.62 shows oxide morphology on the convex surface of Alloy 600 MA. It was covered with needle-like oxide on the entire surface without any crystallites, no doubt due to the shorter exposure time (5 days), similar to the oxide observed on Alloy 600 MA in Run 1. From the EDX result in Table 4.52, the weight percentages of Ni and Fe in the oxide were lower, but the weight percentage of Cr was higher, than those in the base material, possibly indicating the dissolution of Ni and Fe and the formation of Cr-rich oxide in the first stage of corrosion. Small amounts of Ti and Zr come from the test section and Zirc-4 sample, respectively. Copper possibly comes from the base material of SG samples and/or from the lubricant. Moreover, Zn was observed in the oxide, no doubt due to residual contamination with Zn from Run 5.

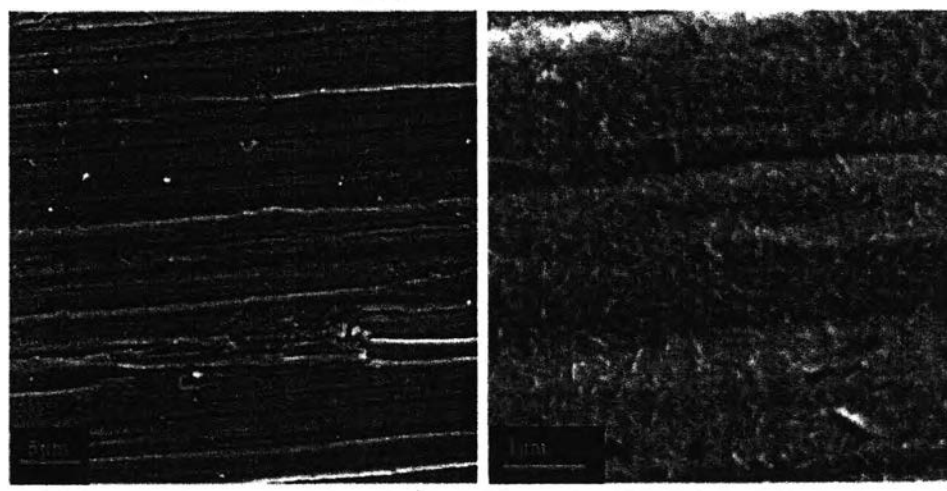

Figure 4.62 SEM images of Alloy 600 MA in Run 6.

Table 4.52 EDX result from the convex surface of Alloy 600 MA in Run 6

Position	Wt%							
	Ni	Fe	Cr	Ti	Cu	Zr	Zn	O
Needle-like oxide	67.11	9.06	16.01	0.42	1.25	0.06	0.23	5.86
Before exposure	70.83	9.63	15.40	0.39	*	-	-	2

*was not presented

Oxide morphology on the SS304 sample is shown in Figure 4.63. The sample was covered with a layer of small crystallites mixed with large, sparse crystallites overlaying an amorphous layer. It shows that the oxide morphologies of Alloy 600 MA and SS304 were different, even though they were exposed to the same coolant and for the same time; this is possibly due to their corrosion resistances and compositions. The EDX was performed on the crystallites and on the underlying layer (an area between the small crystallites). The results show that the weight percentage of Cr in the underlying layer was higher, but the Fe/Cr ratio was lower, than in the crystallites. It indicates that the crystallites were richer in Fe than the underlying layer, which was enriched in Cr. Titanium, Zr and Cu were observed in the oxide. Again, Zn was observed in both the crystallites and the underlying layer because of the contamination of Zn from Run 5. Since the weight percentage of Zn observed in the underlying layer was higher than that in the crystallites, it presumably confirms that Zn prefers to be incorporated in the inner oxide layer than in the crystallites, as mentioned earlier in Run 5.

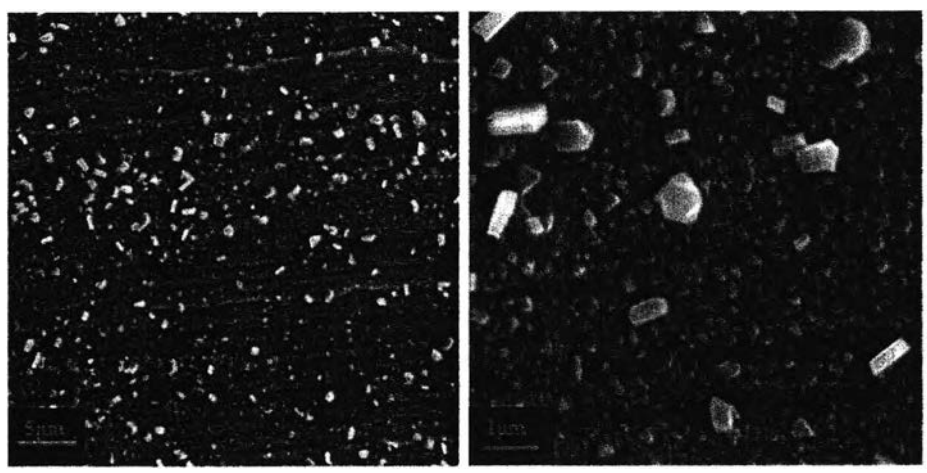

Figure 4.63 SEM images of SS304 in Run 6.

Table 4.53 EDX result from the convex surface of SS304 in Run 6

Position	Wt%								
	Ni	**Fe**	**Cr**	**Ti**	**Cu**	**Zr**	**Zn**	**O**	**Fe/Cr**
Crystallite layer	4.55	58.12	9.13	0.77	0.28	0.13	0.42	26.61	6.36
Underlying layer	9.81	59.45	19.43	0.56	0.82	0.16	0.89	8.89	3.06

From a comparison with oxide morphology on SS304 in Run 3, which was exposed to the similar coolant for a longer time, the number of large crystallites on SS304 in Run 3 (10 days) seemed higher and the small crystallite coverage seemed higher, than in this run (5 days), as shown in Figure 4.64, due to the longer exposure time. This observation possibly suggested that the crystallite size and coverage on SS304 increase with increasing time, consistent with the comparison of the oxide morphology on SS304 in Run 3 with that in Run 4, which was explained in Run 4.

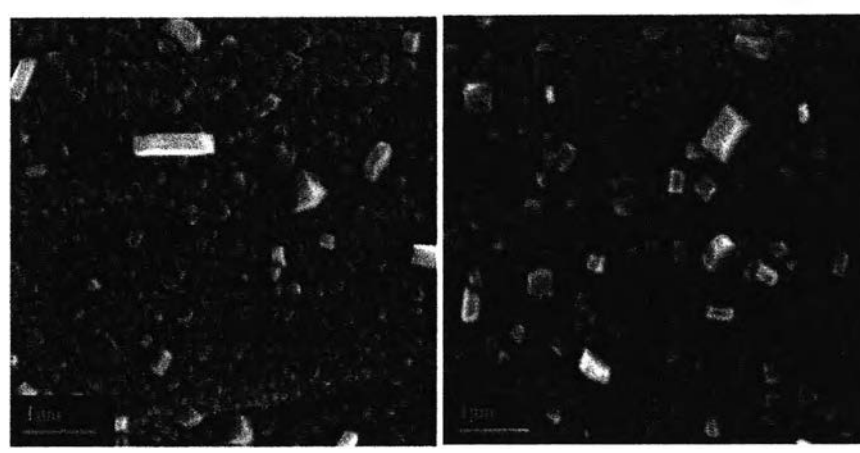

Run6 (120 h) **Run3 (240 h)**

Figure 4.64 Comparison of the surface morphologies of SS304 in Run 6 (a) with SS304 in Run 3 (b).

Figure 4.65 shows the oxide morphology on the Zirc-4 sample. All the surface of the sample was covered with an amorphous oxide. Platelet and elongated oxides were observed at scratches. The EDX results in Table 4.54 show that the major constituent of these oxides was Zr, indicating that these oxides were probably ZrO_2.Small amounts of Ti, Cu and Zn were observed in these oxides.

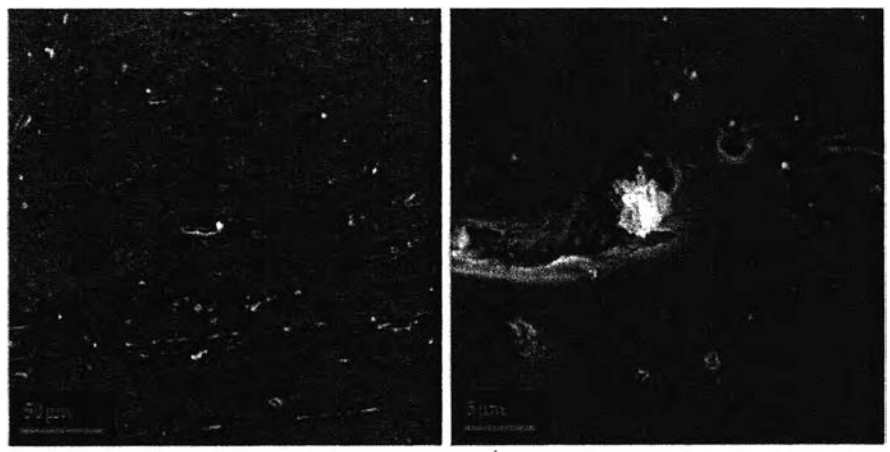

Figure 4.65 SEM images of Zirc-4 in Run 6.

Table 4.54 EDX result from the convex surface of Zirc-4 in Run 6

Position	Wt%						
	Ni	Fe	Cu	Zr	Ti	Zn	O
Amorphous oxide	0.39	0.88	0.36	64.7	0.32	0.32	33.03
Platelet/Elongate oxide	0.54	1.09	0.47	63.62	0.63	0.55	33.1

4.2.4 Run 7

Samples in this run were the same as those in Run 6, as mentioned earlier, but they were exposed to the coolant without boron concentration (but same temperature and pH_T) for studying the effect of boron concentration on oxide film formation. During exposure, samples were darkened, as shown in Figure 4.66.

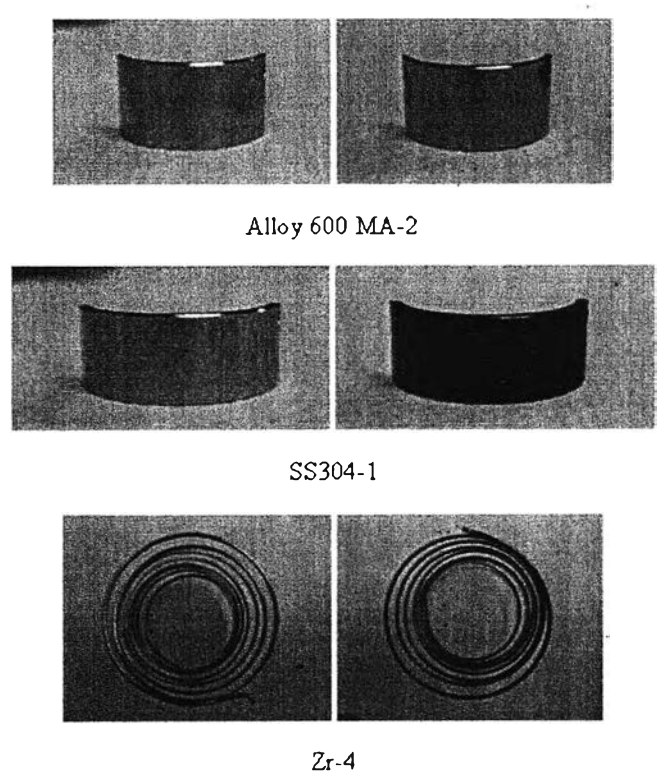

Figure 4.66 Samples before (left) and after (right) exposure in Run 7.

The weight changes of the samples are shown in Table 4.55. Most of the Alloy 600 MA samples lost weight, while the Zirc-4 sample and most of the SS304 samples gained weight. The weight changes of Alloy 600 MA and SS304 are different from those in Run 6, probably due to the effect of boron.

Table 4.55 Weight of the samples before and after exposure in Run 7

Sample	Surface Area (cm^2)	Before (g)	After (g)	Weight Change (mg)	Weight change per unit area (mg/dm^2)
Zircaloy-4	87.28	22.6401	22.6471	+7.0	+8.02
SS304-1	9.02	4.4475	4.4473	-0.2	-2.22
SS304-2	9.02	4.1417	4.1417	0.0	0.0
SS304-3	9.02	4.2865	4.2866	+0.1	-1.11
SS304-4	9.02	4.3790	4.3795	+0.5	+5.54
SS304-5	9.02	4.3321	4.3321	0.0	0.0
SS304-6	9.02	4.3369	4.3370	+0.1	+1.11
SS304-7	9.02	4.2845	4.2844	-0.1	-1.11
SS304-8	9.02	4.2171	4.2172	+0.1	+1.11
Alloy 600MA-1 (Westinghouse)	6.52	2.3550	2.3548	-0.2	-3.07
Alloy 600MA-2 (Westinghouse)	6.52	2.3706	2.3707	+0.1	+1.53
Alloy 600MA-3 (Westinghouse)	6.52	2.3513	2.3512	-0.1	-1.53
Alloy 600MA-4 (Westinghouse)	6.52	2.3723	2.3721	-0.2	-3.07
Alloy 600MA-5 (Westinghouse)	6.52	2.3662	2.3660	-0.2	-3.07
Alloy 600MA-6 (Westinghouse)	6.52	2.3761	2.3761	0.0	0.0
Alloy 600MA-7 (Westinghouse)	6.52	2.3265	2.3264	-0.1	-1.53
Alloy 600MA-8 (Westinghouse)	6.52	2.3412	2.3412	0.0	0.0

Table 4.56 shows boron concentration, coolant pH and iron concentration before and after exposure. Since there was no boron concentration in this run, the coolant $pH_{300°C}$ was kept the same as that in Run 6 using a small amount of lithium hydroxide ($LiOH.H_2O$), which is a strong base. The measured pH of solution containing few H^+ or OH^- can be interfered with by other dissolved species, resulting in the change in pH value. Therefore, the different pH between before and after exposure is probably due to the interference from other dissolved ions in the autoclave. The Ni, Fe and Mn concentrations after exposure were higher than those before exposure, no doubt due to the dissolution of these metal ions from the corrosion products and the base materials. A comparison of the Ni, Fe and Mn concentrations in Run 7 with those in Run 6 shows that they were slightly different because the samples in Run 6 and Run 7 were exposed to the similar coolant conditions for the same time. The Zn concentration after exposure was higher than that before exposure, possibly resulting from the residual Zn contamination from the lubricant and from the previous work, but it was lower than that in Run 6, possibly because the residual contamination with Zn effect from Run 5 was lessened.

Table 4.56 Coolant chemistry before and after exposure in Run 7

Conditions	Before	After
Boron concentration (ppm)	0	0
pH @ room temperature	9.62	7.74
$pH_{300°C}$**	7.01	7.01
Fe concentration (ppb)	-	very low***
Ni concentration (ppb)	-	1.7±0.93
Mn concentration (ppb)	-	6.3±3.1
Zn concentration (ppb)	0.4*	1.5±1.1

*from the de-ionized water

**was calculated from boron and lithium concentration before exposure

***below the detection limit

The oxide films formed on the samples in this run were also analysed with EDX and SEM and the results were compared with those in Run 6 in order to emphasize the effect of boron on oxide film formation. In addition, the oxide formed on SS304 sample in this run was compared with that in Run 2 to confirm the effect of temperature on oxide film formation. The results are presented and discussed as follows:

4.2.4.1 EDX and SEM Analyses

The oxide morphology on Alloy 600 MA in Figure 4.67 shows that Alloy 600 MA was covered with needle-like oxides on all surfaces. From a comparison with the oxide formed on Alloy 600 MA in Run 6, as shown in Figure 4.68, the needle-like oxides on Alloy 600 MA in this run were slightly bigger, while their coverage was lower than those in Run 6, possibly from the boron effect. This observation confirmed that the bigger needle-like oxides in Run 2, compared with the needle-like oxides in Run 1, resulted from the boron effect, but not from the effect of exposure time, as expected. It seems that the oxide formed on Alloy 600 MA in Run 6 (with boron) was more protective than that in this run (without boron), presumably due to the incorporation of boron into the oxide, as indicated by Kawamura *et al.* (2002).

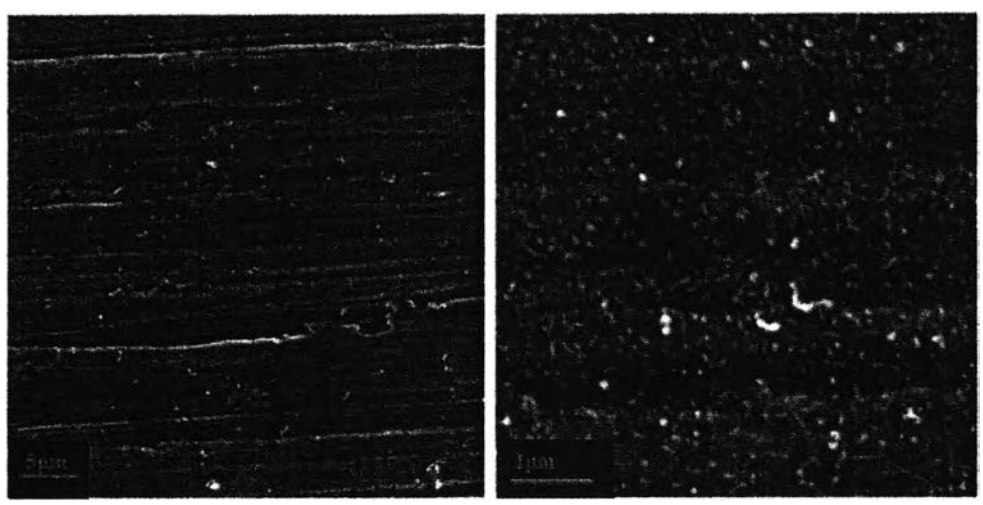

Figure 4.67 SEM images of Alloy 600 MA in Run 7.

The EDX results on Alloy 600 MA in Table 4.57 show that the weight percentages of Ni and Fe in the needle-like oxide were lower, but the weight percentage of Cr was higher, than those in the base material. This may have been due to the dissolution of Ni and Fe from the material and the formation of Cr-rich oxide on the surface. Small amounts of Ti, Zr, Cu and Zn were observed in this oxide.

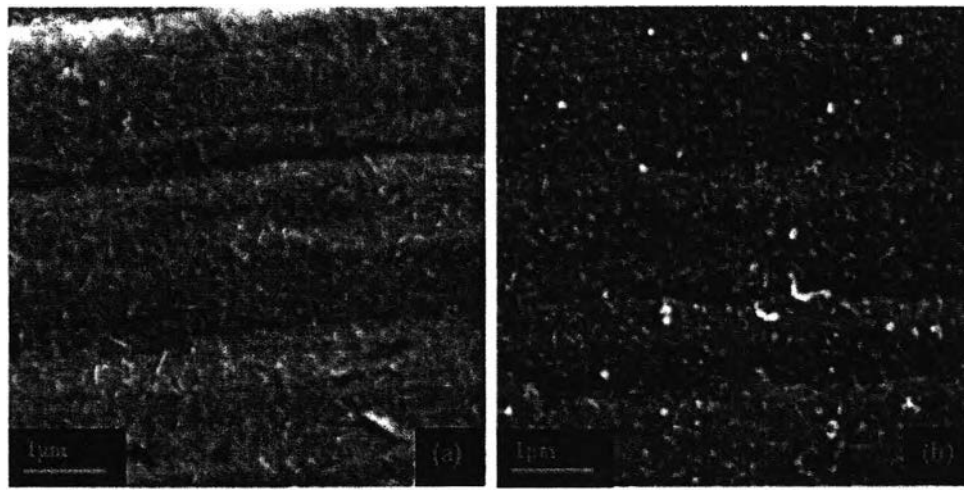

Figure 4.68 Comparison of the surface morphologies of Alloy 600 MA in Run 6 (a) with Alloy 600 MA in Run 7 (b).

Table 4.57 EDX result from the convex surface of Alloy 600 MA in Run 7

Position	Wt%							
	Ni	Fe	Cr	Ti	Cu	Zr	Zn	O
Needle-like oxide	67.45	9.18	16.28	0.33	1.36	0.11	0.24	5.05
Before exposure	70.83	9.63	15.40	0.39	*	-	-	2

*was not recorded

Figure 4.69 (b) shows oxide morphology of SS304 in this run. The SS304 sample was covered with a layer of small crystallites with large sparse crystallites overlaying an amorphous layer, as observed on SS304 in Run 6. However, the crystallites in this run were bigger, while their coverage was lower than

those in Run 6, as shown in Figure 4.69. Thus, the oxide formed on SS304 in Run 6 (with boron) was more protective than that in this run (without boron). This observation is consistent with the results observed on Alloy 600 MA, again possibly resulting from the incorporation of boron in the oxide.

The EDX results on SS304 sample tabulated in Table 4.58 show that the underlying layer had the highest Cr content, while the large and small crystallites had higher Fe/Cr ratio than the underlying layer, indicating that the large and small crystallites were Fe-rich and the underlying layer was Cr-rich. Also, Ti and Zn were observed in both the crystallites and the underlying layer.

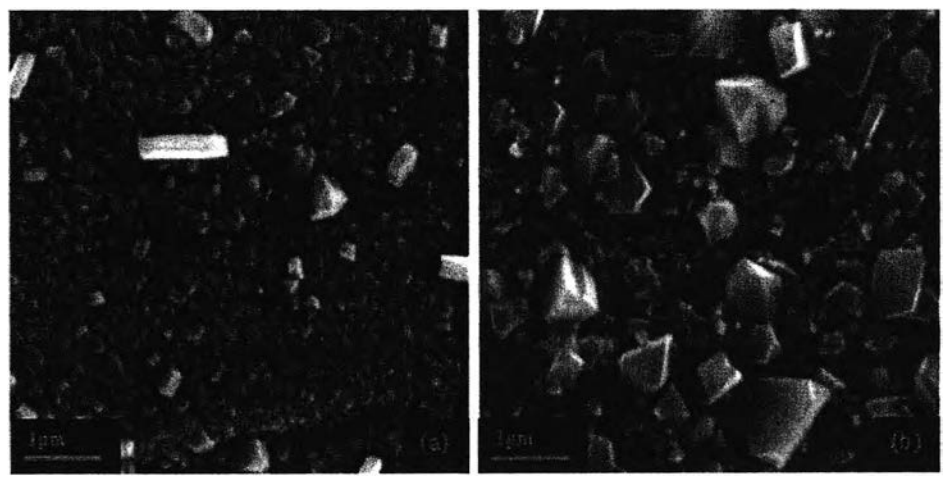

With boron **Without boron**

Figure 4.69 Comparison of the surface morphologies of SS304 in Run 6 (a) with SS304 in Run 7 (b).

Table 4.58 EDX result from the convex surface of SS304 in Run 7

Position	Wt%						
	Ni	Fe	Cr	Ti	Zn	O	Fe/Cr
Large crystallite	3	54.43	6.07	0.84	0.5	33.89	8.97
Small crystallite	7.19	57.7	14.17	0.38	0.59	18.02	4.07
Underlying layer	10.11	58.29	19.21	0.11	0.52	9.85	3.03

A comparison of the oxide on SS304 in this run with that in Run 2, as shown in Figure 4.70 shows that SS304 in this run, which was exposed to higher temperature, had smaller crystallites with a higher coverage than SS304 in Run 2. This is possibly due to the higher corrosion rate, resulting in the higher oxide nucleation. This observation confirms that the oxide coverage increases with increasing temperature, as observed previously from the comparison of the oxide on SS304 in Run 1 with that in Run 3.

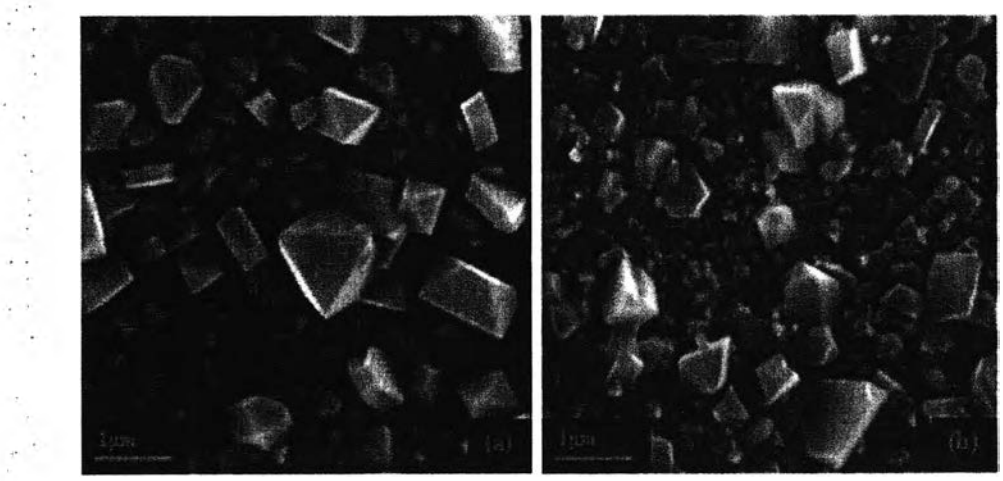

Run2 (295°C) Run7 (300°C)

Figure 4.70 Comparison of the surface morphologies of SS304 in Run 2 (a) with SS304 in Run 7 (b).

Oxide morphology in Figure 4.71 shows that Zirc-4 in Run 7 was completely covered with an amorphous oxide and there were some elongated oxides found at scratches. The EDX results in Table 4.59 show that Zr was a majority constituent in the amorphous and elongated oxides, indicating that these oxides were probably ZrO_2. Moreover, Ti, Cu and Zn were found in a small amount in these oxides.

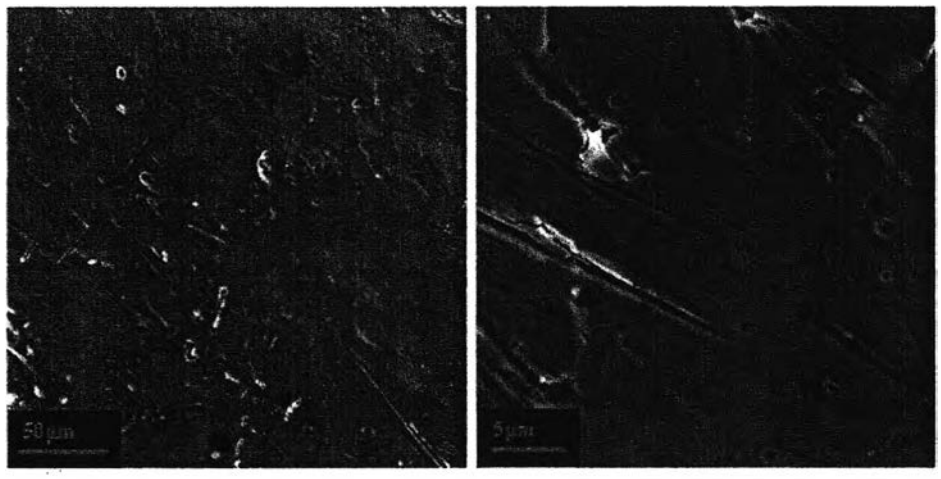

Figure 4.71 SEM images of Zirc-4 in Run 7.

Table 4.59 EDX result from the convex surface of Zirc-4 in Run 7

Position	Wt%						
	Ni	Fe	Cu	Zr	Ti	Zn	O
Amorphous oxide	0.62	1.15	0.72	72.6	0.52	0.68	23.71
Elongate oxide	0.35	1.14	0.26	70.41	0.5	0.44	26.9

From a comparison with Zirc-4 in Run 6, as shown in Figure 4.72, the oxide morphologies of Zirc-4 in Run 6 and Run 7 were similar. In addition, their corrosion rates were only very slightly different, as shown in Table 4.60. This may have been due to the fact that there was no effect of boron on oxide film formation of Zirc-4 between these two runs. As mentioned earlier, the lithium in the coolant can concentrate in the pores in ZrO_2 layers under conditions of surface boiling, resulting in accelerated corrosion of Zirconium alloy (Cox *et al.*, 1996) and the presence of boron can reduce the corrosion rate of zirconium alloys by inhibiting lithium incorporation into the oxide film (Pêcheur *et al.*, 1993). In this case, not only was the lithium concentration in Run 7 (without boron) quite low (0.28 ppm Li), but also there was no heat flux through the Zirc-4 surface to create subcooled boiling; the lithium in the coolant could not concentrate for accelerating the corrosion of Zirc-4 in this run. Moreover, the ZrO_2 oxide layer is protective. Thus, the corrosion of Zirc-

4 in Run 6 and Run 7 was not different. However, for the Zirc-4 samples in Run 1 and Run 2, which had the same heat flux through their surfaces, their corrosion rates were very different, as shown in Table 4.13, possibly due to the boron effect. It has been suggested that the beneficial of boron is to reduce the access of lithium in the oxide, which can cause an increase in the anion defect concentration or porosity in the oxide and, thus, in the oxygen diffusion rate through the oxide (Hillner and Chirigos, 1967).

A comparison of the corrosion rate of Zirc-4 in Run 7 with that in Run 2 shows that the corrosion rate of Zirc-4 in Run 2 was twice that in Run 7, even though the coolant temperature in Run 2 (295°C) was lower than that in Run 7 (300°C). This is no doubt due to the heat flux through the Zirc-4 surface in Run 2, possibly resulting in the concentrated lithium in the pores in ZrO_2 layer by creating subcooled boiling, which accelerated the corrosion of Zirc-4.

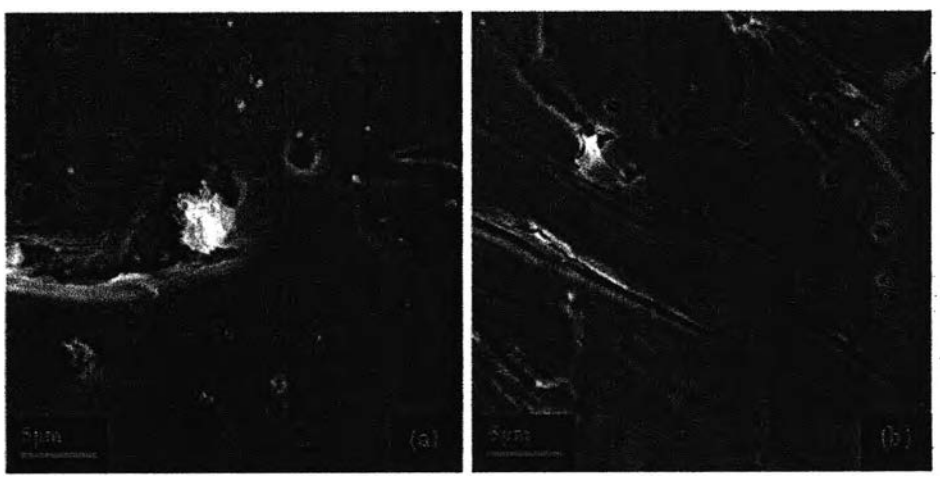

Figure 4.72 Comparison of the surface morphologies of Zirc-4 in Run 6 (a) with Zirc-4 in Run 7 (b).

Table 4.60 Corrosion rates of Zirc-4 in Run 2, Run 6 and Run 7

Zirc-4 sample	Surface Area (dm^2)	Weight Change (mg)	Exposure Time (days)	Corrosion rate (mdd)
Run 2	0.0417	+0.7	5	3.36
Run 6	0.8728	+0.73	5	1.66
Run 7	0.8728	+0.7	5	1.59

In summary, from the comparison of the results in Run 1 with those in Run 2 and the comparison of the results in Run 6 with those in Run 7, the oxides formed on Alloy 600 MA and SS304 in the coolant containing boron were more protective than those in the coolant without boron, possibly resulting from the incorporation of boron in the oxides. For Zirc-4, since ZrO_2 is more protective than the oxides formed on Alloy 600 MA and SS304, the effect of boron was observed only in the presence of subcooled boiling on the Zirc-4 surface (Run 1 and Run 2), which can concentrate the lithium to accelerate the corrosion. This means that in low lithium environments without boron, subcooled boiling on the Zirc-4 surface is necessary to increase the corrosion of Zirc-4, as indicated by Billot *et al.* (2002).

4.3 Corrosion Test in the Stainless Steel Autoclave without Heat Transfer

4.3.1 Run 8

In this run, samples were the same as those in Run 4, but they were exposed to the coolant for the 30 days in a stainless steel autoclave instead of a Ti-2 autoclave. During exposure, the samples were darkened as shown in Figure 4.73. The colors after exposure were different with different heat treatments and materials and corresponded with those in Run 4. Generally, the darkness and color are affected by the oxide coverage and the nature of the oxide.

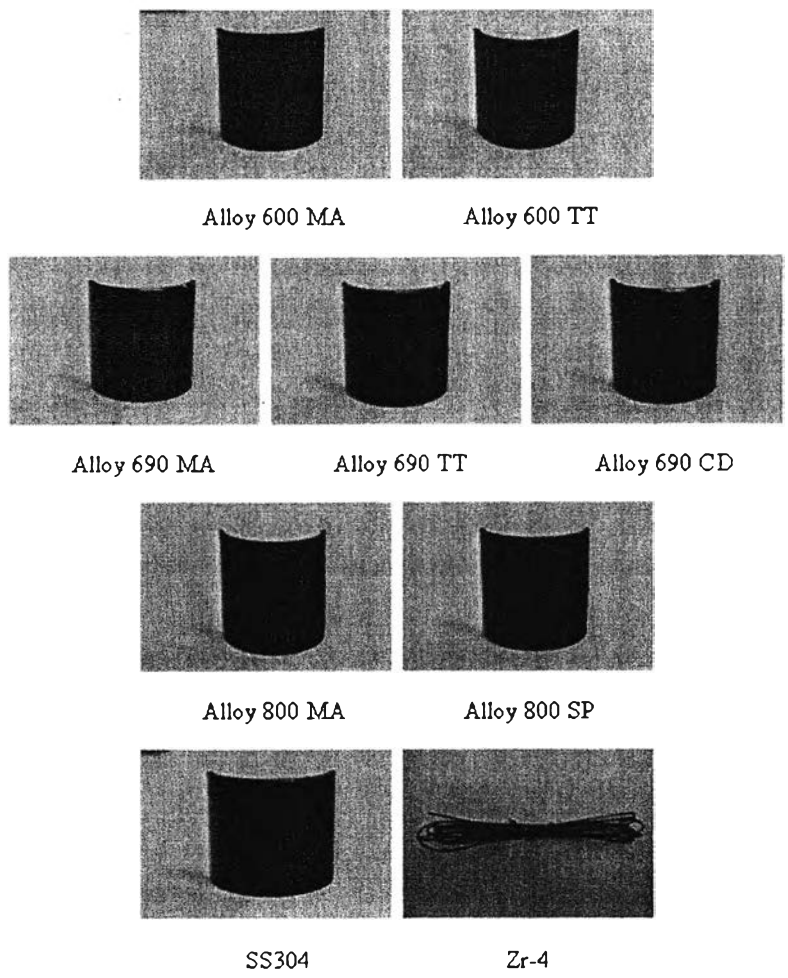

Figure 4.73 Samples after exposure in Run 8.

Table 4.61 shows the weight changes of samples after exposure. All SG samples and Zirc-4 gained weight, while most of SS304 samples, except SS304-4 (weight gain) and SS304-1 and SS304-5 (unchanged), lost weight. Removing the samples from the stainless steel wires on the sample tree was possibly one of the causes of weight loss.

Table 4.61 Weight of the samples before and after exposure in Run 8

Sample	Surface Area (cm^2)	Before (g)	After (g)	Weight Change (mg)	Weight Change per Unit Area (mg/dm^2)
Zircaloy-4	167.07	43.4049	43.4297	+24.8	+14.84
SS304-1	18.37	9.6002	9.6002	0.0	0.0
SS304-2	18.37	9.9187	9.9186	-0.1	-0.54
SS304-3	18.37	10.0189	10.0186	-0.3	-1.63
SS304-4	18.37	9.5668	9.5672	+0.4	+2.18
SS304-5	18.37	9.6380	9.6380	0.0	0.0
SS304-6	18.37	9.7185	9.7183	-0.2	-1.09
SS304-7	18.37	10.0182	10.0175	-0.7	-3.81
SS304-8	18.37	9.7001	9.6993	-0.8	-4.35
Alloy 600MA (Westinghouse)	12.37	4.7610	4.7620	+1.0	+8.08
Alloy 600 TT (Westinghouse)	12.35	4.7981	4.7988	+0.7	+5.67
Alloy 690 MA (Valinox)	12.36	4.4494	4.4496	+0.2	+1.62
Alloy 690 TT (Sandvik)	12.35	4.5668	4.5671	+0.3	+2.43
Alloy 690 TT (Valinox)	12.35	4.3635	4.3636	+0.1	+0.81
Alloy 690 CD (Valinox)	12.36	4.5078	4.5080	+0.2	+1.62

Alloy 800 MA (Unknown)	12.28	3.4904	3.4913	+0.9	+7.33
Alloy 800 SP (Sandvik)	12.34	4.1129	4.1142	+1.3	+10.53

Before and after exposure, the coolant pH, boron concentration and iron concentration were measured and the results are shown in Table 4.62. Boron concentrations and pH values before and after exposure were slightly different, however, these differences were within the measurement error. The Ni, Fe and Mn concentration after exposure were much higher than those before exposure and than those in the titanium autoclave. This is because these metal ions were not only released from the corrosion products and the base materials, but also from the stainless steel autoclave, which had a large surface area contacting with the coolant. The Zn concentration after exposure was also higher than that before exposure, possibly due to the residual Zn contamination from the lubricant used in this work and/or from the previous work.

Table 4.62 Coolant chemistry before and after exposure in Run 8

Conditions	Before	After
Boron concentration (ppm)	1996	2077
pH @ room temperature	6.84	6.81
$pH_{300°C}$	7.4	7.38
Fe concentration (ppb)	-	very low**
Ni concentration (ppb)	-	25.7±0.93
Mn concentration (ppb)	-	183.9±3.1
Zn concentration (ppb)	0.4*	9.2±1.1

*from the de-ionized water

**below the detection limit

In this run, oxides on all SG samples, SS304-4, SS304-8 and a small part of the Zirc-4 were analysed with EDX and SEM for studying the effect of SG alloy heat treatment and composition on oxide formation. In addition, the results in this run will be compared with those in Run 4 for studying the effect of dissolved ions in the coolant on the oxide formation. The results are presented and discussed as follows:

4.3.1.1 EDX and SEM Analyses

EDX and SEM were performed on the convex surfaces of samples. Figure 4.74 shows oxide morphologies of Alloy 600 MA and TT. They were both covered with polyhedral crystals on an amorphous layer. However, the crystals on Alloy 600 MA were bigger, but their coverage was lower and less uniform than those on Alloy 600 TT, corresponding with the results observed on Alloy 600 in Run 4. This difference is due to the heat treatment effect, as mentioned previously. Thus, the oxide formed on Alloy 600 TT is possibly more protective than that on Alloy 600 MA.

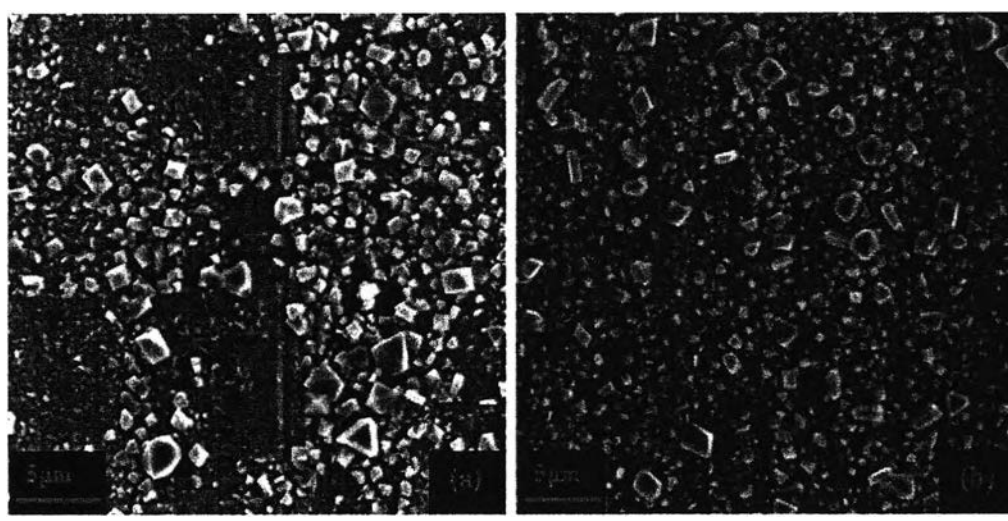

Figure 4.74 SEM images of Alloy 600 MA (a) and Alloy 600 TT (b) in Run 8.

The EDX results on Alloy 600 MA and TT are shown in Table 4.63 and Table 4.64. The tendencies of elemental compositions on Alloy 600 MA and TT were similar; the weight percentage of Fe was the highest in the

crystallites, while the weight percentage of Cr was the highest in the underlying layer, indicating that the crystallite was Fe-rich (possibly a nickel ferrite) and the underlying layer was Cr-rich (possibly a Ni-Fe chromite). Small amounts of Ti, Cu and Zr were observed in the oxides on both materials. Ti and Zr come from the base material and from the Zirc-4 sample. Copper possibly comes from the SG alloys and/or the lubricant.

Table 4.63 EDX result from the convex surface of Alloy 600 MA in Run 8

Position	Wt%						
	Ni	Fe	Cr	Ti	Cu	Zr	O
Crystallite	24.55	42.21	1.73	0.36	0.72	0.22	30.21
Underlying layer	63.16	8.88	15.94	0.56	1.79	0	9.67
Before exposure	70.83	9.63	15.40	0.39	*	-	2

*was not presented

Table 4.64 EDX result from the convex surface of Alloy 600 TT in Run 8

Position	Wt%						
	Ni	Fe	Cr	Ti	Cu	Zr	O
Crystallite	19.56	39.97	1.56	0.22	0.39	0.06	38.24
Underlying layer	58.91	11.15	18	0.65	1.08	0.14	10.07
Before exposure	71.56	9.41	15.09	0.29	*	-	2.54

*was not presented

Figure 4.75 shows oxide morphologies on Alloy 690 MA, TT and CD. All materials were covered with compact crystallite layer, so the underlying layer cannot be seen. However, their crystallite sizes and coverages were different according to the different heat treatments. Figure 4.75 (c) and (d) show that the oxide morphologies on Alloy 690 TT from Sandvik and Valinox were slightly different

possibly because they were processed with slightly different temperatures and times, as mentioned in Run 4. From a comparison of SEM images of Alloy 690 MA, TT and CD from Valinox as shown in Figure 4.76, the average crystallite size of CD was slightly bigger than that of TT, which was slightly bigger than that of MA, while TT had the highest crystallite coverage followed by MA and then CD. It is most likely that Alloy 690 TT had more compact oxide than Alloy 690 MA and Alloy 690 CD, corresponding with the results in Run 4.

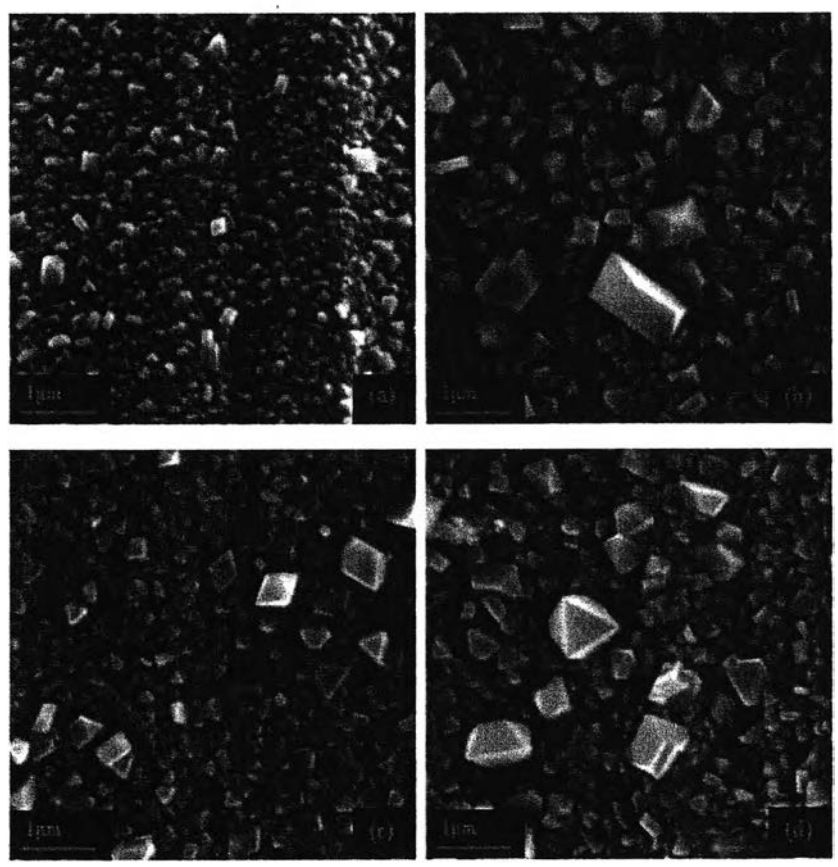

Figure 4.75 SEM images of Alloy 690 MA from Valinox (a), Alloy 690 CD from Valinox (b), Alloy 690 TT from Sandvik (c) and Alloy 690 TT from Valinox (d) in Run 8.

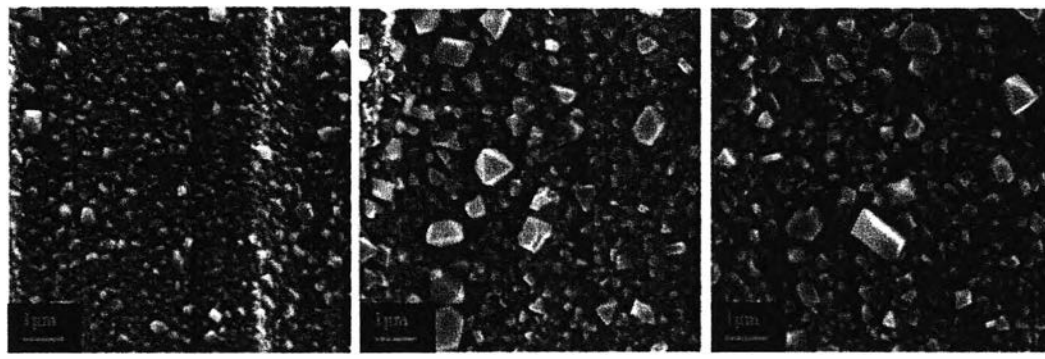

Alloy 690 MA Alloy 690 TT Alloy 690 CD

Figure 4.76 Comparison of SEM images of Alloy 690 MA, TT and CD from Valinox in Run 8.

The EDX results on Alloy 690 MA, TT and CD are shown in Table 4.65-4.67. The weight percentage of Ni decreased, while the weight percentage of Fe increased, toward the crystallite layer. Moreover, the weight percentage of Cr in the underlying layer was higher than that in the crystallite. These indicate that the crystallite was Fe-rich and the underlying layer was Cr-rich. Also, small amounts of Ti, Cu and Zr were observed in the oxides on these materials.

Table 4.65 EDX result from the convex surface of Alloy 690 MA in Run 8

Position	Wt%						
	Ni	Fe	Cr	Ti	Cu	Zr	O
Crystallite layer	29.79	28.95	15.73	0.35	1.18	0.06	23.94
Underlying layer	49.17	11.65	26.18	0.36	1.08	0	11.56
Before exposure	56.37	9.47	27.41	0.33	*	-	6.42

*was not recorded

Table 4.66 EDX result from the convex surface of Alloy 690 TT in Run 8

Position	Wt%						
	Ni	Fe	Cr	Ti	Cu	Zr	O
Crystallite layer	23.43	36.16	5.35	0.34	0.61	0.23	33.88
Underlying layer	38.31	12.34	30.15	0.43	1.32	0.1	17.35
Before exposure	57.55	9.80	27.37	0.30	*	-	4.98

*was not recorded

Table 4.67 EDX result from the convex surface of Alloy 690 CD in Run 8

Position	Wt%						
	Ni	Fe	Cr	Ti	Cu	Zr	O
Crystallite layer	20.52	34.78	3.29	0.12	0.46	0.31	40.52
Underlying layer	45.87	13.14	24.48	0.29	1.08	0.25	14.89
Before exposure	57.37	10.03	27.23	0.44	*	-	4.93

*was not recorded

SEM images of Alloy 800 MA and SP in Figure 4.77 show that crystallites over Alloy 800 MA surface were bigger, but their coverage was lower, than those over Alloy 800 SP surface because the surface of Alloy 800 SP had more defects created by shot peening, resulting in a higher oxide nucleation rate.

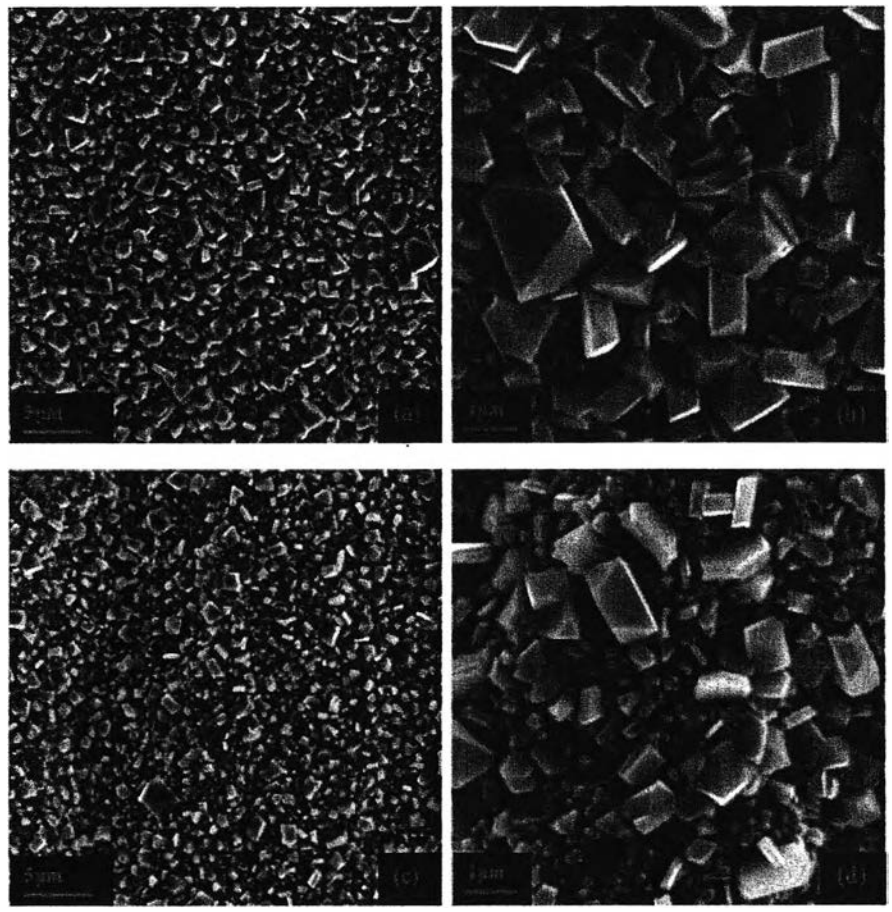

Figure 4.77 SEM images of Alloy 800 MA (a and b) and Alloy 800 SP (c and d) in Run 8.

From the EDX results on Alloy 800 MA and SP as tabulated in Table 4.68 and Table 4.69, the crystallites had the highest Fe content compared with the underlying layer and the base metal, while the Cr content was the highest in the underlying layer, indicating that the crystallite was possibly enriched in Fe and the underlying layer was enriched in Cr.

Table 4.68 EDX result from the convex surface of Alloy 800 MA in Run 8

Position	Wt%						
	Ni	Fe	Cr	Ti	Cu	Zr	O
Crystallite layer	18.05	45.06	2.17	0.3	0.47	0.08	33.87
Underlying layer	22.7	29.55	23.49	0.26	0.76	0.18	23.06
Before exposure	31.94	43.04	19.29	0.35	*	-	5.38

*was not recorded

Table 4.69 EDX result from the convex surface of Alloy 800 SP in Run 8

Position	Wt%						
	Ni	Fe	Cr	Ti	Cu	Zr	O
Crystallite layer	15.51	49.85	3.08	0.29	0.58	0.07	30.62
Underlying layer	25.49	32.92	21.98	0.52	0.67	0.13	18.29
Before exposure	31.59	41.96	20.96	0.54	*	-	4.95

*was not recorded

From a comparison of SEM images of Alloy 600 MA with those of Alloy 690 MA and Alloy 800 MA, as shown in Figure 4.78, it appears that in this run Alloy 800 MA had the biggest crystallites followed by Alloy 600 MA and then Alloy 690 MA, but the crystallite coverage of Alloy 690 MA was higher than those of Alloy 800 MA and Alloy 600 MA. However, the oxide formed on Alloy 690 MA was apparently more compact than that of Alloy 800 MA, which was more compact than that of Alloy 600 MA, no doubt due to the effect of Cr content of the alloys. This observation is consistent with the results observed in Run 4 and Run 5. Moreover, Figure 4.79 shows that the oxide formed on Alloy 690 TT was more compact than that on Alloy 600 TT. Thus, it might be summarized that Alloy 690 has the most protective oxide compared with Alloy 600 and Alloy 800, which were

processed with the same heat treatment and exposed to the same conditions and time, because it has the highest Cr content.

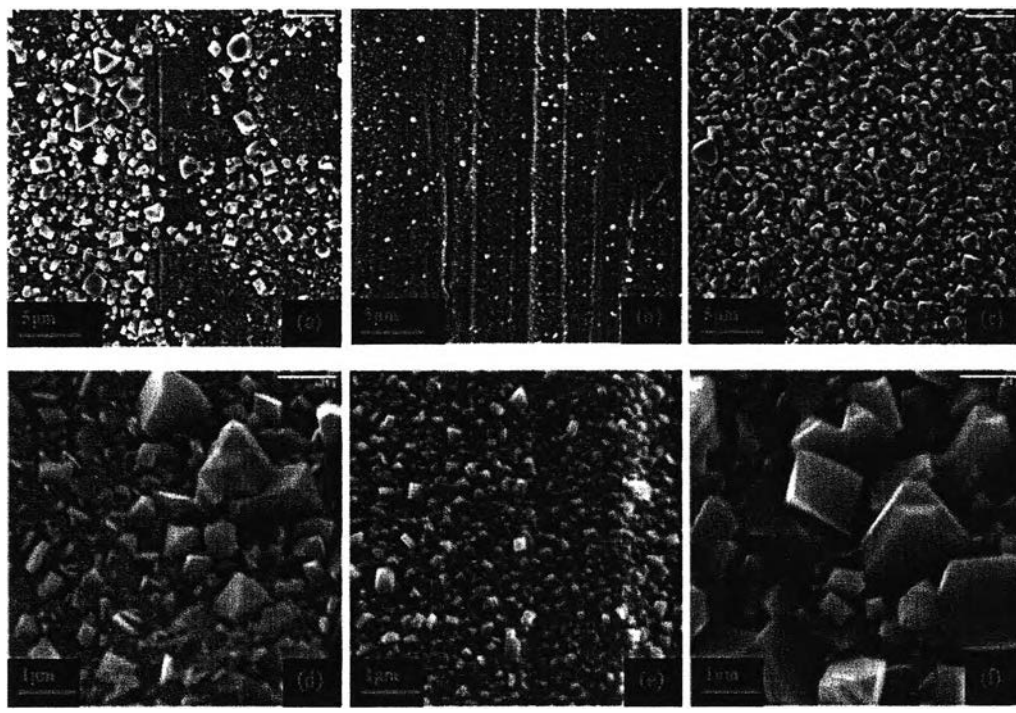

Figure 4.78 Comparison of SEM images of Alloy 600 MA (a and d), Alloy 690 MA (b and e) and Alloy 800 MA (c and f) in Run 8.

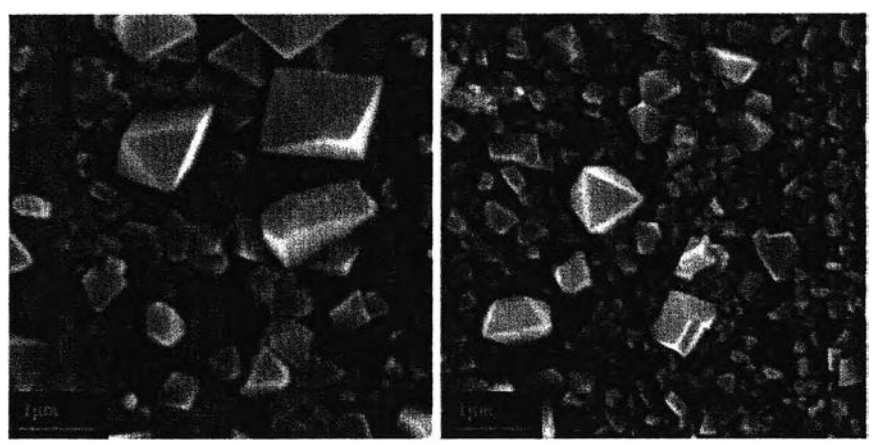

Alloy 600 TT **Alloy 690 TT**

Figure 4.79 Comparison of SEM images of Alloy 600 TT and Alloy 690 TT in Run 8.

In this run, the representative SS304 samples were SS304-4 (weight gain) and SS304-8 (weight loss). Their oxide morphologies, as shown in Figure 4.80, were similar, even though their weight changes were different. All the SS304-4 and SS304-8 surfaces were covered with mostly octahedral crystallites; a layer of large crystallites mixed with much smaller crystallites, overlaying an amorphous layer. EDX was performed on the crystallites and on the amorphous layers between the crystallites and the results are shown in Table 4.70 and Table 4.71. The weight percentages of Fe and Cr in the underlying layer were higher, but its Fe/Cr ratio was lower than those in the crystallite. Therefore, the crystallite was possibly richer in Fe than the underlying layer, which was rich in Cr.

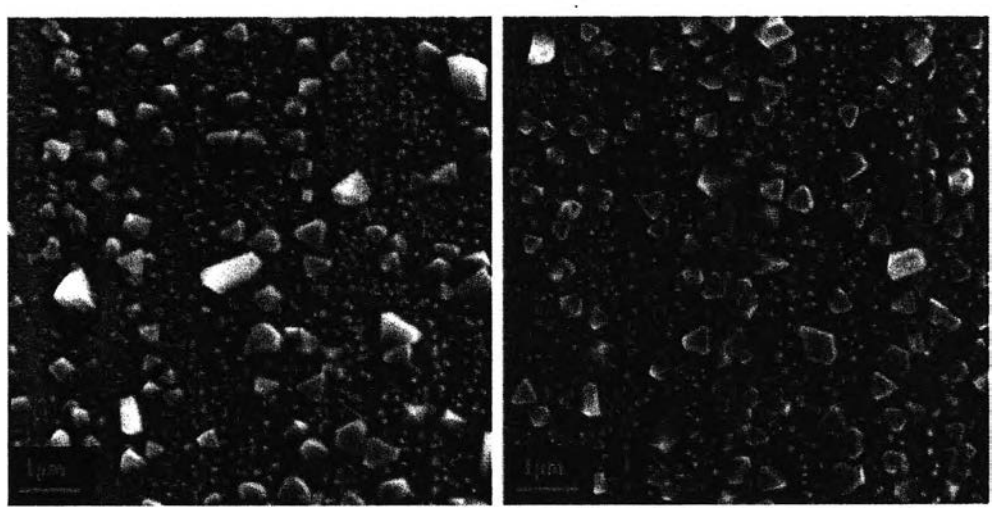

SS304-4 SS304-8

Figure 4.80 SEM images of SS304-4 and SS304-8 in Run 8.

Table 4.70 EDX result from the convex surface of SS304-4 in Run 8

Position	Wt%					
	Ni	Fe	Cr	Ti	O	Fe/Cr
Crystallite layer	8.1	51.52	7.85	0.22	28.67	6.56
Underlying layer	10.6	57.22	19.13	0.16	9.45	2.99

Table 4.71 EDX result from the convex surface of SS304-8 in Run 8

Position	Wt%					
	Ni	Fe	Cr	Ti	O	Fe/Cr
Crystallite layer	7.93	47.57	9.11	0.12	31.47	5.22
Underlying layer	10.57	57.81	19.51	0.17	9.1	2.96

The oxide formed on the Zirc-4 sample in this run was similar to that in Run 4. Amorphous oxide was observed on all the surface and platelets and elongated oxides were observed in cavities and/or at scratches, as shown in Figure 4.81. Also, there were oxide crystals sparsely scattered on over the surface. The EDX result in Table 4.72 indicates that the amorphous, platelet and elongated oxides were probably ZrO_2 and the oxide crystals were mostly Cu, according to the major constituents. Copper possibly comes from the SG alloys.

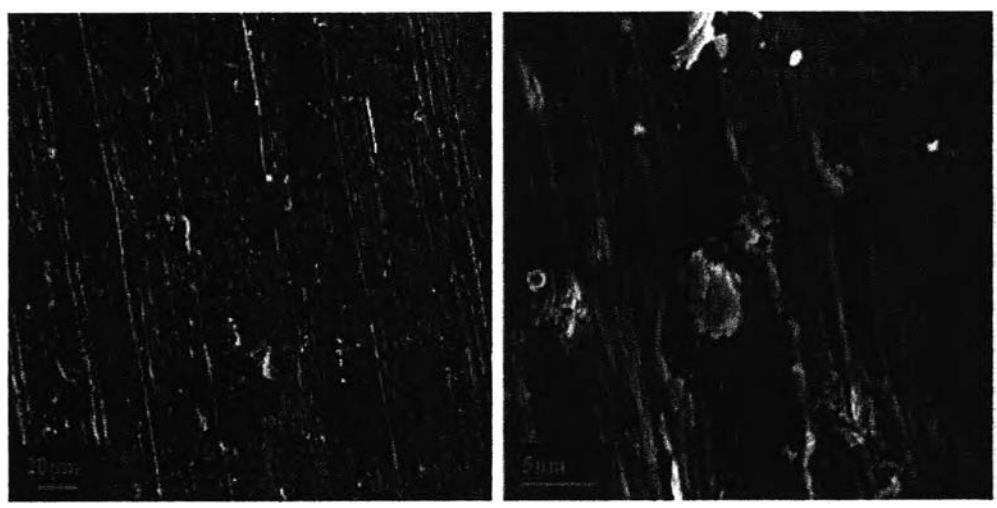

Figure 4.81 SEM images of Zirc-4 in Run 8.

Table 4.72 EDX result from the surface of Zirc-4 in Run 8

Position	Wt%					
	Ni	Fe	Cu	Zr	Ti	O
Amorphous oxide	0.64	1.19	0.75	67.26	0.44	29.72
Platelet/Elongate oxide	0.24	0.86	0.26	57.57	0.37	40.7
Crystal oxide	0.76	0	90.03	4.07	0	5.14

A comparison of oxides formed on samples exposed to the coolant in the stainless steel autoclave (Run 8) with those in the Ti-2 autoclave (Run 4) shows that the crystallites on the SG samples and on SS304 samples in Run 8 were bigger than those in Run 4; an example is shown in Figure 4.82. This is probably due to more concentrated solution species, which were released from the stainless steel autoclave, resulting in high oxide growth rate. In addition, the crystallite structures on Alloy 600 were different (platelet crystals in Run 4 and octahedral crystals in Run 8), possibly affected by the solution species.

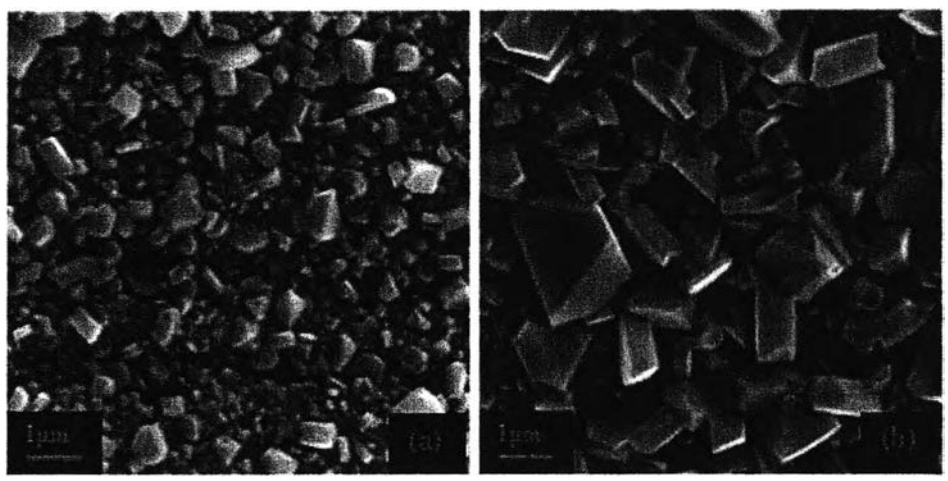

Figure 4.82 Comparison of surface morphologies of Alloy 800 MA in Run 4 (a) with Alloy 800 MA in Run 8 (b).

The oxide on the Zirc-4 samples in Run 4 was apparently thicker than that in Run 8, as can be seen in Figure 4.83. This difference may be due to the position of Zirc-4 sample in the autoclave. The Zirc-4 in Run 4, which was in the form of a coil, was placed close to the inside surface of the autoclave, which was covered with a jacket heater on the outside surface for providing heat, while the Zirc-4 in Run 8 was placed in the middle of the autoclave. Thus, the Zirc-4 in Run 4 was affected by the heat from the jacket heater more than that in Run 8, resulting in higher corrosion rate, as shown in Table 4.73.

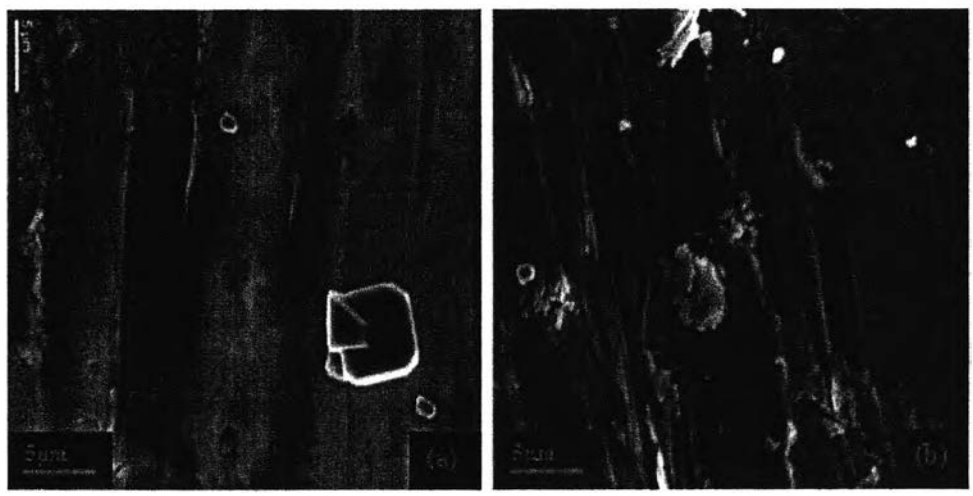

Figure 4.83 Comparison of the surface morphologies of Zirc-4 in Run 4 (a) with Zirc-4 in Run 8 (b).

Table 4.73 Comparison of Zirc-4 corrosion rate between Run 4 and Run 8

Zirc-4 sample	Surface Area (dm^2)	Weight Change (mg)	Exposure Time (days)	Corrosion rate (mdd)
Run 4	0.8778	+67	30	2.54
Run 8	1.6707	+24.8	30	0.49

4.3.2 Run 9

In this run, the samples were the same as those in Run 8, but they were exposed to the coolant containing 20 ppb Zn. All samples were darkened during exposure, as shown in Figure 4.84. However, the color of samples after this run was darker than that after Run 8, probably because of the zinc addition. This comparison is consistent with the comparison of color between the samples in Run 4 and those in Run 5 (exposed in titanium autoclave).

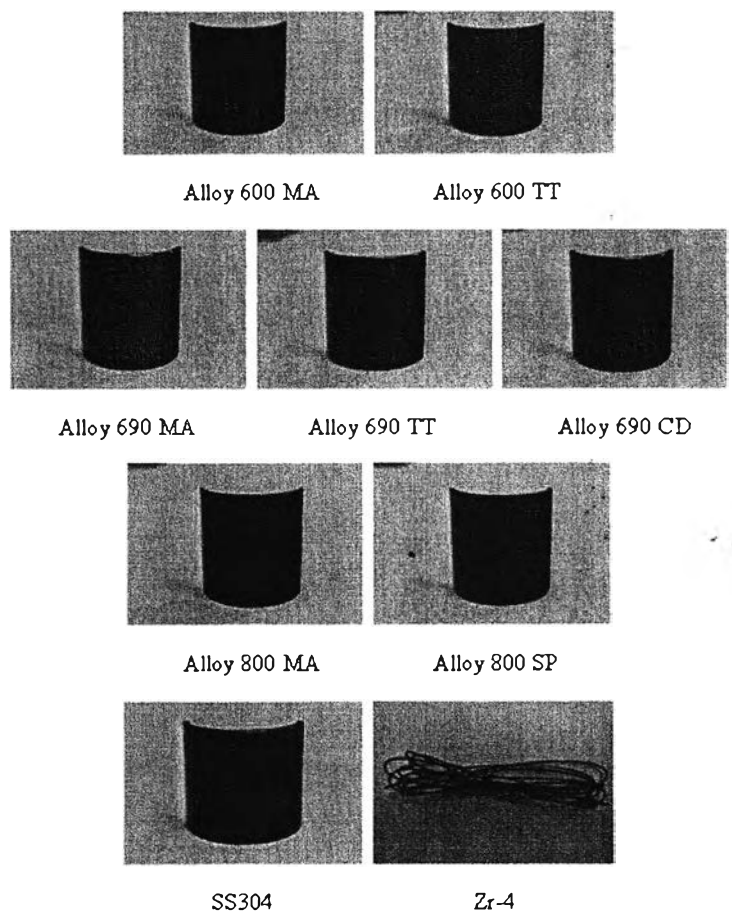

Figure 4.84 Samples after exposure in Run 9.

The weight changes of the samples are shown in Table 4.74. The Zircaloy-4 and SG alloy samples, except Alloy 690 TT from Valinox, gained weight, while most of the SS304 samples lost weight. Removing the samples from the stainless steel wires on the sample tree was one of the causes of weight loss.

Table 4.74 Weight of the samples before and after exposure in Run 9

Sample	Surface Area (cm^2)	Before (g)	After (g)	Weight Change (mg)	Weight Change per Unit Area (mg/dm^2)
Zircaloy-4	167.07	43.3834	43.4040	+20.6	+12.33
SS304-1	18.37	9.9475	9.9474	-0.1	-0.54
SS304-2	18.37	9.6719	9.6716	-0.3	-1.63
SS304-3	18.37	9.6380	9.6383	+0.3	+1.63
SS304-4	18.37	9.4568	9.4563	-0.5	-2.72
SS304-5	18.37	9.6575	9.6574	-0.1	-0.54
SS304-6	18.37	10.0318	10.0317	-0.1	-0.54
SS304-7	18.37	10.0367	10.0365	-0.2	-1.09
SS304-8	18.37	9.6180	9.6178	-0.2	-1.09
Alloy 600MA (Westinghouse)	12.37	4.7253	4.7256	+0.3	+2.42
Alloy 600 TT (Westinghouse)	12.35	4.6441	4.6446	+0.5	+4.05
Alloy 690 MA (Valinox)	12.36	4.4629	4.4633	+0.4	+3.24
Alloy 690 TT (Sandvik)	12.35	4.5167	4.5174	+0.7	+5.67
Alloy 690 TT (Valinox)	12.35	4.4123	4.4121	-0.2	-1.62
Alloy 690 CD (Valinox)	12.36	4.4652	4.4657	+0.5	+4.04
Alloy 800 MA (Unknown)	12.28	3.5260	3.5266	+0.6	+4.88
Alloy 800 SP (Sandvik)	12.34	4.0848	4.0855	+0.7	+5.67

Before and after exposure, boron concentration, coolant pH and iron concentration were measured and are shown in Table 4.75. The boron concentration and the coolant pH_T values before and after exposure were identical, while the coolant pH values at room temperature before and after exposure were very slightly different. However, the difference was within the measurement error. The Ni, Fe and Mn ions were released from the corrosion products and the base materials of SG and SS304 samples and stainless steel autoclave during exposure. However, the concentration of these metal ions in this run were lower than those in Run 8, possibly due to the Zn addition effect; the protective oxide was produced and acted as a barrier to reduce the corrosion product release. The Zn concentration after exposure was lower than that before exposure, probably due to the incorporation of Zn both in the oxides on the samples and the oxide on the stainless steel autoclave. However, the Zn concentration after exposure in this run was lower than that in Run 8, even though the Zn was added in the coolant in this run. This possibly resulted from the measurement error.

Table 4.75 Coolant chemistry before and after exposure in Run 9

Conditions	Before	After
Boron concentration (ppm)	2008	2008
pH @ room temperature	6.78	6.76
$pH_{300°C}$	7.39	7.39
Fe concentration (ppb)	-	very low**
Ni concentration (ppb)	-	8.8±0.93
Mn concentration (ppb)	-	150.2±3.1
Zn concentration (ppb)	20*	2.2±1.1

*from the Zn addition

**below the detection limit

Oxides on all SG samples, SS304-2, SS304-3 and a small part of the Zirc-4 were analysed with EDX and SEM to examine the effect of SG alloy

composition and heat treatment on oxide film formation. The results in this run were compared with the results in Run 8 in order to determine the effect of Zn addition on oxide film formation. The results are presented and discussed as follows:

4.3.2.1 EDX and SEM Analyses

Figure 4.85 shows oxide morphologies on Alloy 600 MA and TT. The samples were covered with a layer of small crystallites with large, sparse crystallites overlaying an amorphous layer. The oxide coverage of Alloy 600 MA was higher than that of Alloy 600 TT, but the crystallite coverage on Alloy 600 TT was more uniform than that on Alloy 600 MA. It may be hypothesized that the big crystallites on Alloy 600 MA occurred around the grain boundaries, probably due to the depletion of Cr around the grain boundaries, as explained in Run 4. However, the oxide formed on Alloy 600 MA was slightly more compact than that on Alloy 600 TT. It is interesting to note that the effects of heat treatment on the oxide formed on Alloy 600 in this run are not in agreement with those in Run 4, 5 and 8 (the oxide formed on Alloy 600 TT was more compact than that on Alloy 600 MA). This discrepancy might indicate that the effect of heat treatment was uncertain, depending on the exposure environment.

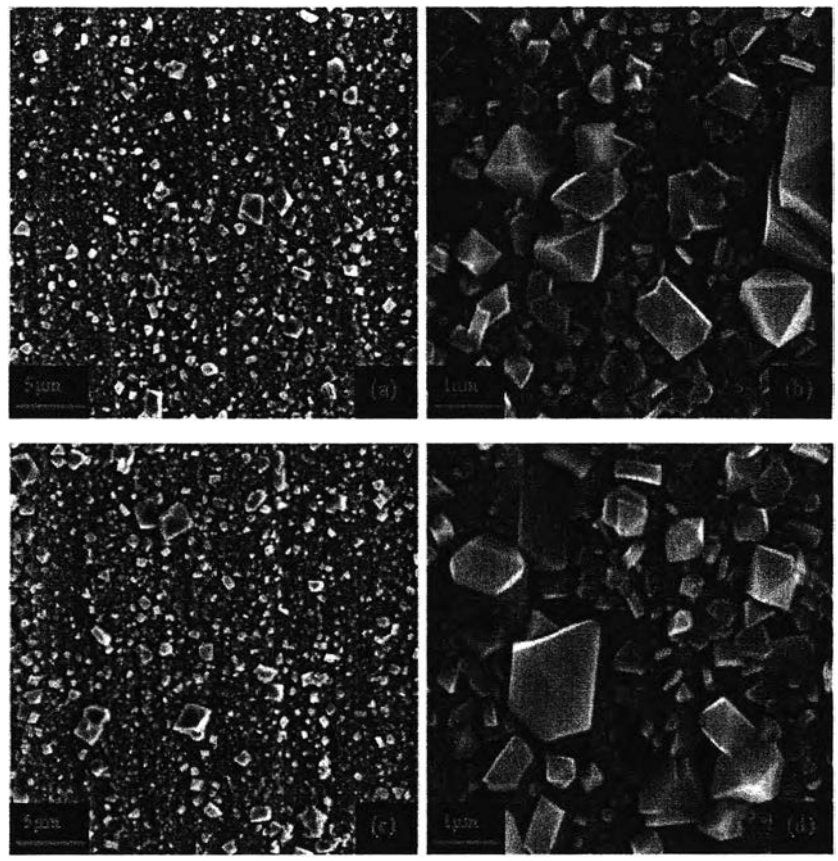

Figure 4.85 SEM images of Alloy 600 MA (a and b) and Alloy 600 TT (c and d) in Run 9.

The EDX results of oxides formed on Alloy 600 MA and TT are shown in Table 4.76 and Table 4.77. It should be noted that the elemental compositions of the underlying layer were determined by analysing the small crystallites. From the results on Alloy 600 MA, the weight percentage of Fe was the highest in the crystallites, while the weight percentage of Cr was the highest in the base metal. However, the weight percentage of Cr in the underlying layer was higher than that in the crystallite, indicating that the crystallite was richer in Fe than the underlying layer, which was enriched in Cr. From the EDX results on Alloy 600 TT, the weight percentage of Fe was the highest in the crystallite, while the weight percentage of Cr was the highest in the underlying layer. Also, it indicates that the crystallite was Fe-rich and the underlying layer was Cr-rich. The small amounts of Ti, Cu possibly come from the SG alloy samples, while Zr comes from the Zirc-4

sample. In addition, Zn was observed both in the crystallites and in the underlying layer, indicating the incorporation of zinc in the oxide. As mentioned previously in Run 5, Zn should prefer to incorporate in the inner oxide (underlying layer) than in the outer oxide (crystallites), but the weight percentage of Zn in the underlying layer was lower than that in the crystallite, presumably due to the interference of the EDX signal from the base metal.

Table 4.76 EDX result from the convex surface of Alloy 600 MA in Run 9

Position	Wt%							
	Ni	Fe	Cr	Ti	Cu	Zr	Zn	O
Crystallite	28.55	31.49	4.61	0.2	0.93	0.31	0.43	33.48
Underlying layer	59.69	12.4	14.62	0.5	1.47	0.08	0.35	10.89
Before exposure	70.83	9.63	15.40	0.39	*	-	-	2

*was not recorded

Table 4.77 EDX result from the convex surface of Alloy 600 TT in Run 9

Position	Wt%							
	Ni	Fe	Cr	Ti	Cu	Zr	Zn	O
Crystallite	25.5	46.37	2.83	0.33	0.59	0.24	0.33	23.81
Underlying layer	64.7	11.2	16.77	0.31	0.97	0.17	0.24	5.64
Before exposure	71.56	9.41	15.09	0.29	*	-	-	2.54

*was not recorded

Figure 4.86 shows oxide morphologies on Alloy 690 MA, TT and CD. The samples were covered with a compact layer of small crystallites with large sparse crystallites, with the result that the underlying layer cannot be seen. The oxides morphologies on Alloy 690 TT from Sandvik and from Valinox, as shown in Figure 4.86 (c) and (d), respectively, were slightly different possibly because they

were processed with the slightly different temperatures and times, as mentioned in Run 4. A comparison of the oxide morphologies on Alloy 690 MA, TT and CD from Valinox, as shown in Figure 4.87, shows that the crystallites on Alloy 690 TT were slightly smaller than those on Alloy 690 MA, which were smaller than those on Alloy 690 CD. However, the oxide coverage on Alloy 690 TT was higher than that on Alloy 690 MA, which was higher than that on Alloy 690 CD. Therefore, the oxide formed on Alloy 690 TT was slightly more compact than that on Alloy 690 MA, which was more compact than that on Alloy 690 CD. The effect of heat treatment on oxide film formed on Alloy 690 in this run is consistent with those observed in Run 4, 5 and 8.

Next, EDX was performed on the large crystallites and on the layer of small crystallites on Alloy 690 MA, TT and CD to determine the elemental compositions in the crystallite and in the underlying layer. The EDX results on Alloy 690 MA, TT and CD from Valinox, as shown in Table 4.78-4.80, show that the crystallites on Alloy 690 MA, TT and CD had the highest Fe content compared with the underlying layer and the base metal. The underlying layer of Alloy 690 TT had the highest Cr content compared with the crystallite and the base metal, while the weight percentages of Cr in the underlying layers on Alloy 690 MA and CD were slightly lower than that in the base metal, possibly due to the interference of the EDX signal from the small crystallites on top. However, the weight percentages of Cr in the underlying layers on Alloy 690 MA and CD were higher than those in the crystallites. Thus, the underlying layers on all Alloy 690 were richer in Cr than the crystallites, which were Fe-rich. Titanium, Cu and Zr were also observed in the oxides of these materials. Furthermore, for all Alloy 690 samples, the weight percentage of Zn in the underlying layers was higher than that in the large crystallites, probably due to the preferential Zn incorporation in the underlying layer (as inner oxide) and/or the interference of the EDX signal from the small crystallites on top, which were possibly as $ZnFe_2O_4$.

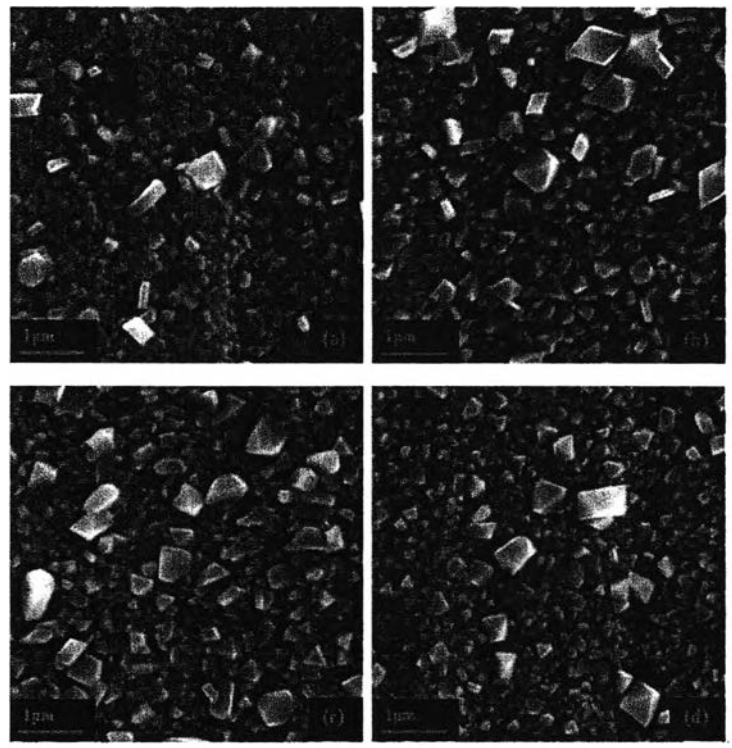

Figure 4.86 SEM images of Alloy 690 MA from Valinox (a), Alloy 690 CD from Valinox (b), Alloy 690 TT from Sandvik (c) and Alloy 690 TT from Valinox (d) in Run 9.

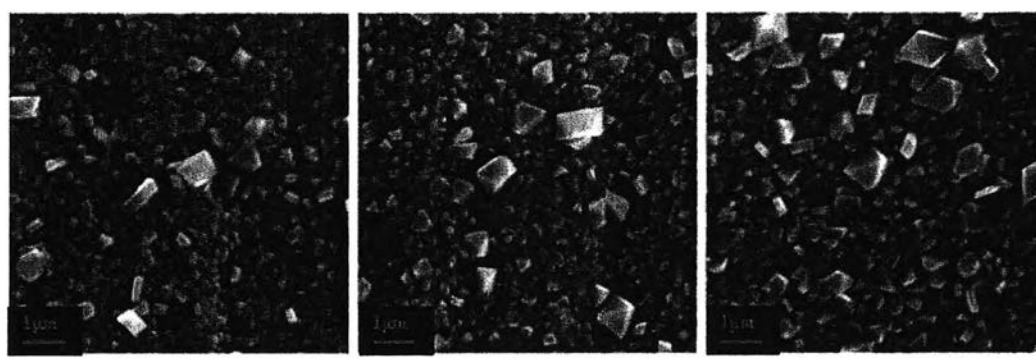

Figure 4.87 Comparison of SEM images of Alloy 690 MA, TT and CD from Valinox in Run 9.

Table 4.78 EDX result from the convex surface of Alloy 690 MA in Run 9

Position	Wt%							
	Ni	**Fe**	**Cr**	**Ti**	**Cu**	**Zr**	**Zn**	**O**
Crystallite	22.52	36.03	8.73	0.23	0.51	0.18	0.51	31.29
Underlying layer	43.36	14.19	24.78	0.69	1.04	0.05	0.91	14.98
Before exposure	56.37	9.47	27.41	0.33	*	-	-	6.42

*was not recorded

Table 4.79 EDX result from the convex surface of Alloy 690 TT in Run 9

Position	Wt%							
	Ni	**Fe**	**Cr**	**Ti**	**Cu**	**Zr**	**Zn**	**O**
Crystallite	24.5	31.99	8.61	0.3	0.39	0.2	0.26	33.75
Underlying layer	43.57	11.78	29.15	0.37	0.89	0.1	0.5	13.64
Before exposure	57.55	9.80	27.37	0.30	*	-	-	4.98

*was not recorded

Table 4.80 EDX result from the convex surface of Alloy 690 CD in Run 9

Position	Wt%							
	Ni	**Fe**	**Cr**	**Ti**	**Cu**	**Zr**	**Zn**	**O**
Crystallite	23.33	35.75	5.11	0.24	0.3	0.17	0.48	34.62
Underlying layer	44.8	14.01	24.92	0.54	0.93	-	0.67	14.13
Before exposure	57.37	10.03	27.23	0.44	*	-	-	4.93

*was not recorded

Surfaces of Alloy 800 MA and SP were covered with a layer of small crystallites mixed with larger crystallites overlaying an amorphous layer, but their crystallite sizes and coverages were different, as shown in Figure 4.88. Alloy 800 SP had smaller crystallites, while their coverage was higher, than Alloy 800 MA, possibly due to the higher defects on Alloy 800 SP by shot peening, which resulted in the higher oxide nucleation. Therefore, the oxide formed on Alloy 800 SP was more compact than that on Alloy 800 MA. This observation is consistent with the results observed on Alloy 800 in Runs 4, 5 and 8.

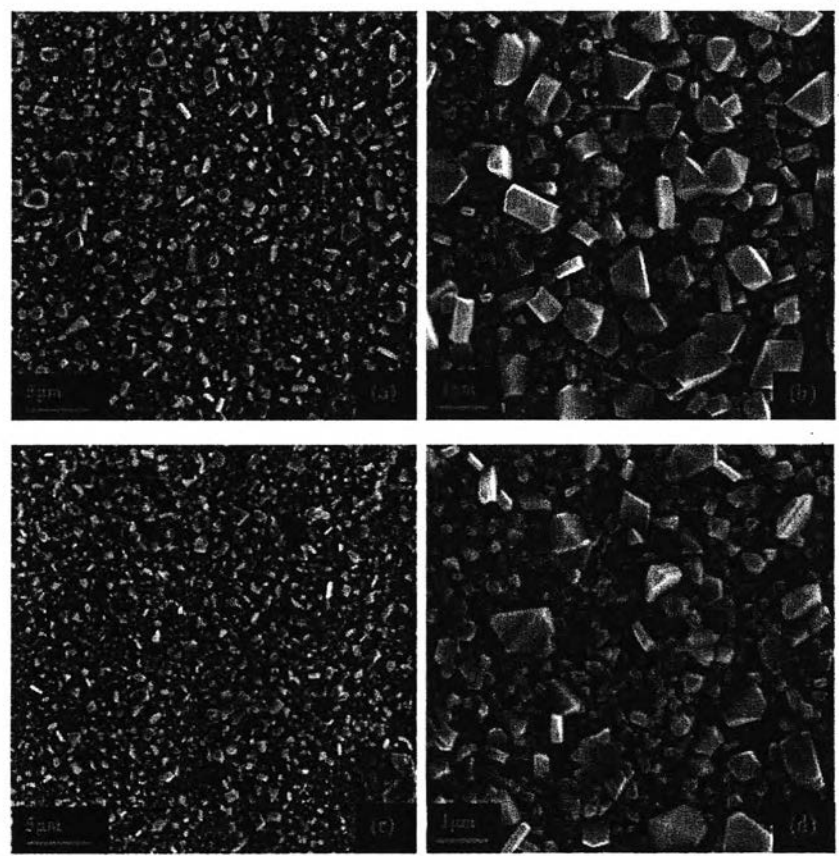

Figure 4.88 SEM images of Alloy 800 MA (a and b) and Alloy 800 SP (c and d) in Run 9.

The elemental compositions in the crystallite and in the underlying layer of Alloy 800 were determined using EDX performed on the large crystallite and on the layer of small crystallites and are shown in Table 4.81 and

Table 4.82. The weight percentage of Fe was the highest in the crystallite compared with the underlying layer and the base metal, while the weight percentage of Cr was the highest in the underlying layer. These indicate that the crystallite was Fe-rich and the underlying layer was Cr-rich. Small amounts of Ti, Zr and Cu were also observed in the oxides. Zn was observed in the crystallite and in the underlying layer, but the weight percentage of Zn in the underlying layer was higher than that in the crystallite. This is possibly due to the preferential Zn incorporation in the underlying layer and/or the interference of the EDX signal from the small crystallites on top, which was expected to be $ZnFe_2O_4$.

Table 4.81 EDX result from the convex surface of Alloy 800 MA in Run 9

Position	Wt%							
	Ni	Fe	Cr	Ti	Cu	Zr	Zn	O
Crystallite	18.17	43.3	4.22	0.57	0.31	0.14	0.17	33.12
Underlying layer	22.58	31.98	22.14	0.46	1.1	-	0.73	21.01
Before exposure	31.94	43.04	19.29	0.35	*	-	-	5.38

*was not recorded

Table 4.82 EDX result from the convex surface of Alloy 800 SP in Run 9

Position	Wt%							
	Ni	Fe	Cr	Ti	Cu	Zr	Zn	O
Crystallite	17.34	44.02	5.69	0.25	0.25	0.27	0.19	31.99
Underlying layer	24.17	36.38	22.04	0.6	0.81	0.18	0.7	15.12
Before exposure	31.59	41.96	20.96	0.54	*	-	-	4.95

*was not recorded

Figure 4.89 show a comparison of oxide morphologies on Alloy 600, Alloy 690 and Alloy 800, which were processed by mill annealing (MA).

The oxide formed on Alloy 690 MA was more compact than that on Alloy 800 MA, which was more compact than that on Alloy 600 MA. This observation confirms that oxide morphology depended strongly on the SG alloy composition, as observed previously in Run 4, 5 and 8. From Table 2.2, Alloy 690 has the highest Cr content followed by Alloy 800 and then Alloy 600. This indicates that the oxide formed on a higher-Cr alloy was more protective than that on a lower-Cr alloy because Cr is a significant component of protective oxides.

For the thermally treated (TT) alloys, again, the oxide formed on Alloy 690 TT was more compact than that on Alloy 600 TT, as shown in Figure 4.90, no doubt because it has a higher Cr content.

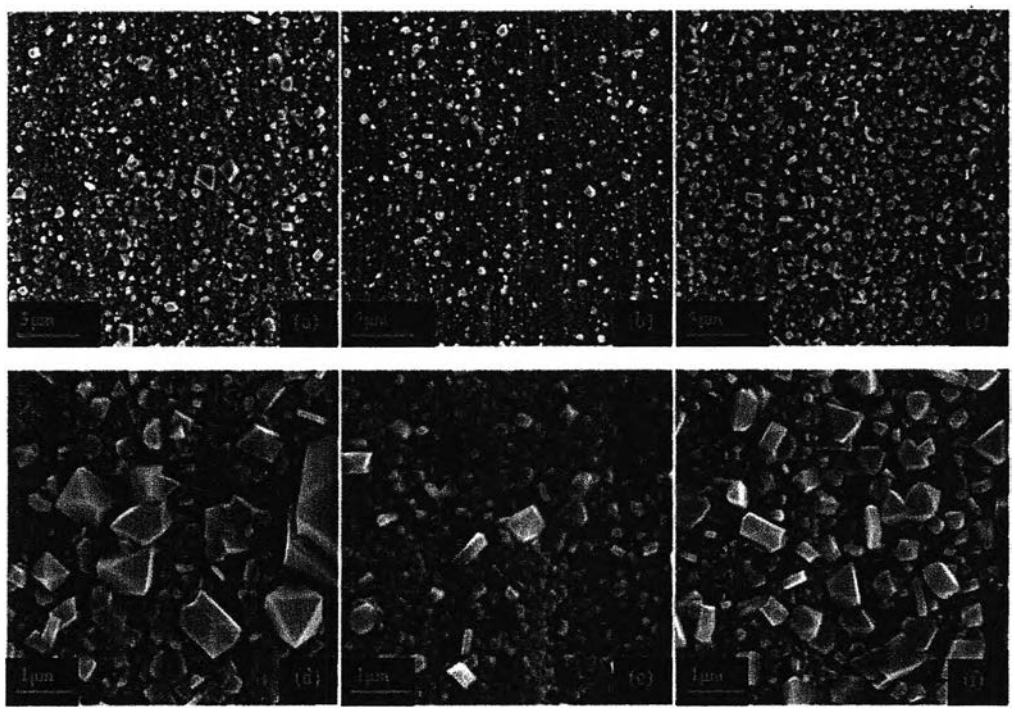

Alloy 600 MA **Alloy 690 MA** **Alloy 800 MA**

Figure 4.89 Comparison of SEM images of Alloy 600 MA, Alloy 690 MA and Alloy 800 MA in Run 9.

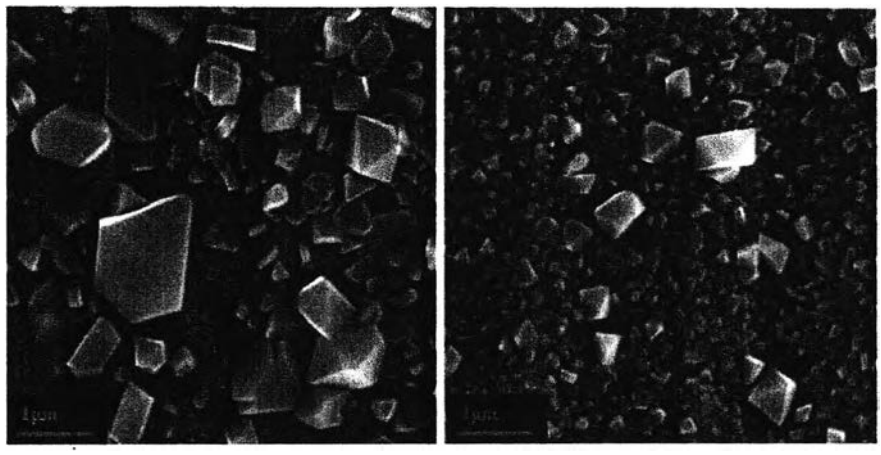

Alloy 600 TT Alloy 690 TT

Figure 4.90. Comparison of SEM images of Alloy 600 TT and Alloy 690 TT in Run 9.

In this run, SS304-2 (weight loss) and SS304-3 (weight gain) were selected as representative to be analysed with SEM and EDX. Oxide morphologies of SS304-2 and SS304-3 were very similar, as shown in Figure 4.91. The samples were covered with a layer of small and much larger crystallites overlaying an amorphous layer.

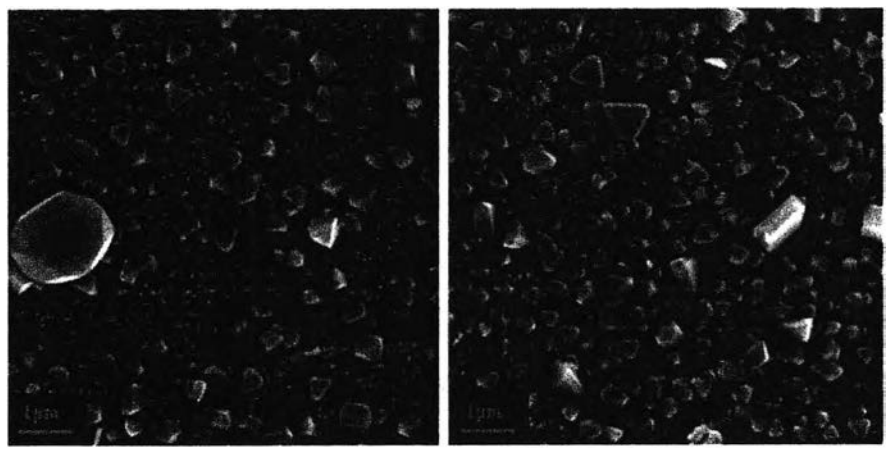

SS304-2 SS304-3

Figure 4.91 SEM images of SS304-2 and SS304-3 in Run 9.

The EDX results on SS304-2 and SS304-3 are shown in Table 4.83 and Table 4.84. The elemental compositions in the underlying layer were determined by analysing the layer of small crystallites. The results show that .the weight percentage of Fe in the crystallite was higher, but the weight percentage of Cr in the crystallite was lower, than in the underlying layer. Therefore, the crystallite was richer in Fe than the underlying layer, which was enriched in Cr. Again, Ti, Zr and Cu were observed in the oxides. Since SS304 samples were not covered with the compact layer of small crystallites, as observed on Alloy 690 (MA, TT and CD) and Alloy 800 (MA and SP), the interference of the Zn signal from the small crystallites was lessened. Therefore, the higher weight percentage of Zn in the underlying layer than that in the crystallite is possibly due to the preferential incorporation of Zn in the underlying layer.

Table 4.83 EDX result from the convex surface of SS304-2 in Run 9

Position	Wt%							
	Ni	Fe	Cr	Ti	Cu	Zr	Zn	O
Crystallite	5.91	57.66	3.51	0.42	0.28	0.21	0.2	31.53
Underlying layer	9.97	53.21	19.69	0.16	2.23	0.16	0.54	13.37

Table 4.84 EDX result from the convex surface of SS304-3 in Run 9

Position	Wt%							
	Ni	Fe	Cr	Ti	Cu	Zr	Zn	O
Large Crystallite	5.14	61.84	3.93	0.33	0.35	0.11	0.45	27.72
Underlying layer	10.46	61.15	19.03	0.22	0.98	-	0.61	6.84

The oxide morphology on Zirc-4 is shown in Figure 4.92. Zircaloy-4 was covered with an amorphous oxide over the entire surface. Elongated oxides were observed at scratches and there were small crystallites sparsely scattered on the surface. According to the major constituent in the amorphous, elongated and

crystallite oxides, as shown in Table 4.85, the amorphous and elongated oxides were possibly ZrO_2 and the small crystallite was probably CuO. Titanium and Cu found in the oxides could have come from SG alloys. Zinc was also observed in these oxides; however, Zn should not affect to the oxide formed on Zirc-4, as reported by Byers and Jacko (1993).

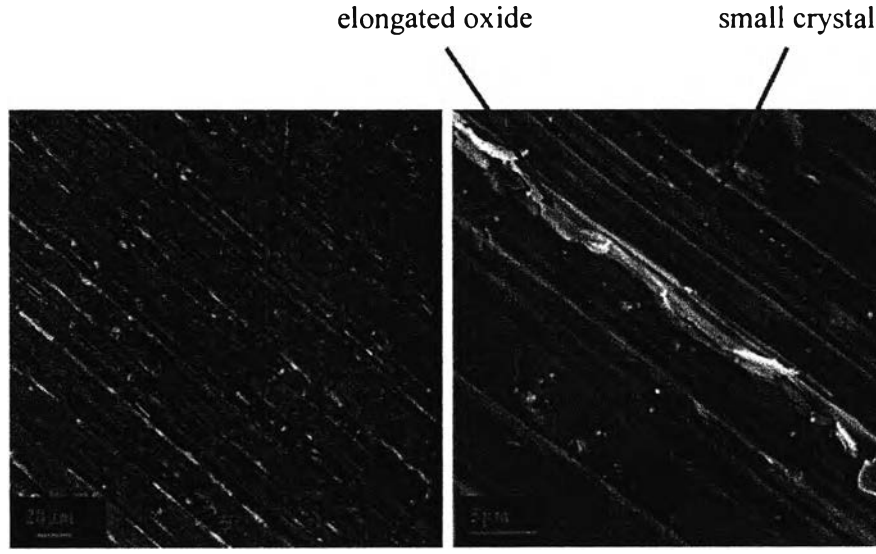

Figure 4.92 SEM images of Zirc-4 in Run 9.

Table 4.85 EDX result from the convex surface of Zirc-4 in Run 9

Position	Wt%						
	Ni	Fe	Cu	Zr	Ti	Zn	O
Amorphous oxide	0.72	1.18	0.87	72.45	0.49	0.72	23.57
Platelet/Elongated oxide	0.82	1.68	0.95	73.02	0.67	0.83	22.03
Crystal oxide	1.65	1.07	76.63	14.28	0.1	0.78	5.49

A comparison of the oxide morphologies on SG and SS304 samples in Run 8 (without Zn addition) with those in Run 9 (with 20 ppb Zn addition) is shown in Figure 4.93-4.96. The SG and SS304 samples in both two runs were covered with a layer of small crystallites with large, sparse crystallites

overlaying an amorphous layer. However, the small crystallites in the presence of 20 ppb Zn in the coolant (Run 9) were smaller, while their coverage was higher, than those in the coolant without Zn addition (Run 8), resulting in a more compact oxide. The reason for this is, Zn was incorporated in the inner oxide layer and in the outer oxide layer to form stable oxides, e.g. $ZnCr_2O_4$ and $ZnFe_2O_4$, resulting in the high oxide nucleation. This observation is consistent with the comparison of the results in Run 4 (without Zn) with those in Run 5 (with 20 ppb Zn). Therefore, it was quite reasonable to conclude that the Zn addition enhanced the formation of protective oxide on SG alloys and SS304.

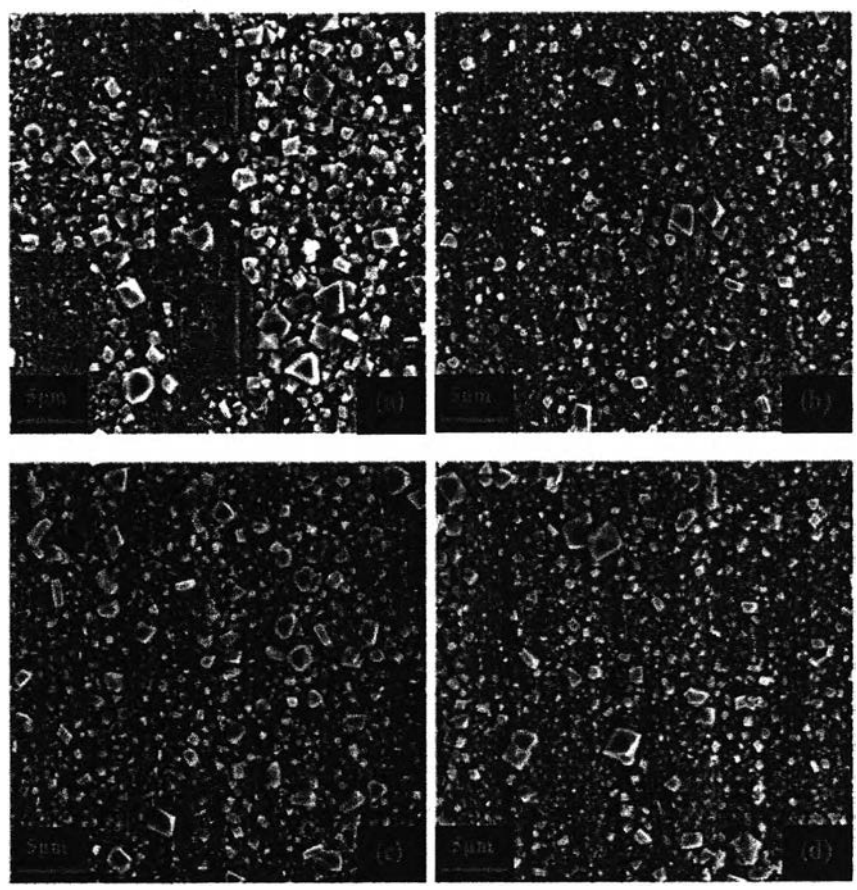

Figure 4.93 Comparison of the surface morphologies of Alloy 600 MA (a) and Alloy 600 TT (b) in Run 8 with Alloy 600 MA (c) and Alloy 600 TT (d) in Run 9.

The EDX results in both runs show that Zn was observed both in the crystallite and in the underlying layer, indicating the incorporation of Zn in the crystallite probably as zinc ferrite and in the underlying layer possibly as zinc chromite.

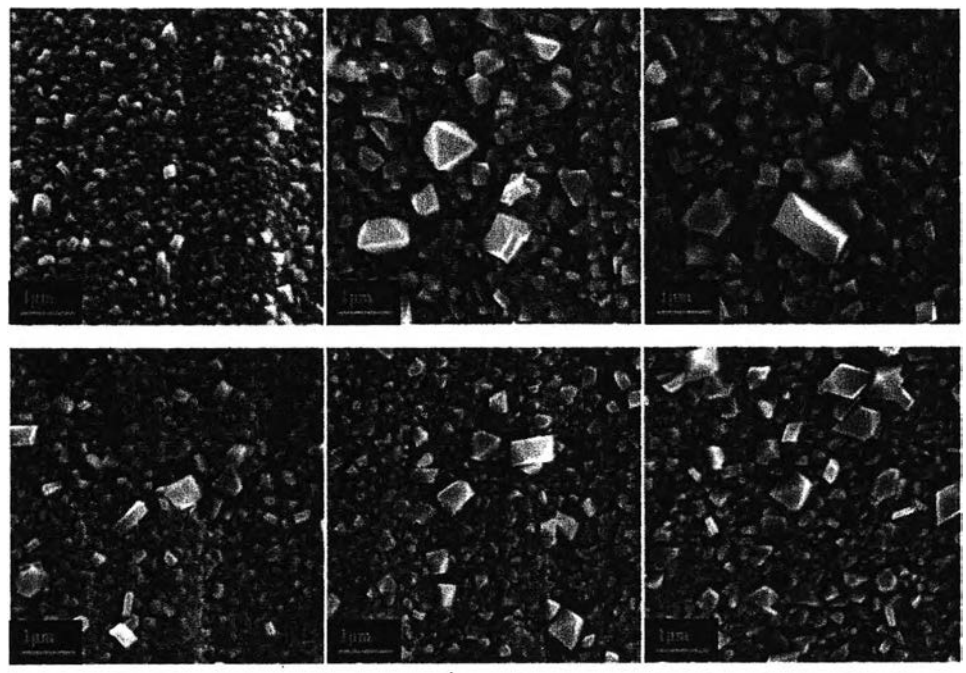

Figure 4.94 Comparison of the surface morphologies of Alloy 690 MA, TT and CD in Run 8 (top) with Alloy 690 MA, TT and CD in Run 9 (below).

From a comparison of oxide morphology on Zirc-4 in Run 8 with that in Run 9, as shown in Figure 4.97, the oxides formed on Zirc-4 in Run 8 and Run 9 were very similar. However, their corrosion rates were slightly different, as shown in Table 4.86. Therefore, it is possible that there was no effect of Zn addition on oxide formed on Zirc-4, corresponding to the result reported by Byers and Jacko (1993) and EPRI TR-105714 (1999). Moreover, this observation possibly confirmed that the lower corrosion rate of Zirc-4 in Run 5 (with Zn addition), than Zirc-4 in Run 4 (without Zn addition) did not result from the effect of Zn, but it probably resulted from the leak and the slightly different coolant pH, as mentioned in Run 5.

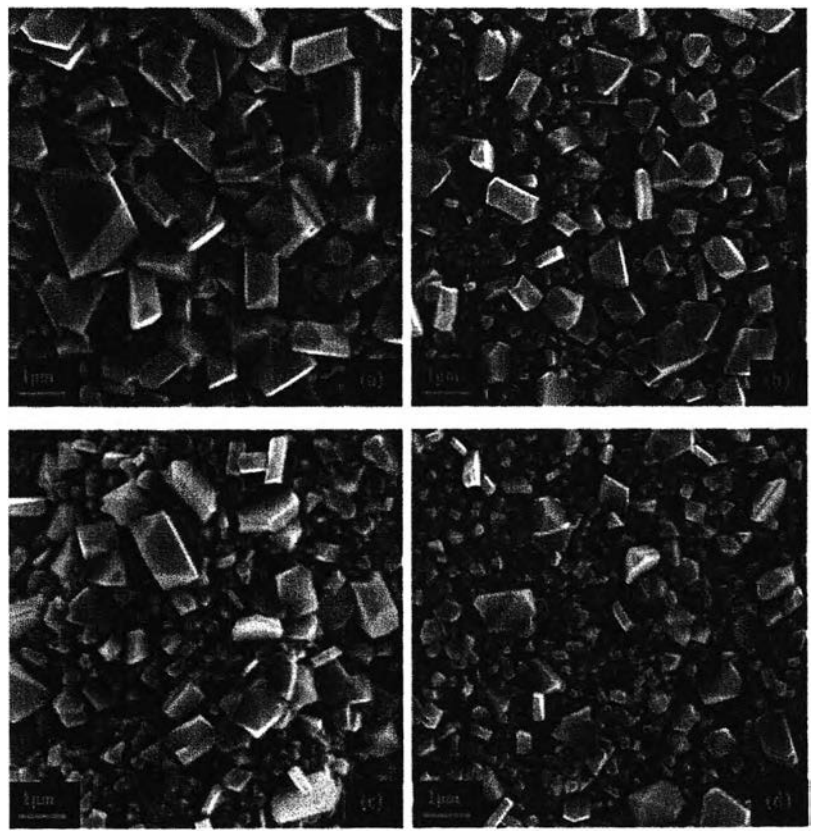

Figure 4.95 Comparison of the surface morphologies of Alloy 800 MA (a) and Alloy 800 SP (c) in Run 8 with Alloy 800 MA (b) and Alloy 800 SP (d) in Run 9.

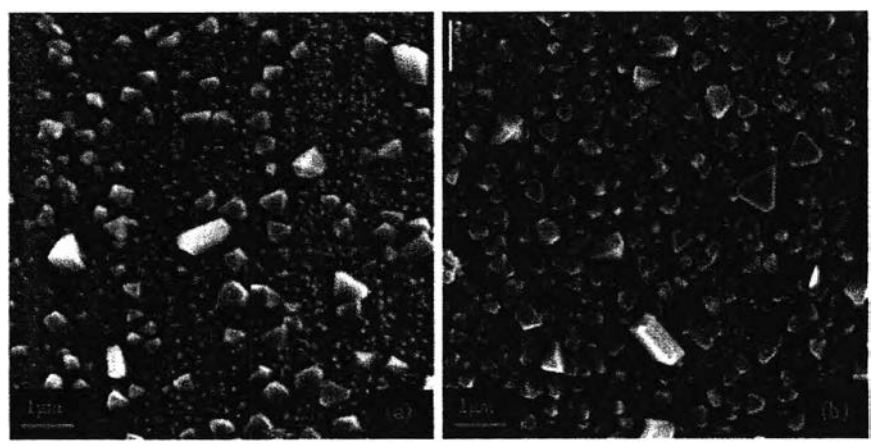

Figure 4.96 Comparison of the surface morphologies of SS304 in Run 8 (a) with SS304 in Run 9 (b).

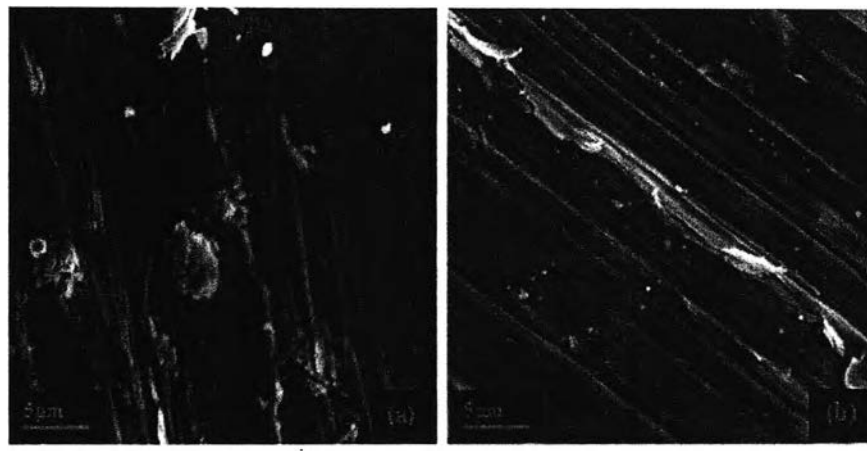

Figure 4.97 Comparison of the surface morphologies of Zirc-4 in Run 8 (a) with Zirc-4 in Run 9 (b).

Table 4.86 Comparison of Zirc-4 corrosion rate between Run 8 and Run 9

Zirc-4 sample	Surface Area (dm^2)	Weight Change (mg)	Exposure Time (days)	Corrosion rate (mdd)
Run 8	1.6707	+24.8	30	0.49
Run 9	1.6707	+20.6	30	0.41

4.4 Discussions

From all results described previously, the discussions are obtained as follows:

4.4.1 Oxide Morphology

From the present results, the surfaces of the corroded samples after exposure had different characteristic morphologies, depending on SG alloy composition, SG alloy heat treatment, boron concentration, Zn addition, dissolved ions in the coolant, exposure time and coolant temperature. Nevertheless, the oxides formed on SG alloys and 304 stainless steel (SS304) presented a duplex oxide

consisting of an Fe-rich crystallite layer and a Cr-rich underlying layer. The crystallite layer presented a bimodal size distribution of large, sparse crystallites and a more uniform distribution of small crystallites. Moreover, the crystallite shape depended on the nature of the base metal and the saturation of the coolant in Ni and Fe ions. Zircaloy-4 was covered with a single oxide layer of ZrO_2.

4.4.2 The Effect of SG Alloy Composition on Oxide Film Formation

From the comparison of the oxide morphologies of Alloy 600, Alloy 690 and Alloy 800, which were processed by the same heat treatment and exposed to the same coolant for the same time, their oxide morphologies were different. It is clear that the SG alloy composition had a large effect on the oxide morphology. The compactness of the oxide formed on Alloy 690 MA suggests that it may have been more protective than that on Alloy 800 MA and on Alloy 600 MA. It is most likely effected by the Cr content in the alloys; the weight percentage of Cr in Alloy 690 is higher than that in Alloy 800 and then Alloy 600 and because chromium is a significant component of protective oxides ($FeCr_2O_4$ and $NiCr_2O_4$).

4.4.3 The Effect of SG Alloy Heat Treatment on Oxide Film Formation

From the results, the oxide morphologies on the same SG alloys were different with different heat treatments, indicating that heat treatments affected the oxide formation. However, heat treatment effects were overshadowed by effects of alloy composition. On Alloy 600, which was processed by mill annealing (MA) and thermal treatment (TT), the oxide coverage on Alloy 600 TT was higher and more uniform than that on Alloy 600 MA. This is possibly because MA processed at ~1000°C for few minutes results in carbide precipitation within the grain boundaries and hence, the depletion of Cr around the grain boundaries. Thermal treatment (TT) processed after mill annealing at 700-720°C for 10-15 hours dissolves carbides into solid solution and then precipitates some within the grains, resulting in the less Cr depletion at the grain boundaries and the uniform carbide-precipitate distribution throughout the grain. Moreover, it is well known that a Cr-depleted area is a preferential site for corrosion. Therefore, it is hypothesized that Alloy 600 TT could be corroded uniformly across the grains, while Alloy 600 MA may have been more

corroded at the grain boundaries. On Alloy 690, which was processed by mill annealing (MA), thermal treatment (TT) and cold drawing (CD), the oxide formed on Alloy 690 TT was more compact than that on Alloy 690 MA and Alloy 690 CD. Alloy 690 CD had the least compact oxide possibly because it had the biggest grain size compared with Alloy 690 MA and TT (Lister *et al.*, 2009), resulting in the lowest oxide nucleation. On Alloy 800, which was processed by mill annealing (MA) and shot peening (SP), the oxide formed on Alloy 800 SP was more compact than that on Alloy 800 MA, possibly because of the numerous defects by shot peening, resulting in the higher oxide nucleation.

4.4.4 Effect of Boron Concentration on Oxide Film Formation

In an attempt to examine the effect of boron on oxide film formation, the results in Run1 and Run6, in which the coolant contained both boron and lithium, were compared with those in Run2 and Run7, in which the coolant contained only lithium. The major difference between the comparison of the results in Run1 with those in Run2 and the comparison of the results in Run6 with those in Run7 was the heat flux through the SG alloy samples and Zirc-4 samples; Run1 and Run2 had heat flux, but Run6 and Run7 did not.

From the comparisons, it is quite clear that the oxides formed on Alloy 600 MA and SS304 in the coolant containing both boron and lithium were more protective (small crystallites with high coverage) than those in the coolant without boron. The reason for this is possibly because boron was incorporated to form a protective oxide. Kawamura *et al.* (2002) suggested that boron in the form of H_3BO_3 can produce the protective oxide by reactions with magnetite (Fe_3O_4) in high-temperature water, as shown by the following equations (Eq. 1 is a correction to the equation in the ref.):

$$4Fe_3O_4 + 2H_3BO_3 + 6H_2O \longrightarrow 2Fe_3BO_5 + 3Fe_2O_3.3H_2O \quad (1)$$

$$6Fe_3BO_5 + 22H_3BO_3 \longrightarrow 4Fe_3B_7O_{13}.OH + 3Fe_2O_3.3H_2O + 22H_2O \quad (2)$$

From the equations, hulsite (Fe_3BO_5) and boracites ($Fe_3B_7O_{13}.OH$) were expected to be the protective oxides.

For Zirc-4 samples, since ZrO_2 is more protective than the oxides formed on Alloy 600 MA and SS304, the effect of boron was observed only in the presence of heat flux through the Zirc-4 surface (Run1 and Run2), as shown by the corrosion rate of Zirc-4 in Table 4.87. This may be explained by the fact that, in the presence of heat flux, there was sub-cooled boiling occurring on the Zirc-4 surface, resulting in the concentration of lithium in the pores in the oxide. This could accelerate the corrosion of zirconium alloy in the coolant without boron. There are three hypotheses to explain the accelerated corrosion of zirconium alloy due to lithium. First hypothesis: the incorporation of lithium in ZrO_2 increases the anion defects in the oxide, resulting in the increasing oxygen diffusion rate through the oxide film (Hillner *et al.*, 1967). Second hypothesis: LiOH affects the recrystallization processes in the ZrO_2 by rapid transition from a tetragonal to a monoclinic phase, resulting in the generation of pores and cracks in the oxide (Bramwell *et al.*, 1991). Third hypothesis: in concentrated LiOH solutions, the undissociated LiOH can react with the ZrO_2 oxide to produce soluble oxide (Li_2ZrO_3), resulting in the dissolution of ZrO_2 and, hence, the generation of pores for oxygen diffusion through the oxide-metal interface (Billot *et al.*, 2002).

Table 4.87 Corrosion rate of Zirc-4 in Run1, 2, 6 and 7

Zirc-4 sample	Heat Flux through Surface	Boron	Lithium	Corrosion rate (mdd)
Run1	Yes	Yes	Yes	1.92
Run2	Yes	No	Yes	3.36
Run6	No	Yes	Yes	1.66
Run7	No	No	Yes	1.59

4.4.5 Effect of Zn Addition on Oxide Film Formation

From a comparison of oxides formed on samples exposed to Zn-free coolant with those exposed to coolant containing 20 ppb Zn, in both cases the SG and SS304 samples were covered with crystallites consisting of large crystallites (non-uniformly distributed) and small crystallites (uniformly distributed), but their crystallite sizes, shapes and coverages were different, possibly due to a zinc effect. Since the small crystallites in the coolant containing 20 ppb Zn were smaller and had higher coverage than those in the Zn-free coolant, it is likely that the oxides formed on SG and SS304 samples in the coolant containing Zn were more protective than those in the Zn-free coolant. This is possibly caused by the incorporation of Zn in the oxide, resulting in the formation of stable oxides, e.g., $ZnCr_2O_4$ in the inner oxide and $ZnFe_2O_4$ in the outer oxide. Ziemniak and Hanson (2006) mentioned that the replacement of Fe(II) by Zn(II) in the ferrite (outer oxide) changes the structure of the oxide from inverse spinel (magnetite) to normal spinel ($ZnFe_2O_4$), which is more stable, resulting in the high oxide nucleation rate and, hence, the formation of a large number of small crystallites at the base of the outer layer close to the inner layer, consistent with the results from the coolant containing Zn. From the EDX results from these oxides, Zn was observed in the crystallites and in the underlying layer in the presence of 20 ppb zinc, confirming that Zn was incorporated in the crystallites possibly as zinc ferrite, and in the underlying layer possibly as zinc chromite. However, there was no effect of zinc on the oxide formed on Zirc-4.

Besides the SG alloy composition, SG alloy heat treatment, boron concentration and Zn addition effects, the effects of dissolved ions in the coolant, exposure time and coolant temperature on oxide film formation were also observed in this work.

4.4.6 The Effect of Dissolved Ions in the Coolant on Oxide Film Formation

The oxides formed on samples exposed to the coolant in the stainless steel autoclave may be compared with those in the Ti-2 autoclave. The crystallites on the SG samples and on the SS304 samples in the stainless steel autoclave were bigger than those in the titanium autoclave, probably due to more concentrated solution species, which were released from the stainless steel autoclave, resulting in

high oxide growth rate. However, there was no effect of dissolved ions in the coolant on oxide formed on Zirc-4, probably due to no precipitation of metal ions from the coolant on the Zirc-4 surface.

4.4.7 The Effect of Exposure Time on Oxide Film Formation

From the comparison of the oxide morphologies on Alloy 600 TT and SS304 in Run3 (10 days) with those in Run4 (30 days), Alloy 600 TT in Run3 formed a single-layered oxide, while Alloy 600 TT in Run4 formed a double-layered oxide. The SS304 samples in Run3 and Run4 formed a double-layered oxide, but the crystallites on SS304 in Run4 were bigger and had higher coverage than those in Run3. Moreover, the comparison of the oxide morphology on SS304 in Run3 (10days) with that in Run6 (5 days) shows a similar observation, but the difference cannot be seen clearly, probably due to a smaller difference in the exposure time. These observations suggest that the crystallite layer (as the outer oxide layer) was formed in the saturated coolant by precipitation of ions, and the time period used to form this layer was different with different materials in the same coolant, depending on their corrosion resistances. In addition, the crystallite size and coverage increase with increasing time. This can be explained by the theory of Ostwald ripening; the smallest particles (with the highest surface energy) tend to dissolve to benefit the largest particles with increasing time.

4.4.8 The Effect of Coolant Temperature on Oxide Film Formation

The comparison of the oxide morphologies on SS304 in Run1 (295°C) with that in Run3 (300°C) shows that the crystallites on SS304 in Run3 was smaller and had higher coverage than those in Run1. Moreover, this was also observed in the comparison of the oxide morphologies on SS304 in Run2 (295°C) with that in Run7 (300°C). Therefore, it is clear that the crystallite size decreases, while the crystallite coverage increases, with increasing temperature, possibly because a higher temperature results in a higher corrosion rate.